ALBERT-LUDWIGS-UNIVERSITÄT
FREIBURG
INSTITUT FÜR INFORMATIK

Lehrstuhl für Mustererkennung und Bildverarbeitung
Prof. Dr. Hans Burkhardt

Detection and Classification of 3D Tissue Samples of Colorectal Carcinomas

Detektion und Klassifikation von Mitosen in 3D Gewebeproben

von kolorektalen Karzinomen

Diplomarbeit

Matthias Schlachter

September 08 ~ März 09, 6 Monate

Erklärung

Hiermit erkläre ich, daß die vorliegende Arbeit von mir selbständig und nur unter Verwendung der aufgeführten Hilfsmittel erstellt wurde.

Freiburg, den

Zusammenfassung

In dieser Diplomarbeit werden neue Verfahren zur Detektion und Klassifikation von Objekten in Mehrkanal 3D Aufnahmen vorgestellt. Für die Detektion von Objekten wurden neue Bildfilterungsverfahren entwickelt, die es ermöglichen an Hand von Trainingsdaten eine an das zu detektierende Objekt angepasste Bildfilterung durzuführen. Die entwickelten Bildfilterungsverfahren können auf beliebig vielen Kanälen eingesetzt werden. Um in einem zweiten Schritt die detektierten Objekte zu verifizieren wurden bereits bewährte Merkmale zur 3D Objectkerkennung auf 3D Mehrkanal Aufnahmen erweitert.

Die entwickelten Verfahren wurden erfolgreich auf Zellkulturen von kolorektalen Karzinomen zur Detektion von aberranten Mitosen eingesetzt.

Abstract

The present diploma thesis introduces new approaches for the detection and classification of objects in multi-channel 3D data sets. For the detection of objects new image filtering techniques were developed. Based on given training data they allow for an image filtering which is adapted to a specific object. The image filtering algorithms can be deployed on an abitrary number of channels. To verify detected objects, established features for the recognition of 3D objects were extended to multichannel 3D data sets.

The present methods were successfully used for the detection of aberrant mitoses in cell cultures of colorectal carcinomas.

Danksagungen

Ich möchte mich zuallererst bei Herrn Prof. Dr.-Ing. Hans Burkhardt bedanken, mir es ermöglicht zu haben diese Abschlussarbeit an seinem Lehrstuhl zu erstellen.

Herrn Prof. Dr. Matthias Teschner möchte ich meinen Dank aussprechen, sich die Zeit dafür zu nehmen, meine Diplomarbeit als Zweitgutachter entgegenzunehmen.

Dr. Olaf Ronneberger möchte ich für die ausgezeichnete Betreuung und für das Formulieren der Fragestellung meinen Dank aussprechen.

Des weiteren möchte ich mich bei Dr. Silke Lassmann und Ihrer Arbeitsgruppe bedanken, ohne deren Vorarbeit und Mitwirkung eine Arbeit mit vorliegender Fragestellung nicht zustande gekommen wäre.

Besonderer Dank gebührt auch Dr. Marco Reisert, der mir immer mit Rat bei Seite stand.

Und nicht zu vergessen meine Kollegen Henrik und Sebastian, die mir immer eine große Hilfe waren.

Und zu guter Letzt meiner Familie die mich die letzten Jahre über immer unterstützt hat.

Contents

1 Introduction **1**
- 1.1 Outline . . . 2

2 Biological Background **3**
- 2.1 Cell Division and the Cell Cycle . . . 4
- 2.2 Cancer Cells and Aberrant Mitosis . . . 5
- 2.3 Cell Lines . . . 6

3 Preliminaries **9**
- 3.1 Irreducible Representations of Elements of SO(3) . . . 10
- 3.2 Spherical Tensor Analysis . . . 10
- 3.3 Spherical and Solid Harmonics . . . 13
- 3.4 Spherical Derivatives . . . 14
- 3.5 Spherical Gaussian Derivatives . . . 16

4 Tensor Voting and Harmonic Filters **17**
- 4.1 Harmonic Filters . . . 17
- 4.2 Differential Formulation of the Voting Function . . . 19
- 4.3 Training: Finding Optimal Filter Parameters . . . 22
- 4.4 Higher Order Tensor Fields . . . 24
- 4.5 Tensor Fields of Multi-Channel Data . . . 25
- 4.6 Antisymmetric Products and Local Non-linearities . . . 27

5 Steerable Filter **29**
- 5.1 M-th Order Basis Filter Bank . . . 29
- 5.2 Design of the Template . . . 31
- 5.3 Steering and Implementation . . . 31

6 Feature Computation **33**
- 6.1 Spherical Harmonic Descriptor . . . 33
- 6.2 Extending the Descriptor to Multi-Channel Data . . . 35
- 6.3 Simplified MiSP Invariants for Multi-Channel Data . . . 37

7 Experiments **41**
- 7.1 Description of Data . . . 41
- 7.2 Segmentation . . . 42
- 7.3 Detection of Mitosis Cells . . . 43

7.4 Cross Validation Results 50
7.5 Validation with Support Vector Machines 51

8 Conclusion and Outlook **53**
8.1 Outlook 53

A Appendix **57**
A.1 Spherical Harmonics 57
A.2 Clebsch Gordan Coefficients 57
A.3 Wigner D-Matrix 58

B Details of all Filter Algorithms **59**
B.1 Steerable Filter 59
B.2 Harmonic Filter (Single Channel) 63
B.3 Harmonic Filter Multi-Channel 65
B.4 Harmonic Filter Multi Channel (GVF) 67
B.5 Harmonic Filter Multi Channel (Antisymmetric Products) 69

C Cross Validation Results **71**
C.1 SVM Histogram Intersection Kernel 71
C.2 SVM Histogram Intersection Kernel (scaled) 73
C.3 NN Cross Validation Results 75

D Overview of the Data **82**
D.1 Treated Group (Nocodacole) 82
D.2 Control Group (DMSO) 84
D.3 Data sets 85

1 Introduction

In our society cancer diagnosis are constantly increasing. Improved methods for detection and quantification of individual cellular and genetic aberrations need to be fully established as supplementary tool to classical histomorphological analysis. Automated three dimensional imaging methods are expected significantly to improve today's standards of histopathology and molecular pathology. In particular, quantitative multi-parametric three dimensional assessment of candidate molecular markers in the context of tumour cells within routinely processed tissue specimens will be a crucial task to significantly improve prognostic and predictive pathology.

For example the development and progression of colorectal cancer is determined by several pathways of genetic instability, such as chromosomal instability, microsatellite instability and a methylation-related instability. Alterations in these genetic pathways and mutations of specific genes within the evolving tumour cell population contribute to tumour cell invasion and metastasis, and the aggressiveness of the disease. The molecular aspects of tumour cell biology are of primary importance for individual patient prognosis and the therapeutic response to current therapeutic strategies.

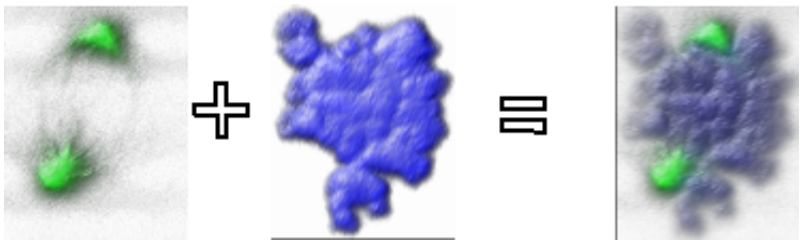

Figure 1.1: Overlay of FITC and DAPI channels of a colorectal cancer cell.

The main goal of the current work was to detect and classify mitotic cells in tissue samples of colorectal cancer. Therefore we will introduce new techniques in the area of multi-channel image (see figure 1.1) filtering and feature extraction methods.

Detection of objects in images is one of the fundamental tasks of image processing. However, the variety of objects and image acquisition parameters makes this process not trivial. There are many types of filter based feature detectors for lines and corners [FY91] [AJU05] [YLZW06] but only very few have the ability to learn the objects of interest in a generic way [SMH98] [Rei09]. Many approaches are model based such as the Hough transform and involve a previous segmentation of objects [RWB08][SSR+06]. For multi-channel images most algorithms are only addressed to 2d problems [Cyg05].

1.1 Outline

This work is organised as the following.

Chapter 2 will give brief introduction on the biological and medical background.

In chapter 3 we will give the theoretical background needed to understand most concepts of the following chapters.

Chapter 4 introduces the concept of harmonic filters. We will extend the concept to multi-channel data.

Chapter 5 gives a brief introduction on the theory of steerable filters in 3D. Since steerable filter are a state of the art concept in image filtering in many object and feature detection tasks, this was the main reference for our techniques developed in chapter 4.

In chapter 6 we will discuss various feature extraction methods with regard to multi-channel data.

In chapter 7 we will present the results of our experiments.

And finally chapter 8 will complete the current work by summarising and discussing the introduced concepts and giving an outlook on how to solve outstanding problems.

2 Biological Background

In this chapter we want to present a brief overview of the biological background needed to understand the purpose of the presented work. First, we will outline the cell division cycle in order to understand what the main biomedical interest of our work is. This will be presented regarding healthy cells. Furthermore, we give a brief description of aberrant cells in section 2.2 on page 5, which we later want to distinguish from healthy cells. Cell division requires the interaction of a multitude of proteins, regulating entry into the individual phases of the cell cycle (see figure 2). In particular, protein kinases transfering phosphate groups from one protein to another, and thereby leading to their activation, are essential for proper cell cycle progression. Recently the Aurora-family of kinases have been identified to play a major role in the cell cycle.

Three Aurora kinases have been identified: Aurora A (also known as STK15), Aurora B and Aurora C. Coordinate events for the positioning of the two spindle poles and the alignment of chromatids are regulated via Aurora A and Aurora B kinases, respectively. Clearly, disturbance of these coordinate events will lead to cell cycle disturbances and may be involved in development of chromosomal unstable cells, as seen in malignant transformation and several cancer entities.

Since the main research interest of our project partners is Aurora A, we will neglect other Aurora kinases and focus on Aurora A.

Aurora A is working during prophase (see figure 2.1 on the next page) and is required for the correct function of the centrosomes which serve as the main microtubule organising centre.

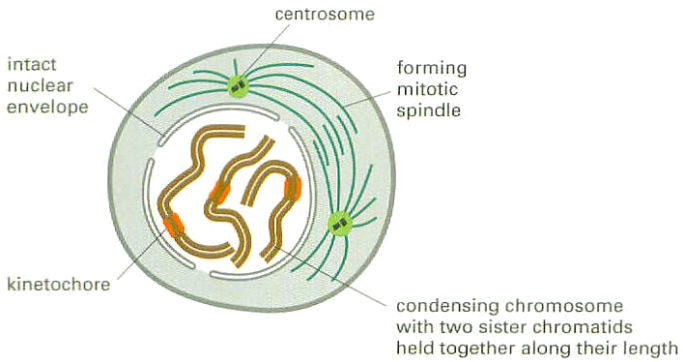

Figure 2.1: Prophase of a cell.

During the prophase of mitosis, the centrosomes migrate to opposite poles of the cell. The mitotic spindle then forms between the two centrosomes. Upon division, each daughter cell

receives one centrosome. Aberrant numbers of centrosomes in a cell have been associated with cancer.

2.1 Cell Division and the Cell Cycle

The process of mitosis can be divided into six phases as depicted in figure 2.1. These six stages are known as prophase, prometaphase, metaphase, anaphase, telophase and cytokinesis.

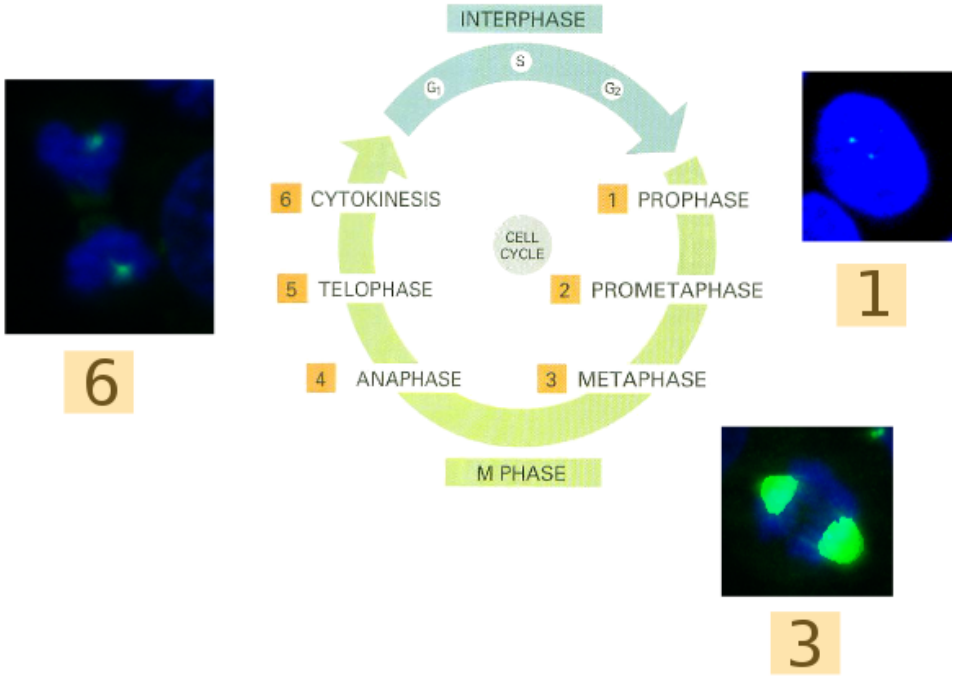

Figure 2.2: Overview of the cell cycle.

During mitosis, a mitotic spindle is assembled by using microtubules to tether together the mother centrosome to its daughter. The resulting mitotic spindle is then used to propel apart the sister chromosomes into what will become the two new daughter cells.
Aurora A is critical for proper formation of the mitotic spindle. It is required for the recruitment and activation of several different proteins important to the spindle formation. Without Aurora A the centrosome does not accumulate the quantity of γ-tubulin that normal centrosomes recruit prior to entering anaphase. Finally, Aurora A helps to orchestrate an exit from mitosis by contributing to the completion of cytokinesis- the process by which the cytoplasm of the parent cell is split into two daughter cells. During cytokinesis the mother centriole returns to the mid-body of the mitotic cell at the end of mitosis and causes the central microtubules to release from the mid-body. The release allows mitosis to run to completion.
Furthermore, Aurora A is also involved in the dynamics of centrosome maturation and their migration to form two opposite located spindle poles.
Aberrant high expression of Aurora A has been associated with supernumerary centrosomes and multipolar spindle poles during cell division of cancer cells. High levels of Aurora A have

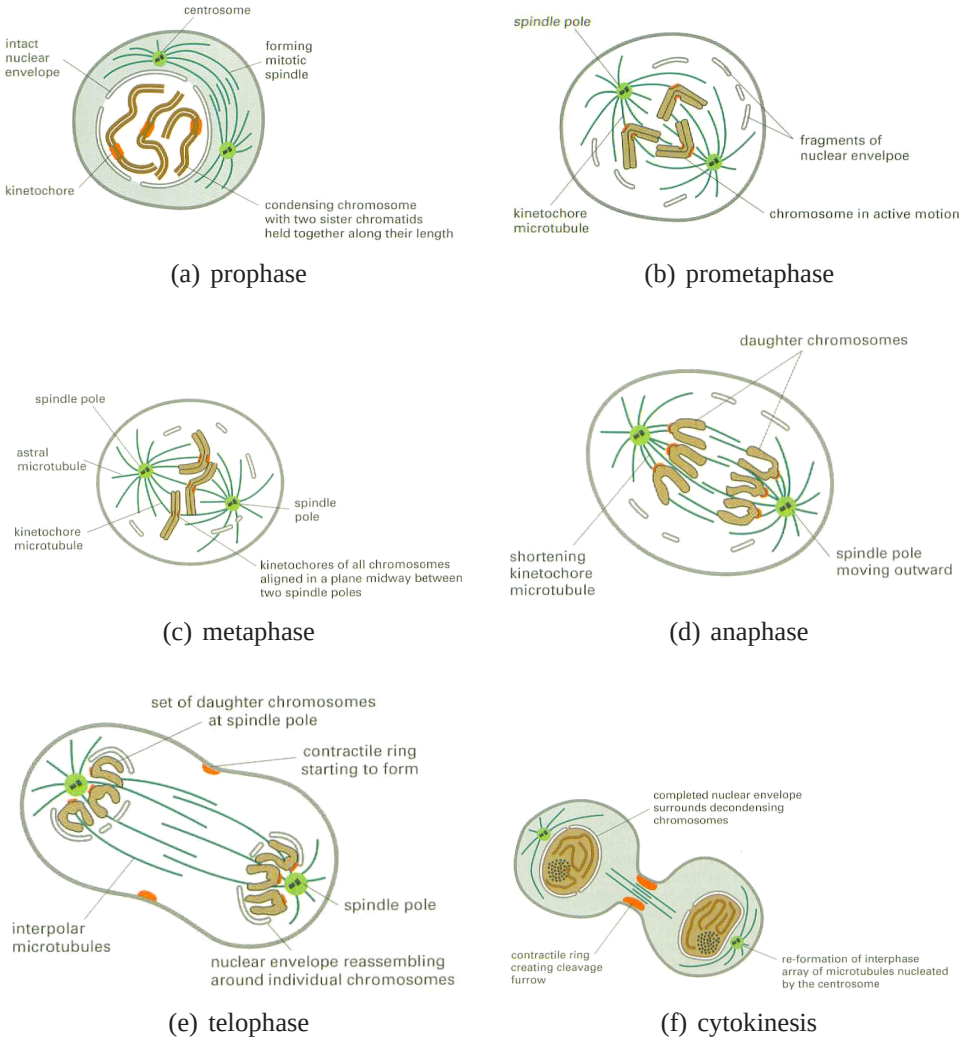

(a) prophase (b) prometaphase

(c) metaphase (d) anaphase

(e) telophase (f) cytokinesis

Figure 2.3: Six different cell division stages.

been observed in colorectal cancers, especially in those molecular subgroups of colorectal cancers that display chromosomal instability (see [GKW+06],[LWM+07]and [LKS+09]).

2.2 Cancer Cells and Aberrant Mitosis

Aurora A dysregulation has been associated with a high occurrence of cancer. Dysregulation of Aurora A may lead to cancer because Aurora A is required for the completion of cytokinesis. If the cell begins mitosis, it duplicates its DNA, but is then not able to divide into two separate cells, it becomes an aneuploid and contains more chromosomes than normal. Figure 2.4 on the next page shows a few examples of aberrant mitosis cells. More examples can be found in appendix D.1 on page 82.

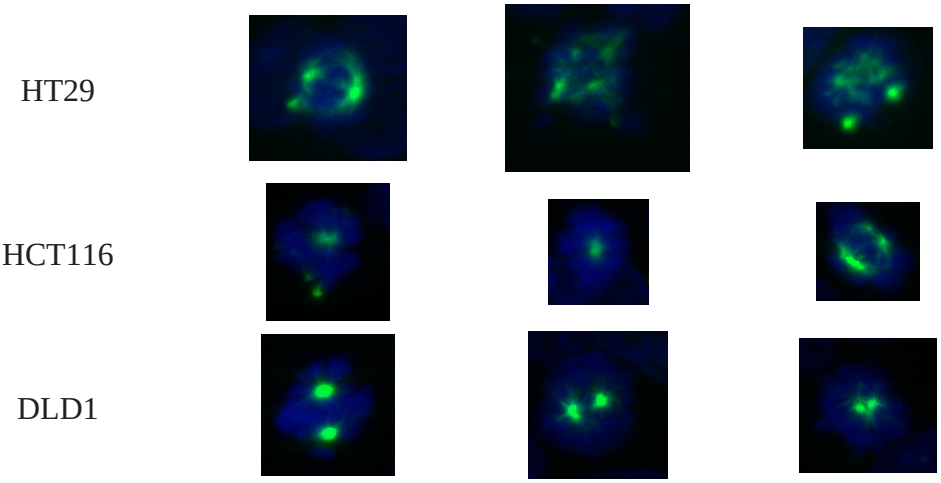

Figure 2.4: Examples of highly aberrant mitotic cells of three different identified cancer types.

2.3 Cell Lines

Cell lines are distinct families of cells grown in culture. Cells in the same line are typically clones. Different cell lines have different features which are useful in molecular biological applications. We used images of the following three cell lines (see `http://www.biotech.ist.unige.it`).

- HCT 116:

  Morphology: Epithelial-like

  Species: human male

  Tissue: colon

  Tumour: carcinoma

  Depositor: obtained from ATCC Properties: expressing xenobiotic metabolising enzymes; producing carcinoembryonic antigen

- DLD-1:

  Morphology: Epithelial Human colon adenocarcinoma

  Depositor: Obtained from ATCC, USA

  Derived from human colorectal adenocarcinoma. The cells have been used in the study of polar solvents on cell characteristics.

- HT 29:

  Morphology: Epithelial

  Human Caucasian colon adenocarcinoma grade II

Isolated from a primary tumour in a 44 year old Caucasian female. Forms a well-differentiated adenocarcinoma consistent with colony primary, grade I. Tumours also form in steroid treated hamsters.

3 Preliminaries

This chapter presents the theoretical background needed to understand the following chapters. Until a few exceptions we passed on most of the proofs or referred to its source. Most of the definitions and theorems where invented in [RB09] and [Rei09] and the interested reader is referred to these sources.

We will begin with a very basic definition.

Definition 3.0.1 (Equivariant Mapping)**.** *A mapping f between two set X and Y is called equivariant if f commutes with the group action of a given group $\mathcal{G}$.*

$$f(g \cdot x) = g \cdot f(x),\ \forall g \in \mathcal{G} \text{ and } x \in X$$

Or in other words, f is an equivariant mapping if the following diagram commutes for every $g \in \mathcal{G}$:

$$\begin{array}{ccc} X & \xrightarrow{g\cdot} & X \\ {\scriptstyle f}\downarrow & & \downarrow{\scriptstyle f} \\ Y & \xrightarrow[g\cdot]{} & Y \end{array}$$

$g\cdot : \mathcal{G} \times X \to X$, $(g, x) \mapsto gx$ denotes the group action of $\mathcal{G}$ on X (for Y respectively).

We will later need the following vector space definition.

Definition 3.0.2 (The vector space V_j)**.** *We define V_j as the complex $2j+1$ dimensional vector space represented by $\mathbb{C}^{2j+1}$. The standard basis of V_j is written as $\mathbf{e}_m^j$ for $m = -j, \ldots, j$.*

Elements of V_j are written in bold face, e.g. $\mathbf{v} \in V_j$, and the $2j+1$ components of $\mathbf{v}$ in unbold face $v_m \in \mathbb{C}$, where $m = -j, \ldots, j$. We treat V_j as a real vector space of dimension $2j+1$, despite the fact that the components of $\mathbf{v}$ might be complex. This means that V_j is only closed under weighted superpositions of real numbers. Therefore, components of $u \in V_j$ fulfil the property $\overline{u_m} = (-1)^m u_{-m}$. The corresponding "imaginary" space is denoted as $\mathbf{i}V_j$. We write the elements $\mathbf{w} \in \mathbf{i}V_j$ as $\mathbf{w} = \mathbf{i}\mathbf{v}$, whereas $\mathbf{v} \in V_j$. Analogue to elements of V_j, the elements $\mathbf{w} \in \mathbf{i}V_j$ fulfil always $\overline{w_m} = (-1)^{m+1} w_{-m}$. Hence the whole $\mathbb{C}^{2j+1}$ can be written as the direct sum of these two spaces $\mathbb{C}^{2j+1} = V_j \oplus \mathbf{i}V_j$.
Let $\mathbf{r} = (x, y, z)^T \in \mathbb{R}^3$ be the standard coordinate vector. One can relate $\mathbf{r}$ to the complex valued spherical coordinate $\mathbf{u} \in V_1$ in an unitary way:

$$\mathbf{u} = \begin{pmatrix} \frac{1}{\sqrt{2}}(x - \mathbf{i}y) \\ z \\ -\frac{1}{\sqrt{2}}(x + \mathbf{i}y) \end{pmatrix} = \begin{pmatrix} \overline{w} \\ z \\ -w \end{pmatrix} = \mathbf{S}\mathbf{r} \in V_1 \ ,$$

whereas $w = x + \mathbf{i}y$. $\mathbf{S}$ is an unitary coordinate transformation given by the matrix

$$\mathbf{S} = \frac{1}{\sqrt{2}} \begin{pmatrix} 1 & -\mathbf{i} & 0 \\ 0 & 0 & \sqrt{2} \\ -1 & -\mathbf{i} & 0 \end{pmatrix} \tag{3.1}$$

3.1 Irreducible Representations of Elements of SO(3)

The representation of a group $\mathcal{G}$ is a mapping of the elements $g \in \mathcal{G}$ onto a set of matrices $\mathbf{D}(g)$ of dimension d, such that the product rule still holds (group homomorphism):

$$\mathbf{D}(g_1 g_2) = \mathbf{D}(g_1)\mathbf{D}(g_2) \, .$$

We will need the definition of irreducible representations of elements of SO(3).

Definition 3.1.1 (Wigner D-matrices and the vector space V_j)**.** *Let $\mathbf{D}_g^j$ be the irreducible representation of elements $g \in$ SO(3) that act on the vector space V_j . The representations $\mathbf{D}_g^j$ are unitary*

$$(\mathbf{D}_g^j)^T \mathbf{D}_g^j = \mathbf{I}$$

The $\mathbf{D}_g^j$ are called the Wigner D-matrix. The components of $\mathbf{D}_g^j$ are written D_{mn}^j.
The relation between $\mathbf{D}_g^1$ and the real valued rotation matrix $\mathbf{U}_g \in \mathbb{R}^{3\times 3}$ is given by

$$\mathbf{D}_g^1 = \mathbf{S}\mathbf{U}_g\mathbf{S}^T$$

for $\mathbf{S}$ according to equation (3.1).

3.2 Spherical Tensor Analysis

In this section we will give all basic definition and theorems which are essential for spherical tensor analysis.

Definition 3.2.1 (Spherical Tensor Field)**.** *We call a function $\mathbf{f} : \mathbb{R}^3 \to V_j$ a spherical tensor field of rank j if it transforms with respect to rotations as*

$$\left(g \cdot \mathbf{f}\right)(\mathbf{r}) := \mathbf{D}_g^j \mathbf{f}\left(\mathbf{U}_g^T \mathbf{r}\right) \tag{3.2}$$

for all $g \in$ SO(3). The space of all spherical tensor fields of rank j is denoted as $\mathcal{T}_j$.

The next definition will give us a basic tool for combining tensors of different ranks.

Definition 3.2.2 (Spherical Tensor Coupling)**.** *For $j \geq 0$ we define a family of bilinear forms of type*

$$\circ_j : V_{j_1} \times V_{j_2} \to V_j$$

whereas $j_1, j_2 \in \mathbb{N}$ have to be chosen according the triangle inequality

$$|j_1 - j_2| \leq j \leq j_1 + j_2 \tag{3.3}$$

For $\mathbf{v} \in V_{j_1}$ and $\mathbf{w} \in V_{j_2}$, $\mathbf{v} \circ_j \mathbf{w}$ is defined by

$$(\mathbf{e}_m^j)^T(\mathbf{v} \circ_j \mathbf{w}) = \sum_{m=m_1+m_2} \langle jm \mid j_1 m_1, j_2 m_2 \rangle v_{m_1} w_{m_2}$$

whereas $\langle jm \mid j_1 m_1, j_2 m_2 \rangle$ are the Clebsch-Gordan coefficients.

This is just the ordinary angular momentum coupling known in quantum mechanics (see [Ros95] and [Tin04]). Note that the Clebsch-Gordan coefficients $\langle jm \mid j_1 m_1, j_2 m_2 \rangle$ are only non zero for $m = m_1 + m_2$. The most important and useful property of the above defined products is that they respect the rotations of their arguments. We will make use of this property in the following chapters. The following proposition will make this clear.

Proposition 3.2.1. *Let $j_1, j_2, j \in \mathbb{N}$ be chosen according to the triangle inequality (3.2). For any $\mathbf{v} \in V_{j_1}$ and $\mathbf{w} \in V_{j_2}$ and $g \in \mathsf{SO}(3)$ holds*

$$\left(\mathbf{D}_g^{j_1}\mathbf{v}\right) \circ_j \left(\mathbf{D}_g^{j_2}\mathbf{w}\right) = \mathbf{D}_g^j\left(\mathbf{v} \circ_j \mathbf{w}\right)$$

Proof. See [RB09] and [Rei07] □

We will present some other useful properties of the products defined by definition 3.2.2.

Proposition 3.2.2. *Let $j_1, j_2, j \in \mathbb{N}$ be chosen according to the triangle inequality (3.2). If $j + j_1 + j_2$ is even, then $\circ_j$ is symmetric and antisymmetric otherwise. The space V_j is closed under symmetric products but not for antisymmetric products. Then we have for $\mathbf{v} \in V_{j_1}$ and $\mathbf{w} \in V_{j_2}$*

$$j + j_1 + j_2 \text{ is even} \Rightarrow \mathbf{v} \circ_j \mathbf{w} \in V_j$$

$$j + j_1 + j_2 \text{ is odd} \Rightarrow \mathbf{v} \circ_j \mathbf{w} \in \mathbf{i}V_j$$

Proof. See [RB09] and [Rei07] □

Definition 3.2.3 (Normalised Symmetric Products)**.** *For $j \geq 0$, $|j_1 - j_2| \leq j \leq j_1 + j_2$ and $j + j_1 + j_2$ even, we define a family of symmetric bilinear forms $\bullet_j : V_{j_1} \times V_{j_2} \to V_j$ by*

$$\mathbf{v} \bullet_j \mathbf{w} := \frac{1}{\langle j\,0 \mid j_1 0, j_2 0 \rangle}\, \mathbf{v} \circ_j \mathbf{w}$$

Note that $\langle j0 \mid j_1 0, j_2 0 \rangle$ are only non zero for $j + j_1 + j_2 =$ even.

There are some special cases which we will now summarise.

For $\bullet_0$ the arguments have to be of the same rank in order to fulfil the triangle inequality, e.g. $\mathbf{v}, \mathbf{w} \in V_k$. In this case $\bullet$ coincides with the standard inner product:

$$\mathbf{v} \bullet_0 \mathbf{w} = \sum_{m=-k,\ldots,k} (-1)^m v_m w_{-m} = \mathbf{w}^T \mathbf{v} \,.$$

For $j = j_2$ and $j_1 = 0$, e.g. $\mathbf{v} \in V_0$ and $\mathbf{w} \in V_j$, $\bullet$ reduces to the standard scalar multiplication:

$$\mathbf{v} \bullet_j \mathbf{w} = v_0 \mathbf{w} \,.$$

The following has found to be very useful in the context of multi-channel image filters.
For $j = j_1 = j_2 = 1$ and $\mathbf{v} = \mathbf{S}\mathbf{b},\ \mathbf{w} = \mathbf{S}\mathbf{c} \in V_1$ and $\mathbf{b},\ \mathbf{c} \in \mathbb{R}^3$ it holds

$$-\mathbf{i}(\mathbf{v} \circ_1 \mathbf{w}) = \frac{1}{\sqrt{2}} \mathbf{S}\,(\mathbf{b} \times \mathbf{c}) \tag{3.4}$$

$\times$ denotes the cross product.

Proof.

$$\begin{aligned}
-\mathbf{i}(\mathbf{v} \circ_1 \mathbf{w}) &= -\mathbf{i} \begin{pmatrix} \sum_{-1=m_1+m_2} \langle 1-1 \mid 1m_1, 1m_2 \rangle v_{m_1} w_{m_2} \\ \sum_{0=m_1+m_2} \langle 10 \mid 1m_1, 1m_2 \rangle v_{m_1} w_{m_2} \\ \sum_{1=m_1+m_2} \langle 11 \mid 1m_1, 1m_2 \rangle v_{m_1} w_{m_2} \end{pmatrix} \\
&= -\mathbf{i} \begin{pmatrix} \langle 1-1 \mid 1-1, 10 \rangle v_{-1} w_0 + \langle 1-1 \mid 10, 1-1 \rangle v_0 w_{-1} \\ \langle 10 \mid 1-1, 11 \rangle v_{-1} w_1 + \langle 10 \mid 11, 1-1 \rangle v_1 w_{-1} \\ \langle 11 \mid 10, 11 \rangle v_0 w_1 + \langle 10 \mid 11, 10 \rangle v_1 w_0 \end{pmatrix} \\
&= -\mathbf{i} \begin{pmatrix} -\frac{1}{\sqrt{2}} v_{-1} w_0 + \frac{1}{\sqrt{2}} v_0 w_{-1} \\ -\frac{1}{\sqrt{2}} v_{-1} w_1 + \frac{1}{\sqrt{2}} v_1 w_{-1} \\ -\frac{1}{\sqrt{2}} v_0 w_1 + \frac{1}{\sqrt{2}} v_1 w_0 \end{pmatrix} \\
&= -\frac{\mathbf{i}}{\sqrt{2}} \begin{pmatrix} \frac{1}{\sqrt{2}}((-b_x + \mathbf{i}b_y)c_z + b_z(c_x - \mathbf{i}c_y)) \\ \frac{1}{2}((-b_x + \mathbf{i}b_y)(-c_x - \mathbf{i}c_y) + (-b_x - \mathbf{i}b_y)(c_x - \mathbf{i}c_y)) \\ \frac{1}{\sqrt{2}}(-b_z(-c_x - \mathbf{i}c_y) + (-b_x - \mathbf{i}b_y)c_z) \end{pmatrix} \\
&= -\frac{\mathbf{i}}{\sqrt{2}} \begin{pmatrix} \frac{1}{\sqrt{2}}((b_z c_x - b_x c_z) + \mathbf{i}(b_y c_z - b_z c_y)) \\ \mathbf{i}(b_x c_y - b_y c_x) \\ \frac{1}{\sqrt{2}}((-b_x c_z + b_z c_x) + \mathbf{i}(-b_y c_z + b_z c_y)) \end{pmatrix} \\
&= \frac{1}{2} \begin{pmatrix} (b_y c_z - b_z c_y) - \mathbf{i}(b_z c_x - b_x c_z) \\ \sqrt{2}(b_x c_y - b_y c_x) \\ -(b_z c_y - b_y c_z) - \mathbf{i}(b_z c_x - b_x c_z) \end{pmatrix} \\
&= \frac{1}{\sqrt{2}} \mathbf{S} \begin{pmatrix} b_y c_z - b_z c_y \\ b_z c_x - b_x c_z \\ b_x c_y - b_y c_x \end{pmatrix} \\
&= \frac{1}{\sqrt{2}} \mathbf{S}\,(\mathbf{b} \times \mathbf{c})
\end{aligned}$$

□

The previously introduced products are giving us the ability to not only coupling tensors of different, but also coupling tensor fields of different ranks.

Proposition 3.2.3. *Let* $\mathbf{v} \in \mathcal{T}_{j_1}$ *and* $\mathbf{w} \in \mathcal{T}_{j_2}$ *and* $j \in \mathbb{N}$ *be chosen such that* $\left|j_1 - j_2\right| \leq j \leq j_1 + j_2$ *then*

$$\mathbf{f}(\mathbf{r}) := \mathbf{v}(\mathbf{r}) \circ_j \mathbf{w}(\mathbf{r})$$

defines a tensor field of rank j*, i.e.* $\mathbf{f} \in \mathcal{T}_j$

Proof. Since we have $\mathbf{v}(\mathbf{r}) \in V_{j_1}$ and $\mathbf{w}(\mathbf{r}) \in V_{j_2}$, we know that $(\mathbf{v}(\mathbf{r}) \circ_j \mathbf{w}(\mathbf{r})) \in V_j$. Since this holds for all $\mathbf{r} \in \mathbb{R}^3$ and the properties of $\circ_j$, we have that $(\mathbf{v} \circ_j \mathbf{w}) : \mathbb{R}^3 \to \mathcal{T}_{j_1}$ defines a spherical tensor field. □

Tensor fields can also be combined by convolution, which the next proposition will show. The advantage of combining tensor fields by convolution is, that the so defined ”convolution” products also respect translation in a certain sense.

Proposition 3.2.4. *Let* $\mathbf{v} \in \mathcal{T}_{j_1}$ *and* $\mathbf{w} \in \mathcal{T}_{j_2}$ *and* j *be chosen such that* $|j_1 - j_2| \leq j \leq j_1 + j_2$*, then*

$$(\mathbf{v} \widetilde{\circ}_j \mathbf{w})(\mathbf{r}) := \int_{\mathbb{R}^3} \mathbf{v}(\mathbf{r}' - \mathbf{r}) \circ_j \mathbf{w}(\mathbf{r}')\, d\mathbf{r}'$$

is in $\mathcal{T}_j$*, i.e. a tensor field of rank* j*.*

Considering the behaviour of $\circ_j$ and $\widetilde{\circ}_j$ under a translation τ

$$(\tau\mathbf{f})(\mathbf{r}) := \mathbf{f}(\mathbf{r} - \mathbf{t}_\tau)\,,$$

leads to the following two relations:

$$(\tau\mathbf{v}) \circ_j (\tau\mathbf{w}) = \tau(\mathbf{v} \circ_j \mathbf{w}) \tag{3.5}$$

$$\mathbf{v} \widetilde{\circ}_j (\tau\mathbf{w}) = (\tau\mathbf{v}) \widetilde{\circ}_j \mathbf{w} = \tau(\mathbf{v} \widetilde{\circ}_j \mathbf{w}) \tag{3.6}$$

3.3 Spherical and Solid Harmonics

We denote the spherical harmonics by

$$\mathbf{Y}^j : S^2 \to V_j\,.$$

We write $\mathbf{Y}^j(\mathbf{r})$, where $\mathbf{r}$ may be an element of $\mathbb{R}^3$, although $\mathbf{Y}^j(\mathbf{r})$ is independent of the magnitude of $\mathbf{r}$. This has the advantage that we can interpret them as spherical tensor field.

We know that the $\mathbf{Y}^j$ provide an orthogonal basis of scalar functions on the 2-sphere S^2. Thus, any real scalar field $f \in \mathcal{T}_0$ can be expanded in terms of spherical harmonics in a unique manner. One important and useful property is that $\mathbf{Y}^j = \mathbf{Y}^{j_1} \bullet_j \mathbf{Y}^{j_2}$. We can use this formula to iteratively compute higher order $\mathbf{Y}^j$ from given lower order ones. Note that $\mathbf{Y}^0 = 1$ and

$\mathbf{Y}^1 = \mathbf{Sr}$, where $\mathbf{r} \in S^2$.
Another important property that each $\mathbf{Y}^j$, interpreted as a tensor field of rank j is a fix-point with respect to rotations, i.e.

$$(g\mathbf{Y}^j)(\mathbf{r}) = \mathbf{Y}^j(\mathbf{r}), \text{ for all } g \in \mathsf{SO}(3) \tag{3.7}$$

or in other words: $\mathbf{Y}^j(\mathbf{U}_g\mathbf{r}) = \mathbf{D}_g^j\mathbf{Y}^j(\mathbf{r})$.

The spherical harmonics naturally arise from the solutions from the Laplace equation as the so called solid harmonics

$$\mathbf{R}^j(\mathbf{r}) := r^j\mathbf{Y}^j(\mathbf{r})$$

The generalisation $\mathbf{R}_i^j(\mathbf{r}) := r^{j+i}\mathbf{Y}^{j-i}(\mathbf{r})$ is a complete basis for the analytical functions $L_2(\mathbb{R}^3)$.

Note that the fix point property also holds for the solid harmonics.

3.4 Spherical Derivatives

We will later need the concept of spherical derivatives for the harmonic filter framework.

Proposition 3.4.1 (Spherical Derivatives)**.** *Let $\mathbf{f} \in \mathcal{T}_j$ be a tensor field. The spherical up-derivative $\boldsymbol{\nabla}^1 : \mathcal{T}_j \to \mathcal{T}_{j+1}$ and the down-derivative $\boldsymbol{\nabla}_1 : \mathcal{T}_j \to \mathcal{T}_{j-1}$ are defined as*

$$\boldsymbol{\nabla}^1\mathbf{f} := \nabla \bullet_{j+1} \mathbf{f} \tag{3.8}$$
$$\boldsymbol{\nabla}_1\mathbf{f} := \nabla \bullet_{j-1} \mathbf{f}, \tag{3.9}$$

where

$$\nabla = (\frac{1}{\sqrt{2}}(\partial_x - \mathbf{i}\partial_y), \partial_z, -\frac{1}{\sqrt{2}}(\partial_x + \mathbf{i}\partial_y))$$

is the spherical gradient and $\partial_x, \partial_y, \partial_z$ the standard partial derivatives.

Proof. We have to show that $\boldsymbol{\nabla}^1\mathbf{f} \in \mathcal{T}_{j+1}$, i.e.

$$\boldsymbol{\nabla}^1(\mathbf{D}_g^j\mathbf{f}(\mathbf{U}_g^T\mathbf{r})) = \mathbf{D}_g^{j+1}(\boldsymbol{\nabla}^1\mathbf{f})(\mathbf{U}_g^T\mathbf{r})$$

and $\boldsymbol{\nabla}_1\mathbf{f} \in \mathcal{T}_{j-1}$

$$\boldsymbol{\nabla}_1(\mathbf{D}_g^j\mathbf{f}(\mathbf{U}_g^T\mathbf{r})) = \mathbf{D}_g^{j-1}(\boldsymbol{\nabla}_1\mathbf{f})(\mathbf{U}_g^T\mathbf{r})$$

Both statements are proved just by using the properties of $\bullet$. □

Note. For $\mathbf{f} \in \mathcal{T}_0$ the spherical up-derivative is just the spherical gradient $\nabla\mathbf{f} = \boldsymbol{\nabla}^1\mathbf{f}$. A consecutive application of up- and down-derivatives for $f \in \mathcal{T}_0$ is equivalent with applying the Laplace operator:

$$\boldsymbol{\nabla}_1\boldsymbol{\nabla}^1\mathbf{f} = \Delta\mathbf{f}$$

In the Fourier domain the spherical derivatives act by point-wise $\bullet$-multiplications with a solid harmonic $\mathbf{i}k\mathbf{Y}^1(\mathbf{k}) = \mathbf{i}\mathbf{R}^1(\mathbf{k}) = \mathbf{iSk}$ where $k = \|\mathbf{k}\|$ denotes the frequency magnitude:

Proposition 3.4.2 (Fourier Representation)**.** *Let* $\widetilde{\mathbf{f}}(\mathbf{k})$ *be the Fourier transformation of some* $\mathbf{f} \in \mathcal{T}_\ell$ *and* $\widetilde{\boldsymbol{\nabla}}$ *representations of the spherical derivative in the Fourier domain that are implicitly defined by* $(\widetilde{\boldsymbol{\nabla}\mathbf{f}}) = \widetilde{\boldsymbol{\nabla}}\widetilde{\mathbf{f}}$*, then*

$$\widetilde{\boldsymbol{\nabla}^1}\widetilde{\mathbf{f}}(\mathbf{k}) = \mathbf{i}\mathbf{R}^1(\mathbf{k}) \bullet_{\ell+1} \widetilde{\mathbf{f}}(\mathbf{k}) \tag{3.10}$$

$$\widetilde{\boldsymbol{\nabla}}_1\widetilde{\mathbf{f}}(\mathbf{k}) = \mathbf{i}\mathbf{R}^1(\mathbf{k}) \bullet_{\ell-1} \widetilde{\mathbf{f}}(\mathbf{k}). \tag{3.11}$$

Proof. By using the ordinary Fourier correspondence of the partial derivative, $\widetilde{\partial_x \mathbf{f}} = \mathbf{i}k_x\widetilde{\mathbf{f}}$, we can verify for the spherical gradient ∇ that

$$\widetilde{\nabla} = \mathbf{i}\mathbf{S}\mathbf{k} = \mathbf{i}\mathbf{R}^1(\mathbf{k})$$

and hence

$$\widetilde{\boldsymbol{\nabla}^1\mathbf{f}} = (\widetilde{\nabla \bullet_{\ell+1} \mathbf{f}}) = \widetilde{\nabla} \bullet_{\ell+1} \widetilde{\mathbf{f}} = \mathbf{i}\mathbf{R}^1(\mathbf{k}) \bullet_{\ell+1} \widetilde{\mathbf{f}}$$

which was to be shown (see [Rei07]). □

Equation (3.10) and (3.11) are direct consequences of the Fourier correspondences for the ordinary partial derivatives.

The generalisation higher orders is only true for scalar fields and is presented by the next proposition.

Proposition 3.4.3 (Multiple Spherical Derivatives)**.** *For* $n \geq i$ *we define* $\boldsymbol{\nabla}_i^n : \mathcal{T}_0 \to \mathcal{T}_{n-i}$ *by*

$$\boldsymbol{\nabla}_i^n := \boldsymbol{\nabla}_i \boldsymbol{\nabla}^n := \underbrace{\boldsymbol{\nabla}_1 \dots \boldsymbol{\nabla}_1}_{i-times} \underbrace{\boldsymbol{\nabla}^1 \dots \boldsymbol{\nabla}^1}_{n-times}.$$

In the Fourier domain these multiple derivatives act by

$$(\widetilde{\boldsymbol{\nabla}}_i^n \widetilde{f})(\mathbf{k}) = (\mathbf{i})^{n+i}\, \mathbf{R}_i^n(\mathbf{k}) \widetilde{f}(\mathbf{k}). \tag{3.12}$$

Using this one can show that $\boldsymbol{\nabla}_i^n = \boldsymbol{\nabla}^{n-i}\Delta^i$*, where* Δ *is the Laplace operator.*

Proof. See [Rei07] □

We will later need the following commuting property for convolutions.

Proposition 3.4.4 (Commuting Property for Convolutions)**.** *Let* $\mathbf{A} \in \mathcal{T}_k$ *and* $\mathbf{B} \in \mathcal{T}_j$ *be arbitrary spherical tensor fields then*

$$(\boldsymbol{\nabla}^\ell \mathbf{A}) \widetilde{\bullet}_J \mathbf{B} = \mathbf{A} \widetilde{\bullet}_J (\boldsymbol{\nabla}_\ell \mathbf{B}) \tag{3.13}$$

$$(\boldsymbol{\nabla}^\ell \mathbf{A}) \widetilde{\bullet}_L \mathbf{B} = \mathbf{A} \widetilde{\bullet}_L (\boldsymbol{\nabla}^\ell \mathbf{B}) \tag{3.14}$$

where $J = j - (\ell + k)$ *and* $L = j + \ell + k$*.*

Proof. See [RB09] □

3.5 Spherical Gaussian Derivatives

This section summarises the most important relations of spherical derivatives Gaussian functions.

Proposition 3.5.1. *The Gaussian windowed harmonic of width σ is defined as*

$$\mathbf{G}_\sigma^j(\mathbf{r}) := \frac{1}{\sigma^3}\left(\frac{-r}{\sigma^2}\right)^j \mathbf{Y}^j(\mathbf{r}) e^{-\frac{r^2}{2\sigma^2}},$$

then, the Fourier transformation of $\mathbf{G}^j(\mathbf{r})$ is given by

$$\tilde{\mathbf{V}}_\sigma^j(\mathbf{k}) = \langle e^{\mathbf{i}\mathbf{k}^T\mathbf{r}}, \mathbf{G}^j(\mathbf{r})\rangle_{L_2} = (\mathbf{i}k)^j \mathbf{Y}^j(\mathbf{k}) e^{-\frac{(\sigma k)^2}{2}}.$$

The following corollary will show that the $\mathbf{G}^j$ are just the j-th order spherical derivatives of a Gaussian.

Corollary 3.5.1 (Homogenous Spherical Gaussian Derivative)**.** *The homogeneous spherical derivative $\boldsymbol{\nabla}^j$ of a Gaussian is given by*

$$\boldsymbol{\nabla}^j e^{-\frac{r^2}{2\sigma^2}} = \sigma^3 \mathbf{G}_\sigma^j(\mathbf{r}) = \left(-\frac{1}{\sigma^2}\right)^j \mathbf{R}^j(\mathbf{r})\, e^{-\frac{r^2}{2\sigma^2}}$$

We use the convention $\mathbf{G}_\sigma^0 = G_\sigma = \frac{1}{(\sqrt{2\pi}\sigma)^3} e^{-\frac{r^2}{2\sigma^2}}$.
This also implies that for small σ the inner products with such $\mathbf{G}_\sigma^j$ tend towards the derivative, meaning

$$(-1)^j \langle \mathbf{G}_\sigma^j, f\rangle_{L_2} \overset{\sigma\to 0}{\longrightarrow} \left(\boldsymbol{\nabla}^j f\right)|_{\mathbf{r}=0}$$

for some $f \in \mathcal{T}_0$. Another implication is that convolutions with the $\mathbf{G}_\sigma^j$ are derivatives of smoothed functions

Corollary 3.5.2 (Smooth Derivatives)**.** *Let $f \in \mathcal{T}_0$ be a scalar-valued tensor field, then it holds*

$$\mathbf{G}_\sigma^j * f = \boldsymbol{\nabla}^j f_s,$$

where $f_s = G_\sigma * f = \frac{1}{\sigma^3} e^{-\frac{r^2}{2\sigma^2}} * f$ is the Gaussian-smoothed tensor field.

Proof. Using associativity and commutativity of convolutions, then in the Fourier domain holds:

$$\begin{aligned}\widetilde{\mathbf{G}}_{\sigma_1}^j \widetilde{f} &= \left((\mathbf{i}k)^j \mathbf{Y}^j(\mathbf{k}) e^{-\frac{(\sigma k)^2}{2}}\right)\widetilde{f} \\ &= (\mathbf{i}k)^j \mathbf{Y}^j(\mathbf{k}) \bullet_j \underbrace{\left(e^{-\frac{(\sigma k)^2}{2}}\widetilde{f}\right)}_{\tilde{f}_s} = \widetilde{\boldsymbol{\nabla}}^j \tilde{f}_s.\end{aligned}$$

Which proves the assertion. □

4 Tensor Voting and Harmonic Filters

This chapter introduces the theory of SE(3)-equivariant non-linear filters for generic feature and object detection [Rei09]. The goal is to build non-linear image filters that are equivariant to Euclidean motion. It is in principle the 3D analogy to the filter developed in [RB08] for the 2D case.
In section 4.1 we will give some basic definitions and give an introduction to the harmonic filter as developed in [Rei09]. Section 4.2 on page 19 will give an alternative formulation of the harmonic filter based on spherical derivatives (see 3.4 on page 14) that will lead to a fast implementation. In section 4.4 on page 24 we will give an extension to the harmonic filter that makes it possible to use higher order tensor fields as input to the filter. In section 4.5 on page 25 we will show how to extend harmonic filters to multi-channel input, and finally in section 4.6 on page 27 we will show how to extend the filter algorithm by making use of antisymmetric tensor products.

4.1 Harmonic Filters

Let us begin with the definition of a SE(3)-equivariant image filter.

Definition 4.1.1 (SE(3)-Equivariant Image Filter)**.** *An image filter* $\mathbf{F}$ *is a mapping from* $\mathcal{T}_{j_1}$ *onto* $\mathcal{T}_{j_2}$*. Such a mapping is called* SE(3)*-equivariant if* $\mathbf{F}\{gf\} = g\mathbf{F}\{f\}$ *for all* $g \in SE(3)$ *and* $f \in \mathcal{T}_{j_1}$*.*

In case of the harmonic filter we will focus on tensor fields $f \in \mathcal{T}_0$ (scalar fields) and elements of $\mathcal{T}_1$ (vector fields, see section 4.4 on page 24). Hence we will give a specialised definition of 4.1.1.

Definition 4.1.2 (SE(3)-Equivariant Scalar Image Filter)**.** *A scalar image filter* $\mathbf{F}$ *is a mapping from* $\mathcal{T}_0$ *onto* $\mathcal{T}_0$*. Such a mapping is called* SE(3)*-equivariant if* $\mathbf{F}\{gf\} = g\mathbf{F}\{f\}$ *for all* $g \in SE(3)$ *and* $f \in \mathcal{T}_0$*.*

The harmonic filter algorithm can be divided up into three steps:

First, compute for each position in the 3D space the projection onto the Gaussian windowed harmonic basis $\mathbf{G}_\sigma^j$ for $j = 0, \ldots, n$. This is achieved by calculating the convolution of the image f with the harmonic basis

$$\mathbf{p}^j := \mathbf{G}_\sigma^j * f \tag{4.1}$$

The set of projections $\mathbf{p}^j$ can be interpreted as a kind of local descriptor images, where the set of $[\mathbf{p}^0(\mathbf{r}), \mathbf{p}^1(\mathbf{r}), \ldots, \mathbf{p}^n(\mathbf{r})]$ of coefficients describe the harmonic part of the neighbourhood

of the voxel $\mathbf{r}$. Note that the resulting projections $\mathbf{p}^j$ are elements of $\mathcal{T}_j$ and as a consequence $\mathbf{p}^j(\mathbf{r}) \in V_j$.

Secondly, for each voxel these projections are mapped onto some new harmonic descriptors

$$\mathbf{N}^j(\mathbf{r}) := \mathbf{N}^j[\mathbf{p}^0(\mathbf{r}), \mathbf{p}^1(\mathbf{r}), \ldots, \mathbf{p}^n(\mathbf{r})] \tag{4.2}$$

which can be interpreted as a local expansion of a kind of voting function that contributes into the neighbourhood of $\mathbf{r}$. The voting function is chosen as a Gaussian-windowed harmonic function (see [Rei09]) and therefore the contribution of the voter at voxel $\mathbf{r}'$ to position $\mathbf{r}$ is :

$$\begin{aligned} V_{\mathbf{r}'}(\mathbf{r}) &= G_\eta(\mathbf{r}-\mathbf{r}') \sum_{j=0}^{\infty} (\mathbf{N}^j(\mathbf{r}'))^T \mathbf{R}^j(\mathbf{r}-\mathbf{r}') \\ &= G_\eta(\mathbf{r}-\mathbf{r}') \sum_{j=0}^{\infty} \mathbf{N}^j(\mathbf{r}') \bullet_0 \mathbf{R}^j(\mathbf{r}-\mathbf{r}') \,. \end{aligned} \tag{4.3}$$

The third and final step is to collect the contribution from all pixels $\mathbf{r}'$ in an additive way

$$\begin{aligned} \mathbf{F}\{f\}(\mathbf{r}) &:= \int_{\mathbb{R}^3} V_{\mathbf{r}'}(\mathbf{r}) d\mathbf{r}' \\ &= \sum_{j=0}^{n} \int_{\mathbb{R}^3} G_\eta(\mathbf{r}-\mathbf{r}') (\mathbf{N}^j(\mathbf{r}') \bullet_0 \mathbf{R}^j(\mathbf{r}-\mathbf{r}')) \\ &= \sum_{j=0}^{n} \int_{\mathbb{R}^3} \mathbf{G}_\eta^j(\mathbf{r}-\mathbf{r}') \bullet_0 \mathbf{N}^j(\mathbf{r}') \\ &= \sum_{j=0}^{n} \mathbf{G}_\eta^j \,\widetilde{\bullet}_0\, \mathbf{N}^j. \end{aligned} \tag{4.4}$$

Before we go into further details, we have to show that a filter defined by equation (4.4) is a filter in the sense of definition 4.1.1 on the previous page. In order to ensure SE(3)-equivariance, $\mathbf{N}^j[\cdot]$ has to fulfil the following definition:

Definition 4.1.3 (SE(3) equivariant mapping)**.** *A mapping $\mathbf{N}^j : V_0 \times \cdots \times V_n \to V_j$ is called equivariant if it behaves as*

$$\mathbf{N}^j \left[\mathbf{D}_g^0 \mathbf{p}^0, \ldots, \mathbf{D}_g^n \mathbf{p}^n\right] = \mathbf{D}_g^j \mathbf{N}^j \left[\mathbf{p}^0, \ldots, \mathbf{p}^n\right]$$

It is obvious that shifting f by τ results in shifted descriptors $\mathbf{p}^j$

$$\mathbf{G}_\sigma^j * (\tau f) = \tau(\mathbf{G}_\sigma^j * f) = \tau\, \mathbf{p}^j$$

Since $\mathbf{N}^j$ is working in a point-wise manner it holds for any translation:

$$\mathbf{N}^j[\tau\mathbf{p}^0, \ldots, \tau\mathbf{p}^j] = \tau\mathbf{N}^j[\mathbf{p}^0, \ldots, \mathbf{p}^j]$$

And finally, reconsidering equation (3.6) leads to the following

$$\mathbf{G}_\eta^j \,\widetilde{\bullet}_0\, (\tau \mathbf{N}^j) = \tau(\mathbf{G}_\eta^j \,\widetilde{\bullet}_0\, \mathbf{N}^j)$$

and proves the translation-equivariance.
We know from section 3.5 on page 16 that $\mathbf{G}_\eta^j$ are fix points with respect to rotations. The descriptor images $\mathbf{p}^j$ are spherical tensor fields of order j, because we have

$$\mathbf{G}_\sigma^j * (g f) = g(\mathbf{G}_\sigma^j * f)$$

Hence, $\mathbf{N}^j[\mathbf{p}^0, \ldots, \mathbf{p}^j]$ is also a spherical tensor field of order j.
Finally, using the fix point property of $\mathbf{G}_\eta^j$ and proposition 3.2.4 on page 13, we have that $\mathbf{F}\{f\} \in \mathcal{T}_0$ which proves the rotation-equivariance.

4.2 Differential Formulation of the Voting Function

We will use the spherical product $\bullet$ as the basic building block for the equivariant non-linearities $\mathbf{N}^j[\cdot]$. We define the non-linear voting function $\mathbf{N}^j[\cdot]$ as the sum of second order descriptor images $\mathbf{p}^j$

$$\mathbf{N}^j\left[\mathbf{p}^0, \ldots, \mathbf{p}^n\right] := \sum_{\substack{|j_1 - j_2| \le j \le j_1 + j_2 \\ j_1 + j_2 + j \text{ even} \\ j_1, j_2 \le n}} \alpha^j_{j_1, j_2}\, \mathbf{p}^{j_1} \bullet_j \mathbf{p}^{j_2} \tag{4.5}$$

where $\alpha^j_{j_1, j_2} \in \mathbb{R}$ are expansion coefficients. The order of the filter is defined as the order of product involved in $\mathbf{N}^j[\cdot]$ and is denoted by N. The computational most expensive parts of the filter given by equation (4.4) are the convolutions. On the one hand, one has to compute the projection onto the harmonic basis of the input image by convolution. On the other hand, the final collection step of all voters is done by convolution.
Reconsidering corollary 3.5.2 on page 16 shows that there is another way to compute projections onto the harmonic basis: by the use of the spherical derivative (see 3.4 on page 14).

Furthermore, we know from the commuting property for convolutions (see proposition 3.13 on page 15) that

$$\begin{aligned}
\sum_{j=0}^{n} \mathbf{G}_\eta^j \,\widetilde{\bullet}_0\, \mathbf{N}^j &= \sum_{j=0}^{n} (\boldsymbol{\nabla}^j G_\eta) \,\widetilde{\bullet}_0\, \mathbf{N}^j \\
&= \sum_{j=0}^{n} G_\eta \,\widetilde{\bullet}_0\, (\boldsymbol{\nabla}_j \mathbf{N}^j) \\
&= G_\eta * \sum_{j=0}^{n} \boldsymbol{\nabla}_j \mathbf{N}^j
\end{aligned}$$

We can reformulate the filter of equation (4.4) and give the final definition of the Harmonic Filter:

$$\mathbf{H}\{f\} := G_\eta * \sum_{j=0}^{n} \boldsymbol{\nabla}_j \mathbf{N}^j[\boldsymbol{\nabla}^0 f_s, \ldots, \boldsymbol{\nabla}^n f_s] \tag{4.6}$$

with $f_s = G_\sigma * f$ as in corollary 3.5.2 on page 16.

Algorithm 1 gives the computation of the filter in pseudo code notation. Note, that we just have to compute n spherical derivatives $\boldsymbol{\nabla}^1$ if we implement them by repeated applications (see proposition 3.4.3 on page 15 for details). Actually the same holds for the down-derivative $\boldsymbol{\nabla}_1$ if we follow Algorithm 1. In Figure 4.1 on the next page we illustrate the workflow of the filter.

Algorithm 1 Harmonic Filter Algorithm

Input: $f : \mathbb{R}^3 \to \mathbb{R}$
Output: $y : \mathbb{R}^3 \to \mathbb{R}, y := \mathbf{H}\{f\}$

Initialise $\mathbf{y}^n := 0 \in \mathcal{T}_n$
// compute projection onto harmonic basis
Convolve $\mathbf{p}^0 := G_\sigma * f$
for $j = 1 : n$ **do**
  $\mathbf{p}^j = \boldsymbol{\nabla}^1 \mathbf{p}^{j-1}$
end for
// compute harmonic descriptors
for $j = n : -1 : 1$ **do**
  $\mathbf{y}^{j-1} = \boldsymbol{\nabla}_1 \left(\mathbf{y}^j + \mathbf{N}^j \left[\mathbf{p}^0, \ldots, \mathbf{p}^j \right] \right)$
end for
Let $y := \mathbf{y}^0 + \mathbf{N}^0 \left[\mathbf{p}^0, \ldots, \mathbf{p}^j \right]$
// collect the contribution of all voters
Convolve $y := G_\eta * y$

Depending on the application they may or may not depend on the absolute intensity values of the input image. To become invariant against additive intensity changes one leaves out the zero order descriptor $\mathbf{p}^0$.
For robustness against illumination/contrast changes we introduce a soft normalisation of the first order descriptor $\mathbf{p}^1$:

$$\mathbf{p}^1(\mathbf{r}) = \frac{1}{\gamma + s_{\text{dev}}(\mathbf{r})} \boldsymbol{\nabla}^1 f(\mathbf{r}), \tag{4.7}$$

where $\gamma \in \mathbb{R}$ is a fixed regularisation parameter and $s_{\text{dev}}(\mathbf{r})$ denotes the standard deviation computed in a local window around $\mathbf{r}$. The normalisation makes the filter robust against multiplicative changes of gray values. The filter has three other parameters: the expansion degree N, the width of the input Gaussian σ and the output Gaussian η.

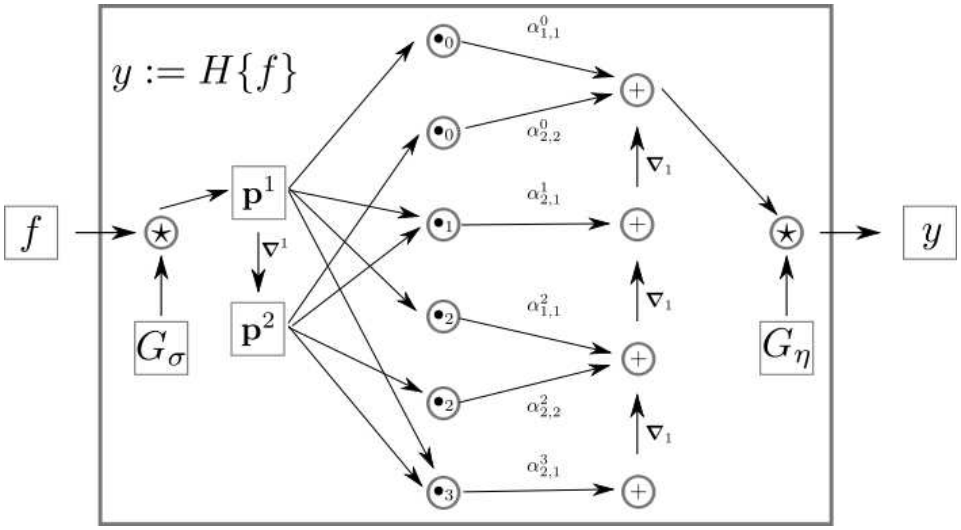

Figure 4.1: Workflow of the harmonic filter algorithm.

The parameter σ determines the size of the local features that vote for the centre of the object of interest. To assure that every pixel of the object can contribute to the output, the extent η of the voting function should be at least half the diameter of the object.

4.3 Training: Finding Optimal Filter Parameters

In order to find the filter coefficients α, we follow a linear least square fit. Suppose we want to train the filter for one input image $f \in \mathcal{T}_0$, then we have to minimise the following expression

$$J(\alpha) \quad = \quad \|\mathbf{L} - H\{f\}\|^2$$

where $\mathbf{L}$ is our label image, which contains ones at positions where we want high response of our filter, and zeros otherwise. Suppose our input image is given by its matrix representation $f \in \mathbb{R}^{m_1 \times m_2 \times m_3}$. We write the k-th computed feature in algorithm 1 on page 20 as

$$\mathbf{f}_k = \mathbf{vec}\left(G_\eta * \boldsymbol{\nabla}_\ell \left(\mathbf{p}^m \bullet_\ell \mathbf{p}^j \right)\right) \in \mathbb{R}^{m_1 \cdot m_2 \cdot m_3}$$

where F_k is k-th computed feature in algorithm 1 on page 20 written as vector. Assuming that we calculate n feature images, we can define the matrix

$$\mathbf{F} = (\mathbf{f}_1, \ldots, \mathbf{f}_n) \in \mathbb{R}^{(m_1 \cdot m_2 \cdot m_3) \times n}$$

Then we have that $\mathbf{vec}\left(\mathbf{H}\{f\}\right) = \sum_k \alpha_k \mathbf{f}_k$ and optimise the following expression

$$\begin{aligned} J(\alpha) \quad &= \quad \|\mathbf{vec}\,(\mathbf{L}) - \mathbf{vec}\left(H\{f\}\right)\|^2 \\ &= \quad \|\mathbf{vec}\,(\mathbf{L}) - \sum_k \alpha_k \mathbf{f}_k\|^2 \end{aligned}$$

The optimal α values arise from solving the normal equations:

$$\alpha = (\mathbf{F}^T\mathbf{F})^{(-1)}\mathbf{F}^T\mathbf{vec}\,(\mathbf{L})$$

Algorithm 2 Harmonic Filter Algorithm (Training)

Input: $f_i : \mathbb{R}^3 \to \mathbb{R}$, $i = 1, \ldots, M$, training examples
Input: $L_i : \mathbb{R}^3 \to \{0, 1\}$, $i = 1, \ldots, M$, corresponding label images
Input: $(m, j, \ell) \in \mathbb{N}^3$, tuple list of wanted products
Output: $\alpha \in \mathbb{R}^N$, filter coefficients (N = #tuples in product list)

Initialise $\mathbf{F} := \{\}$
Initialise $\mathbf{L} := \{\}$
// compute projection onto harmonic basis
for $i = 1 : M$ **do**
  Convolve $\mathbf{p_i}^0 := G_\sigma * f_i$
  for $j = 1 : n$ **do**
    $\mathbf{p_i}^j = \boldsymbol{\nabla}^1 \mathbf{p_i}^{j-1}$
  end for
  // compute local descriptors and collect
  for all $(m, j, \ell) \in$ products **do**
    $\mathbf{f}_k = G_\eta * \boldsymbol{\nabla}_\ell \, (\, \mathbf{p}_i^m \bullet_\ell \mathbf{p}_i^j \,)$
    $\mathbf{F} := \{\mathbf{F}, \mathbf{vec}(\mathbf{f}_k)\}$
    $\mathbf{L} := \{\mathbf{L}, \mathbf{vec}(L_i)\}$
    $k := k + 1$
  end for
end for
// linear least square fit
Let $\mathbf{C} := \mathbf{F}^T \, \mathbf{F}$
Let $\mathbf{b} := \mathbf{F}^T \, \mathbf{vec}(\mathbf{L})$
Solve $\mathbf{C} \, \alpha = \mathbf{b}$

4.4 Higher Order Tensor Fields

In this section we want to examine generalisations of the harmonic filter to higher order tensor fields for input as well as output. We will give an application for higher order input at the end of the current section.

The generalisation to tensor-valued input and output is indeed very simple. One has to construct a filter of type $\mathbf{F} : \mathcal{T}_{j_1} \to \mathcal{T}_{j_2}$ in the sense of definition 4.1.1 on page 17. According to the formulation we gave in section 4.2 on page 19 in order to compute the projection onto the harmonic basis, we can compute the descriptor images for a higher order input $\mathbf{f} \in \mathcal{T}_{j_1}$ as before by $\mathbf{p}^j = \boldsymbol{\nabla}^j(G_\sigma * \mathbf{f})$. The difference is that the resulting descriptor images have higher orders: $\mathbf{p}^j \in \mathcal{T}_{j+j_1}$.

We also have to adjust the local non-linear mappings $\mathbf{N}^j[\cdot]$ to

$$\mathbf{N}^j : \mathcal{T}_{o+j_1} \times \cdots \times \mathcal{T}_{n+j_1} \to \mathcal{T}_{j+j_1}$$

Actually, we can use the same formulation as in equation (4.6) to map the local non-linearities onto the output.

For getting higher order output one has to stop the loop in line 6 of algorithm 1 on page 20 at the desired output order. It is clear that only products $\bullet_j$ of order $j \geq j_1$ can be computed, when j_1 is the desired output order. One also has to have in mind, that the training gets even more complicated: one has to give higher order label images in training. A possible application of higher order output, e.g. for a filter of type $\mathbf{F} : \mathcal{T}_{j_1} \to \mathcal{T}_1$, could the prediction of local orientations, e.g. the orientation axis of the centrosomes of a (healthy) mitosis cell.

As mentioned above we will give an application of a filter of type $\mathbf{F} : \mathcal{T}_1 \to \mathcal{T}_0$, which we will define as the following:

Definition 4.4.1 (SE(3)-Equivariant Vectorial Image Filter)**.** *A vectorial image filter* $\mathbf{F}$ *is a mapping from* $\mathcal{T}_1$ *onto* $\mathcal{T}_0$*. Such a mapping is called* SE(3)*-equivariant if* $\mathbf{F}\{g f\} = g\mathbf{F}\{f\}$ *for all* $g \in SE(3)$ *and* $f \in \mathcal{T}_1$*.*

We used the gradient vector flow field ([XP97] and [XP98]) of a scalar-valued function in order to construct an rank-1 tensor field. Given a scalar $f : \mathbb{R}^3 \to \mathbb{R}$, the gradient vector flow field is defined as the vector field $\mathbf{v} : \mathbb{R}^3 \to \mathbb{R}^3$ that minimises the energy functional

$$E = \int_{\mathbb{R}^3} \mu\, \Delta\mathbf{v}(\mathbf{r}) + \|\nabla f(\mathbf{r})\|^2 \|\mathbf{v}(\mathbf{r}) - \nabla f(\mathbf{r})\|^2 \, d\mathbf{r} \,. \tag{4.8}$$

Due to the variational formulation, the resulting field gets smooth when there is no data. Otherwise when $\|\nabla f\|$ is large, then v tends to ∇f. The parameter μ is a regularisation parameter and should be set according to the amount of noise presented in the image (see [XP98] for details).

After computing the gradient vector flow we applied the vectorial image filter to the resulting field.

4.5 Tensor Fields of Multi-Channel Data

In this section we will give an approach on how to include multi-channel data into the framework of equivariant image filtering. Figure 4.5 shows a human mitosis cell.

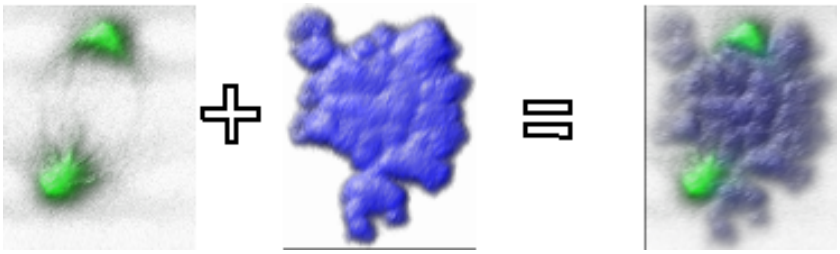

Figure 4.2: Example of a multi-channel image.

By treating each channel as separate scalar-valued function $f_i : \mathbb{R}^3 \to \mathbb{R}$ and $i = 1, \ldots, k$, when $k \in \mathbb{N}$ denotes the number of channels, we can easily integrate this in our framework. It is obvious that we can apply all the previously discussed filters to each channel separately. But even more important is, that we can combine them by using the same products as before.

The only thing we have to do is, extend the non-linear mapping $\mathbf{N}^j[\cdot]$ of the previous sections to multiple input.

We will doing this by exemplary for $k = 2$ channels and give one possible formulation of a non-linear mapping $\mathbf{N}^j$.

Definition 4.5.1. *Let $\mathbf{f}_1, \mathbf{f}_2 \in \mathcal{T}_\ell$ and let $\mathbf{p}_1^0, \ldots, \mathbf{p}_1^n$ and $\mathbf{p}_2^0, \ldots, \mathbf{p}_2^n$ be their expansion in the harmonic basis. We define $\mathbf{N}^j_{Multi}$ as*

$$\mathbf{N}^j_{Multi}\left[\mathbf{p}_1^0, \ldots, \mathbf{p}_1^n, \mathbf{p}_2^0, \ldots, \mathbf{p}_2^n\right] := \sum_{\substack{|j_1 - j_2| \le j \le j_1 + j_2 \\ j_1 + j_2 + j \text{ even} \\ j_1, j_2 \le n}} \alpha^j_{j_1, j_2}\, \mathbf{p}_1^{j_1} \bullet_j \mathbf{p}_2^{j_2} \tag{4.9}$$

where $\alpha^j_{j_1,j_2} \in \mathbb{R}$ are expansion coefficients.

Since we know that each $\mathbf{p}_1^m, \mathbf{p}_2^m \in \mathcal{T}_{m+\ell}$ for $m = 0, \ldots, n$ and knowing the properties of $\bullet_j$ it is obvious that equation (4.9) defines an SE(3)-equivariant mapping in the sense of definition 4.1.3 on page 18. A possible workflow of the filter is depicted in figure 4.3 on page 27.

Algorithm 3 on the following page gives a possible realisation of an SE(3)-equivariant multi-channel (scalar) image filter. The given algorithm also includes information of each channel separately. One could also formulate a multi-channel vectorial image filter in the same way.

Algorithm 3 Multi-Channel Harmonic Filter Algorithm

Input: $f_1, f_2 : \mathbb{R}^3 \rightarrow \mathbb{R}$

Output: $y : \mathbb{R}^3 \rightarrow \mathbb{R}, y := \mathbf{H}\{f_1, f_2\}$

Initialise $\mathbf{y_1}^n := 0 \in \mathcal{T}_n$

Initialise $\mathbf{y_2}^n := 0 \in \mathcal{T}_n$

Initialise $\mathbf{y_3}^n := 0 \in \mathcal{T}_n$

// compute projections onto harmonic basis

Convolve $\mathbf{p_1}^0 := G_\sigma * f_1$

Convolve $\mathbf{p_2}^0 := G_\sigma * f_2$

for $j = 1 : n$ **do**

  $\mathbf{p_1}^j = \boldsymbol{\nabla}^1 \mathbf{p_1}^{j-1}$

  $\mathbf{p_2}^j = \boldsymbol{\nabla}^1 \mathbf{p_2}^{j-1}$

end for

// compute harmonic descriptors

for $j = n : -1 : 1$ **do**

  $\mathbf{y_1}^{j-1} = \boldsymbol{\nabla}_1 \left(\mathbf{y_1}^j + \mathbf{N}^j \left[\mathbf{p_1}^0, \ldots, \mathbf{p_1}^j \right] \right)$ // for f_1 only

  $\mathbf{y_2}^{j-1} = \boldsymbol{\nabla}_1 \left(\mathbf{y_2}^j + \mathbf{N}^j \left[\mathbf{p_2}^0, \ldots, \mathbf{p_2}^j \right] \right)$ // for f_2 only

  $\mathbf{y_3}^{j-1} = \boldsymbol{\nabla}_1 \left(\mathbf{y_3}^j + \mathbf{N}^j_{Multi} \left[\mathbf{p_1}^0, \ldots, \mathbf{p_1}^j, \mathbf{p_2}^0, \ldots, \mathbf{p_2}^j \right] \right)$ // combination of f_1 and f_2

end for

Let $y := \mathbf{y_1}^0 + \mathbf{y_2}^0 + \mathbf{y_3}^0$

// collect the contribution of all voters

Convolve $y := G_\eta * y$

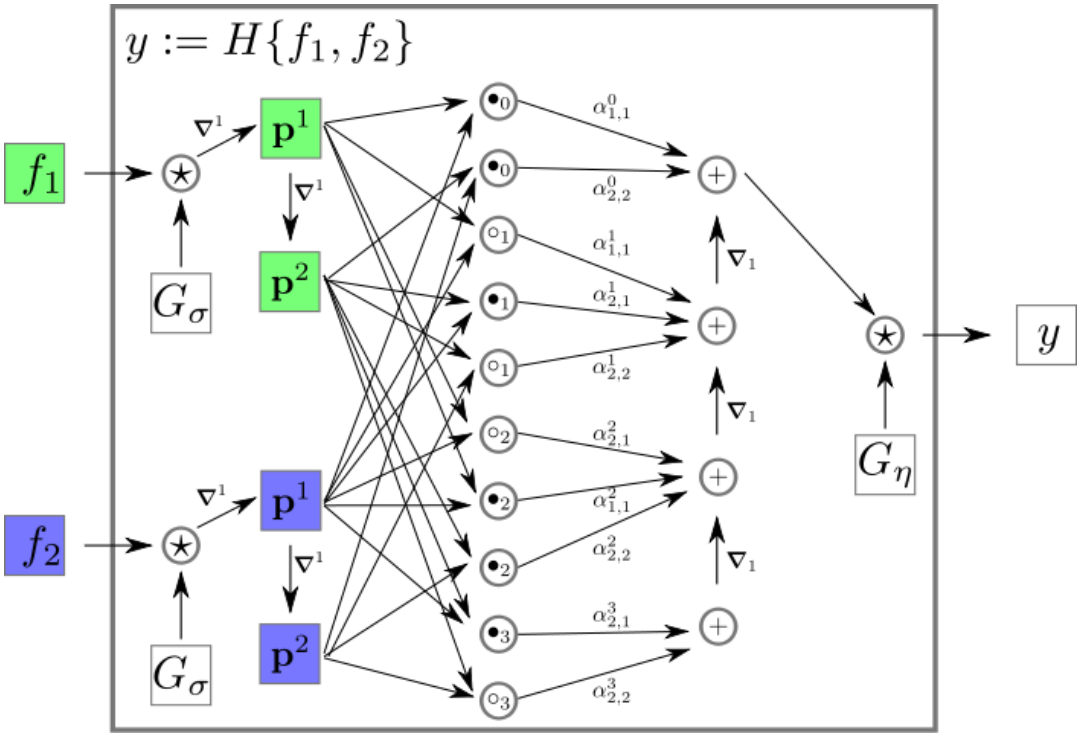

Figure 4.3: Workflow of the harmonic filter for two channels: green and blue.

4.6 Antisymmetric Products and Local Non-linearities

As mentioned in the preliminaries section, for $j = j_1 = j_2 = 1$ and $\mathbf{v} = \mathbf{S}\mathbf{b}$, $\mathbf{w} = \mathbf{S}\mathbf{c} \in V_1$ and $\mathbf{b}$, $\mathbf{c} \in \mathbb{R}^3$ it holds

$$-\mathbf{i}(\mathbf{v} \circ_1 \mathbf{w}) = \frac{1}{\sqrt{2}}\mathbf{S}\,(\mathbf{b} \times \mathbf{c})$$

When we think of $\mathbf{v} = \boldsymbol{\nabla}^1 f(\mathbf{r})$ and $\mathbf{w} = \boldsymbol{\nabla}^1 g(\mathbf{r})$ to be the spherical gradient at position $\mathbf{r}$ of two scalar fields f and g (actually we have $\boldsymbol{\nabla}^1 f(\mathbf{r}) = \mathbf{S}\,\nabla f(\mathbf{r})$ and $\boldsymbol{\nabla}^1 g(\mathbf{r}) = \mathbf{S}\,\nabla g(\mathbf{r})$), $\mathbf{v} \circ_1 \mathbf{w}$ computes the cross products of their gradients at position $\mathbf{r}$. For our image filter, this is only useful when we are in the context of multi-channel images. Otherwise we have (think of the single channel case) that $(\boldsymbol{\nabla}^1\mathbf{f}(\mathbf{r})) \circ_1 (\boldsymbol{\nabla}^1\mathbf{f}(\mathbf{r})) = 0$.

Since the resulting field $(\mathbf{f} \circ_j \mathbf{g}) \in \mathcal{T}_j$ for $\mathbf{f} \in \mathcal{T}_{j_1}, \mathbf{g} \in \mathcal{T}_{j_1}$ and $j + j_1 + j_2 =$ odd, maps onto elements of $\mathbf{i}V_j$, we have to multiply them with $-\mathbf{i}$ in order to get a spherical tensor field that maps onto V_j:

$$-\mathbf{i}\,(\mathbf{f} \circ_j \mathbf{g}) : \mathbb{R}^3 \to V_j$$

Inserting the above in our voting function $\mathbf{N}^j_{Multi}[\cdot]$ we are able to formulate the following extension for multi-channel images:

Definition 4.6.1. *Let* $\mathbf{f}_1, \mathbf{f}_2 \in \mathcal{T}_\ell$ *and let* $\mathbf{p}^0_1, \ldots, \mathbf{p}^n_1$ *and* $\mathbf{p}^0_2, \ldots, \mathbf{p}^n_2$ *be their expansion in the*

harmonic basis. We define $\mathbf{N}^j_{Asym}$ *as*

$$\mathbf{N}^j_{Asym}\left[\mathbf{p}_1^0,\ldots,\mathbf{p}_1^n,\mathbf{p}_2^0,\ldots,\mathbf{p}_2^n\right] := \sum_{\substack{|j_1-j_2|\le j\le j_1+j_2\\ j_1+j_2+j\ even\\ j_1,j_2\le n}} \alpha^j_{j_1,j_2}\ \mathbf{p}_1^{j_1}\bullet_j \mathbf{p}_2^{j_2} - \sum_{\substack{|j_1-j_2|\le j\le j_1+j_2\\ j_1+j_2+j\ odd\\ j_1,j_2\le n}} \alpha^j_{j_1,j_2}\ \mathbf{i}\,(\mathbf{p}_1^{j_1}\circ_j \mathbf{p}_2^{j_2})$$

where $\alpha^j_{j_1,j_2}\in\mathbb{R}$ *are expansion coefficients.*

In algorithm 4 we give a possible realisation of a multi-channel scalar image filter. But many other realisations are possible. One could include information of the single channel separately as we did it in algorithm 3 on page 26 or extend the algorithm to higher order input or both.

Algorithm 4 Multi-Channel Harmonic Filter Algorithm with Antisymmetric Products

Input: $f_1, f_2 : \mathbb{R}^3 \to \mathbb{R}$, $i = 1, 2$
Output: $y : \mathbb{R}^3 \to \mathbb{R}$, $y := \mathbf{H}\{f_1, f_2\}$

1: Initialise $\mathbf{y}^n := 0 \in \mathcal{T}_0$
// compute projections onto harmonic basis
2: Convolve $\mathbf{p_1}^0 := G_\sigma * f_1$
3: Convolve $\mathbf{p_2}^0 := G_\sigma * f_2$
4: **for** $j = 1 : n$ **do**
5: $\quad \mathbf{p_1}^j = \boldsymbol{\nabla}^1 \mathbf{p_1}^{j-1}$
6: $\quad \mathbf{p_2}^j = \boldsymbol{\nabla}^1 \mathbf{p_2}^{j-1}$
7: **end for**
// compute harmonic descriptors
8: **for** $j = n : -1 : 1$ **do**
9: $\quad \mathbf{y}^{j-1} = \boldsymbol{\nabla}_1\left(\mathbf{y}^j + \mathbf{N}^j_{Asym}\left[\mathbf{p_1}^0,\ldots,\mathbf{p_1}^j,\mathbf{p_2}^0,\ldots,\mathbf{p_2}^j\right]\right)$
10: **end for**
11: Let $y := \mathbf{y}^0 + \mathbf{N}^0_{Asym}\left[\mathbf{p_1}^0,\ldots,\mathbf{p_1}^j,\mathbf{p_2}^0,\ldots,\mathbf{p_2}^j\right]$
// collect the contribution of all voters
12: Convolve $y := G_\eta * y$

5 Steerable Filter

This section introduces the concept of steerable filters ([FY91], [JU04] and [AJU05]) in a context of an orientation dependent feature detection task in 3D. In the sense of a matched filter (figure 5.1) this means, that we filter our input signal $f(\mathbf{x})$ with our template $h(\mathbf{x})$ and get the filter response as $r(\mathbf{x}) = f(\mathbf{x}) * h(\mathbf{x})$ (by convolution). Measuring the similarity of $f(\mathbf{x})$ and the shifted template $g(\mathbf{x}) = h(\mathbf{x} - \tau)$ by the inner product $\langle f \mid g \rangle$, each voxel position in the filtered signal $r(\mathbf{x})$ reflects the similarity of the input signal and the template at that position.

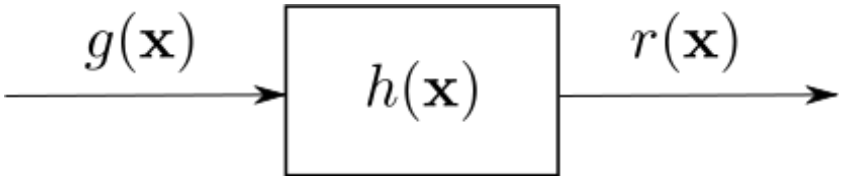

Figure 5.1: Matched filter.

Since we are interested in detecting arbitrary rotated versions of our template, we can state the following optimisation task:

$$(\theta(\mathbf{x})^*, \phi(\mathbf{x})^*) = \arg\max_{\theta,\phi}(f(\mathbf{x}) * h(\mathbf{R}_{\theta,\phi}\mathbf{x})) \tag{5.1}$$

where $h(\mathbf{R}_{\theta,\phi}\mathbf{x})$ is the feature template rotated by Euler angels θ and ϕ.

The magnitude of the filter r^* with respect to the optimal orientation of the appropriate feature template is given by

$$r^*(\mathbf{x}) = f(\mathbf{x}) * h(\mathbf{R}_{\theta^*,\phi^*}\mathbf{x}) \tag{5.2}$$

A direct implementation of the postulated problem (5.2) is computationally very expensive and cannot be applied to real world scenarios. Accordingly, we will follow the steerable formulation introduced in [FY91]. Therefore we need to define a family of separable basis filters, which can be used to build any rotated version of the filter by taking a linear combination of the basis filters (for an introductory example in 2D see [FY91]).

5.1 M-th Order Basis Filter Bank

By taking the linear combination of a small number of basis filters, we can reduce the computational costs by filtering our input signal only with the basis filter bank.

For the creation of our feature template we use the linear combination of M-th order partial derivatives of an isotropic 3D Gaussian function $g(\mathbf{x})$ (we assume standard deviation $\sigma = 1$ and mean $\mu = 0$ for convenience) according to [AJU05]:

$$h(\mathbf{x}) = \sum_{k=1}^{M} \sum_{i=0}^{k} \sum_{j=0}^{k-i} \alpha_{k,i,j} \underbrace{\frac{\partial^i}{\partial x_1^i} \frac{\partial^j}{\partial x_2^j} \frac{\partial^{k-i-j}}{\partial x_3^{k-i-j}} g(\mathbf{x})}_{h_{k,i,j}(\mathbf{x})} \quad , \ \alpha_{k,i,j} \in \mathbb{R} \tag{5.3}$$

$$= \sum_{k=1}^{M} \sum_{i=0}^{k} \sum_{j=0}^{k-i} \alpha_{k,i,j} \, h_{k,i,j}(\mathbf{x}) \tag{5.4}$$

$\frac{\partial^i}{\partial x_1^i}$ denotes the i-th partial derivative along the coordinate x_1, writing our coordinate vector as $\mathbf{x} = (x_1, x_2 x_3)^T$. The functions $h_{k,i,j}(\mathbf{x})$ build up the basis filter bank.
Now we can formulate the convolution of the input volume $f(\mathbf{x})$ with a rotated version of the steerable filter as

$$f(\mathbf{x}) * h(\mathbf{R}_{\theta,\phi}\mathbf{x}) = \sum_{k=1}^{M} \sum_{i=0}^{k} \sum_{j=0}^{k-i} \beta_{k,i,j}(\theta, \phi) \; f * h_{k,i,j}(\mathbf{x}) \tag{5.5}$$

where the orientation dependent weights $\beta_{k,i,j}(\theta, \phi)$ are polynomials in $(\cos\theta \sin\phi)$, $(\sin\theta \sin\phi)$ and $\cos\phi$ (see [JU04] and [FY91]).
It is obvious considering equation (5.5), that we only have to know the filter response of our basis filters to compute the filter response of $h(\mathbf{R}_{\theta,\phi}\mathbf{x})$. The principal work flow of the steerable filter algorithm is depicted in figure 5.2. Details on this will be given in section 5.3 on the next page.

But first, we need to do some considerations on how to design an optimal template for our specific mitosis detection task.

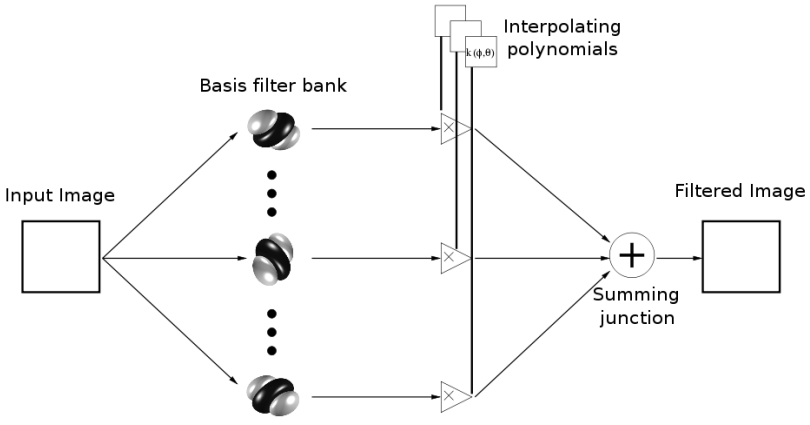

Figure 5.2: Illustration of the steerable filter algorithm.

5.2 Design of the Template

The authors in [AJU05] derive optimal surface and curve detector oriented along the x_1 axis by minimising the localisation error which yields to the following representation:

$$h(\mathbf{x}) = \underbrace{\left(\frac{\partial^2}{\partial x_1^2}g + \frac{\partial^2}{\partial x_2^2}g + \frac{\partial^2}{\partial x_3^2}g\right)}_{\triangle g} - (\alpha + 1)\frac{\partial^2}{\partial x_1^2}g \tag{5.6}$$

$\triangle g$ denotes the isotropic 3D laplacian of g, which is invariant to rotations. The parameter $\alpha \in \mathbb{R}$ is for the surface detector $\alpha = 4$ and for the curve detector $\alpha = \frac{2}{3}$ (see [AJU05] for details). Since we do not have templates than can be given in an analytical way, like a line or a surface as used by [AJU05], we defined the detector empirically. The detector we used is depicted in figure 5.3 and is given by setting $\alpha = 3$ in equation (5.6). We chose the parameters to best fit the spindle centres of mitosis cells.

The question arises why not to use an SVD approach for steerable filters as described in [SMH98]. The answer is the harmonic filter (see chapter 4) which is in fact a more general approach than the one described in [SMH98].

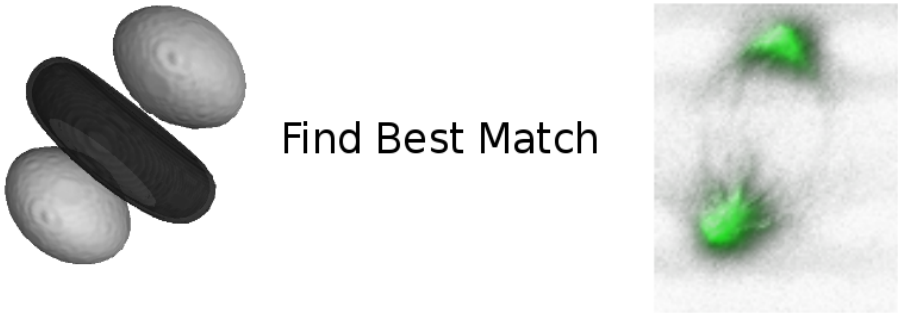

Figure 5.3: Idea of 3D steerable filter.

5.3 Steering and Implementation

We can rotate our feature $h(\mathbf{x})$ to an arbitrary orientation specified by $\mathbf{v} = (\cos\theta\sin\phi, \sin\theta\sin\phi, \cos\phi)^T$

$$h(\mathbf{R}_{\theta,\phi}\mathbf{x}) = \left(\frac{\partial^2}{\partial x_1^2}g + \frac{\partial^2}{\partial x_2^2}g + \frac{\partial^2}{\partial x_3^2}g\right) - (\alpha + 1)\,\mathbf{v}^T\mathbf{H}_g\mathbf{v} \tag{5.7}$$

$\mathbf{H}_g$ denotes the 3D Hessian matrix of $g(\mathbf{x})$. We can rewrite the expression as

$$h(\mathbf{R}_{\theta,\phi}\mathbf{x}) = \mathbf{v}^T\mathbf{A}_g\mathbf{v} \tag{5.8}$$

where

$$\mathbf{A}_g = \left(\frac{\partial^2}{\partial x_1^2}g + \frac{\partial^2}{\partial x_2^2}g + \frac{\partial^2}{\partial x_3^2}g\right)\mathbf{I} - (\alpha + 1)\mathbf{H}_g$$

and $\mathbf{I}$ denotes the identity matrix. Using the linearity of the convolution, we can write the convolution with our rotated feature template as

$$f(\mathbf{x}) * h(\mathbf{R}_{\theta,\phi}\mathbf{x}) = \mathbf{v}^T \mathbf{A}_{f*g} \mathbf{v} \tag{5.9}$$

Finally steering of our feature template is done via Eigenvalue Decomposition. The solution of the optimal filter response and orientation respectively is given by

$$r^* = \lambda_{max} \tag{5.10}$$

$$\mathbf{v}^* = \mathbf{e}_{max} \tag{5.11}$$

λ_{max} denotes the maximum eigenvalue of $\mathbf{A}_{f*g}$ and $\mathbf{e}_{max}$ the corresponding eigenvector.

For the implementation one only has to evaluate the 3×3 matrix $\mathbf{A}_{f*g}$ for each position in the input volume. Therefore, we first compute the convolution with our basis filter bank

$$\frac{\partial^2}{\partial x_1^2} g, \ \frac{\partial^2}{\partial x_2^2} g, \ \frac{\partial^2}{\partial x_3^2} g, \ \frac{\partial^2}{\partial x_1 \partial x_2} g, \ \frac{\partial^2}{\partial x_1 \partial x_3} g, \ \frac{\partial^2}{\partial x_2 \partial x_3} g$$

and afterwards we get the optimal response and orientation by computing the Eigenvalue Decomposition of $\mathbf{A}_{f*g}$.

6 Feature Computation

In this chapter we present our features which we have used for classification and validation of mitosis cells. We utilise the mathematical theory of spherical harmonics (see chapter 3.3 on page 13) to represent functions defined on a sphere in a rotation invariant manner. When we speak of functions defined on a sphere we mean $F : S^2 \to \mathbb{R}$ in a most common sense. More practical, representing a whole data set by this definition means we define our function sampled on the scaled 2-sphere

$$F : r\,S^2 \to \mathbb{R}$$

where $r \in \mathbb{R}$ and $r\,S^2 := \{\mathbf{x} \in \mathbb{R}^3 | \; \exists\, \mathbf{s} \in S^2 : \mathbf{x} = r\,\mathbf{s}\}$. We denote the radius r of the sphere as subscript F_r, when we want to distinguish functions sampled at different shell radii (see figure 6.1 on the next page).

6.1 Spherical Harmonic Descriptor

Orthogonal projection of a spherical function $F(\theta, \phi)$ into the sum of its harmonics:

$$F(\theta, \phi) = \sum_{l=0}^{\infty} \sum_{m=-l}^{l} a_m^l \cdot Y_m^l(\theta, \phi) \tag{6.1}$$

where a_m^l compute as

$$a_m^l = \langle F \,|\, Y_m^l \rangle = \int_{S^2} F(s)\, \overline{Y_m^l(s)}\, ds \tag{6.2}$$

where ds denotes the standard measure on S^2.
Let $g \in \mathsf{SO}(3)$ an element of the rotation group. g acts on functions defined on the 2-sphere F by

$$(gF)(\mathbf{s}) := F(\mathbf{R}^T\mathbf{s})$$

where $\mathbf{R} \in \mathbb{R}^{3\times3}$ is the corresponding rotation matrix to g. The expansion coefficients a_m^l of F in equation (6.2) have the following transformation property

$$\sum_{m'=-l}^{m'=l} D_{mm'}^l(g)\; a_{m'}^l = \langle Y_m^l \,|\, gF \rangle,$$

or shortly

$$\mathbf{D}_g^l \mathbf{a}^l = \langle \mathbf{Y}^l \,|\, gF \rangle. \tag{6.3}$$

The $\mathbf{D}_g^l$ are unitary transformation matrices depending on the rotation g and are known as *Wigner D-matrices* (see section 3.1 on page 10). This property allows us to obtain invariance

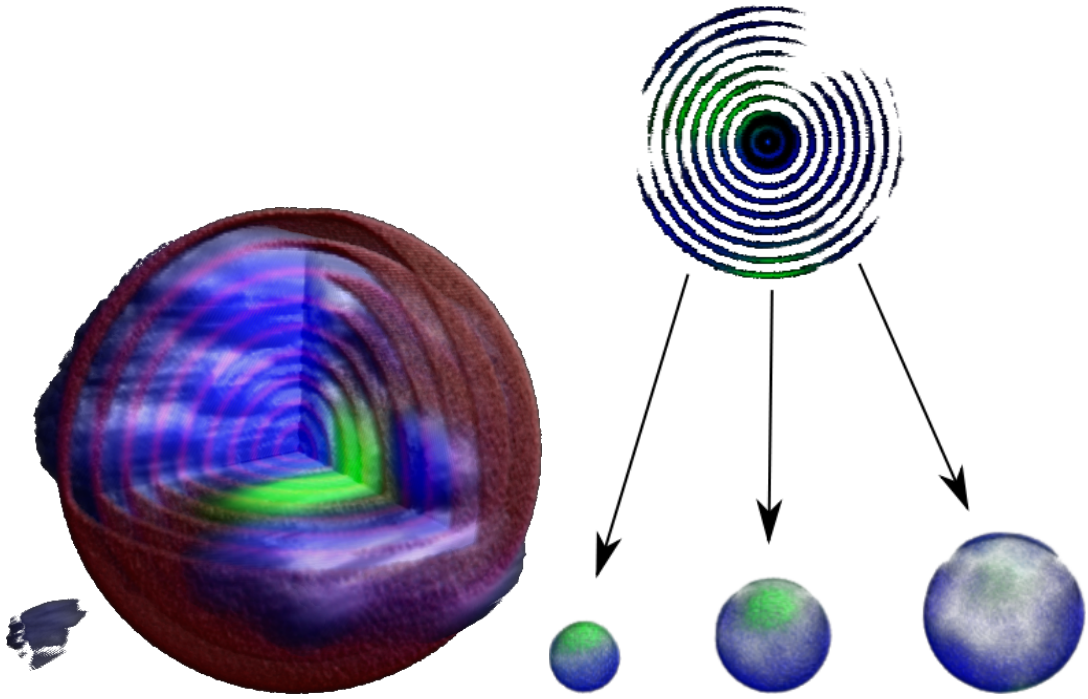

Figure 6.1: Functions F_r defined on the scaled 2-sphere $r\,S^2$

against rotations.
Due to the unitarity of $\mathbf{D}_g^l$ the energy within a subspace l is preserved. One can easily obtain invariant features of the function F by taking the band-wise energy

$$\|\mathbf{D}_g^l\,\mathbf{a}^l\| = \sqrt{\langle \mathbf{D}_g^l\,\mathbf{a}^l \,|\, \mathbf{D}_g^l\,\mathbf{a}^l\rangle} = \sqrt{\langle \mathbf{a}^l \,|\, \mathbf{a}^l\rangle} = \sqrt{\sum_{m=-l}^{m=l} |a_m^l|^2} = \|\mathbf{a}^l\|$$

Doing this for all $l = 0, \ldots, N$ where $N \in \mathbb{N}$ is the index by which we truncate the series in equation (6.1) and defining

$$\mathrm{SHD}(F, N) = \{\, \|\mathbf{a}^0\|, \ldots, \|\mathbf{a}^N\| \,\}\,, \tag{6.4}$$

we get an rotation invariant description of F defined on a sphere. The descriptor given by (6.4) is called SH-descriptor (see [KFR03]). For each radius $r_i \in \mathbb{R}$, $i = 1, \ldots, M$ on which we sample our data we can define the descriptor $\mathrm{SHD}(F_{r_i}, N)$ (see figure 6.2 on the next page) and get our final feature vector by appending the feature vectors of different radii.

We also gain invariance to rotations by calculating the inner product of expansion coefficients of corresponding subspaces defined by different radii. Let r_i and r_j be radii of different shells and F_{r_i} and F_{r_j} the corresponding functions defined on $r_i\,S^2$ and $r_j\,S^2$ respectively. Let $\mathbf{a}^l$ be the expansion coefficients (of a fixed subspace l) of F_{r_i} and $\mathbf{b}^l$ of F_{r_j} respectively. Then we

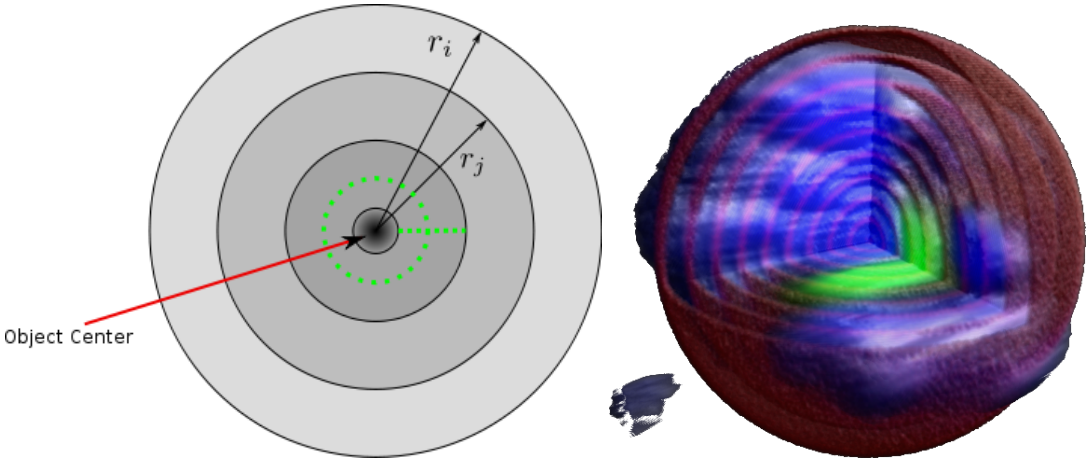

Figure 6.2: Shell model.

gain rotation invariance due to the unitarity of $\mathbf{D}_g^l$

$$\langle \mathbf{D}_g^l \mathbf{a}^l \,|\, \mathbf{D}_g^l \mathbf{b}^l \rangle = \langle \mathbf{a}^\mathbf{l} \,|\, \mathbf{b}^l \rangle = \mathbf{a}^{\mathbf{l}^T} \mathbf{b}^l = \sum_{m=-l}^{m=l} \overline{a_m^l} b_m^l \tag{6.5}$$

We can do this for different radii combinations and append the result to our feature vector. Note that we have to assume that the shells have a fixed orientation to each other, meaning all spheres are rotated by the same element $g \in \mathrm{SO}(3)$.

6.2 Extending the Descriptor to Multi-Channel Data

Now we want to do some considerations on how we can extend the descriptor defined in section 6.1 on page 33 to multi-channel data. By treating each channel independently it is obvious that we compute a descriptor as described in section 6.1 on page 33 for each channel. By appending the resulting descriptors of each channel to one large feature vector, we get an invariant descriptor which, however, does not respect the interconnection of channels.
The simplest way to include information about interconnection of multiple channels would be to follow the same approach as for connecting functions on different spheres, namely by inner product. We can assume that all channels have a rigid interconnection, because they represent the same object. By rotating the object itself, we rotate each channel by the same element $g \in \mathrm{SO}(3)$. Therefore equation (6.5) holds for spherical functions defined by different channels. So we get a rotation invariant description of the interconnection of two channels by computing the inner product of their expansion coefficients.

Algorithm 5 SH-Descriptor for Multiple Channels

Input: $X_i : \mathbb{R}^3 \to \mathbb{R}$, $i = 1, \ldots, N$ list of channels
Input: $r_i \in \mathbb{R}$, $i = 1, \ldots, M$ list of radii
Input: $(r_i, r_j) \in \mathbb{R}^2$, $1 \leq r_i, r_j \leq M$ list of radii tuples
Input: $(i, j) \in \mathbb{N}^2$, $1 \leq i, j \leq N$ list of channel index tuples
Output: Invariants

```
    // compute SH-Descriptor for each channel
 1: for i = 1, ..., N do
 2:     for all r ∈ radii do
 3:         Inv := band-wise energy for radius r in source X_i
 4:         append Inv to list of invariants
 5:     end for
 6:     for all (r_1, r_2) ∈ radii tuples do
 7:         Inv := inner product of radii r_1 and r_2 in source X_i
 8:         append Inv to list of invariants
 9:     end for
10: end for
    // compute interconnection invariants of channels
11: for all (i, j) ∈ index tuples do
12:     for all r ∈ radii do
13:         Inv := band-wise inner product for radius r in sources X_i and X_j
14:         append Inv to list of invariants
15:     end for
16:     for all (r_1, r_2) ∈ radii tuples do
17:         Inv := band-wise inner product of radius r_1 in source X_i and radius r_2 in source X_j
18:         append Inv to list of invariants
19:     end for
20: end for
```

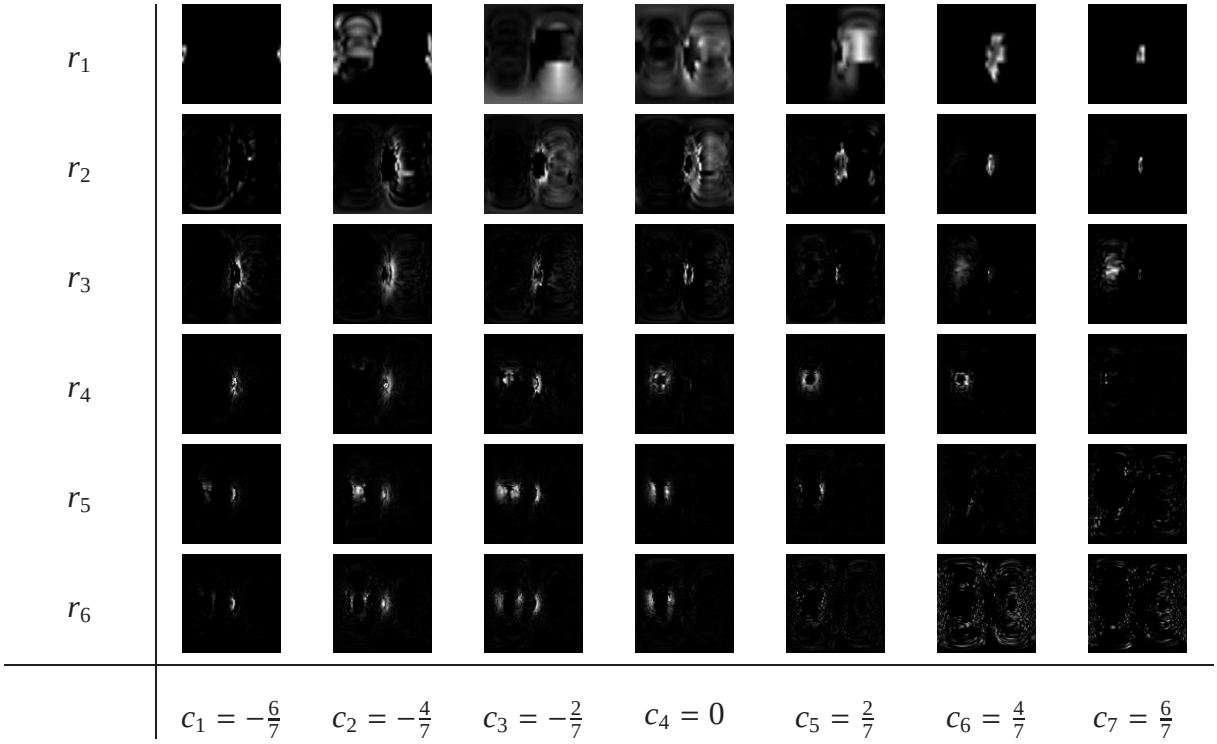

Figure 6.3: FITC channel profile image. c_i are gradient direction quantisation values. r_i is the radius of the sphere on which the signal was sensed. The index i is the radius of the sphere in μm.

6.3 Simplified MiSP Invariants for Multi-Channel Data

We will introduce a simplified version of the MiSP invariants used in [Ron07]. The main goal in [Ron07] was to integrate a global deformation model into the Haar-Integration framework (see [SM95] and [RFB05]). Therefore, the original dense 3D space was split up into gradient direction and gradient magnitude for the construction of robust invariants (see also [SSR+06]) and projected onto a 4D sparse space that was spanned by the parameters: $\|\mathbf{d}\|$ = distance to segmentation surface, c = radial component of the normalised gradient, and the sensed signal as function of a deformed sphere (shell with distance $\|\mathbf{d}\|$ to segmentation surface) parametrised by latitude θ and colatitude ϕ.

Since we do not have any information about the contour of our objects, we can not model deformations as done in [Ron07]. However, when we assume fixed concentric shells around the object centre, as depicted in 6.2, we can project the original dense space onto the sparse 4D space by replacing the distance $\|\mathbf{d}\|$ to the segmentation surface by the distance to the object centre. The resulting sparse 4D space is shown in figure 6.3 and 6.4.

The extension to multi-channel data is straightforward, we simply combine the 4D space of all channels into one multi-channel image (see figure 6.5).

Since we are interested in being invariant to rotations of our objects, we follow the same approach as used in section 6.2.

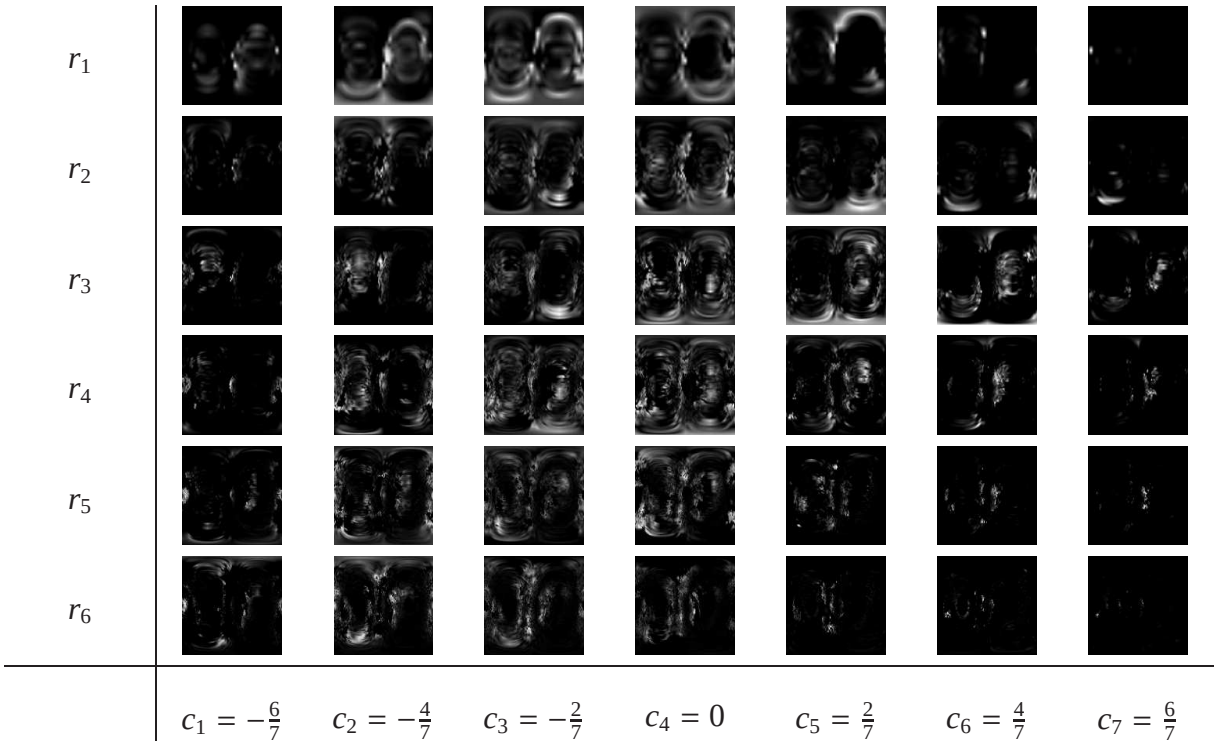

Figure 6.4: DAPI channel profile image. c_i are gradient direction quantisation values. r_i is the radius of the sphere on which the signal was sensed. The index i is the radius of the sphere in μm.

Algorithm 6 MiSP Invariants (for 1 Image)

Input: $X : \mathbb{R}^3 \to \mathbb{R}$
Output: Invariants := MiSP(X) list of invariants
Input: $r_i \in \mathbb{R}$, $i = 1, \ldots, M$ list of radii
Input: $(r_i, r_j) \in \mathbb{R}^2$, $1 \leq r_i, r_j \leq M$ list of radii tuples
Input: $(i, j) \in \mathbb{N}^2$, $1 \leq i, j \leq N$ list of
Input: gradDir, list of gradient direction quantisation
Output: Invariants

// compute 4D profile
Initialise profile := $0 \in \mathbb{R}^4$ // dimensions are distance to centre (”shell”), radial component of gradient direction (”gradDir”), θ and ϕ
Initialise weights := $0 \in \mathbb{R}^4$ // dimensions as profile
D := array 3D containing radial distance to object centre
G := radial component of gradient direction
M := gradient magnitude of
for all $(\theta,\ \phi)$ **do**
  for all x on a beam in $(\theta,\ \phi)$ direction **do**
    profile$(D(\mathbf{x}), G(\mathbf{x}), \theta, \phi) +=\ M(\mathbf{x})$ // array access uses tri-linear interpolation
    weights$(D(\mathbf{x}), G(\mathbf{x}), \theta, \phi) +=\ 1$
  end for
end for
profile / = weights
// compute spherical harmonic transform
profileSH := $0 \in \mathbb{R}^4$ // dimensions are shell, gradDir and Spherical Harmonics parameters l and m
for all r_i in profile **do**
  for all gradDir in profile **do**
    profileSH(shell, gradDir) := SH-Transform(profile(shell, gradDir))
  end for
end for
// compute invariants
for all r_i and gradDir **do**
  Compute band-wise energy
  Append energy to Invariants
end for
for all (r_i, r_j) and gradDir **do**
  Compute band-wise inner product of different shells
  Append energy to Invariants
end for

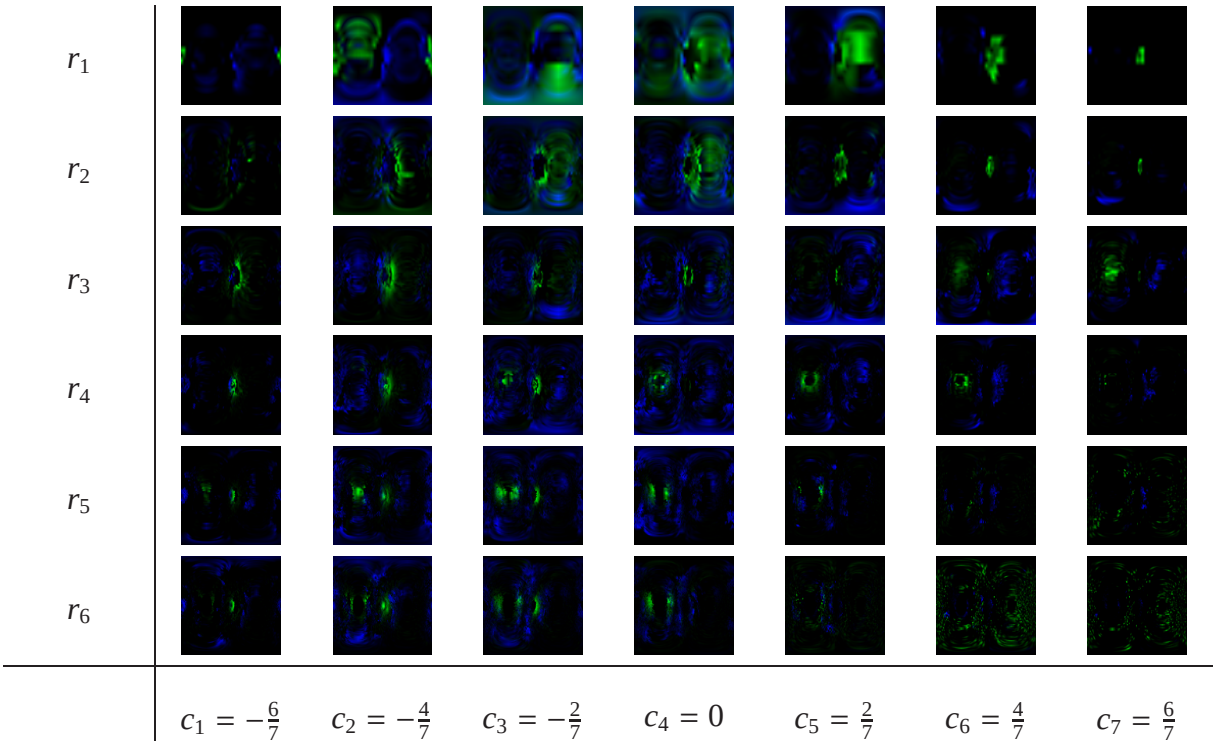

Figure 6.5: Multi-channel profile image. c_i are gradient direction quantisation values. r_i is the radius of the sphere on which the signal was sensed. The index i is the radius of the sphere in μm.

7 Experiments

7.1 Description of Data

The imaging of the cell line data was done with Zeiss ApoTome. The ApoTome uses the principle of structured illumination (see [SSS04] and [BS06] for details) to improve resolution in the axial dimension.

Though, structured illumination techniques allow imaging thick tissue samples, it also leads to artifacts in the reconstructed images due to bleaching effects of the tissue. Figure 7.1 shows an example of a ApoTome recorded stack slice. One can clearly see the wave artifacts stemming from the projected grid.

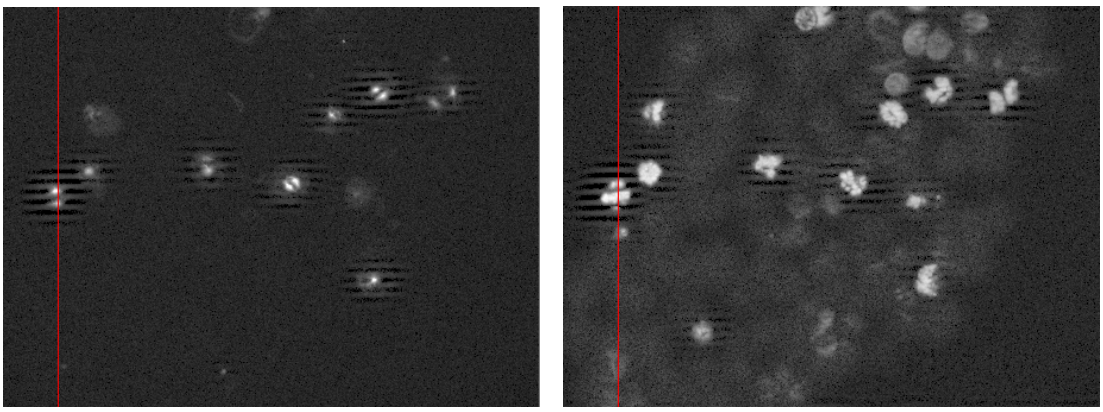

(a) Channel0 XY-slice (b) Channel1 XY-slice

Figure 7.1: XY-slice of a stack recorded with the ApoTome showing the wave artifacts which arise from structured illumination techniques. The presented images are highly gamma corrected

Note that we will refer to the centrosome channel (FITC) as channel-0, whereas for the cell membrane (DAPI) channel as channel-1.

7.2 Segmentation

For segmentation of cell we did experiments with a standard watershed segmentation algorithm. Since the cells showed many disconnected regions (see 7.2) we applied in a previous step a fill-hole algorithm. The segmentation results are depicted in 7.3. One can clearly see that the result is highly over segmented. Therefore we neglected to use the segmentation results for our experiments.

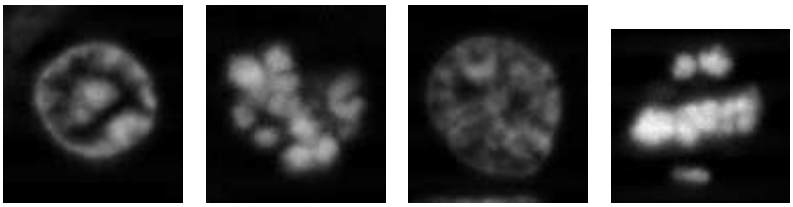

(a) Channel1 XY-slice (b) Channel1 XY-slice (c) Channel1 XY-slice (d) Channel1 XY-slice

Figure 7.2: Images with disconnected regions: ”holes” and ”gaps”.

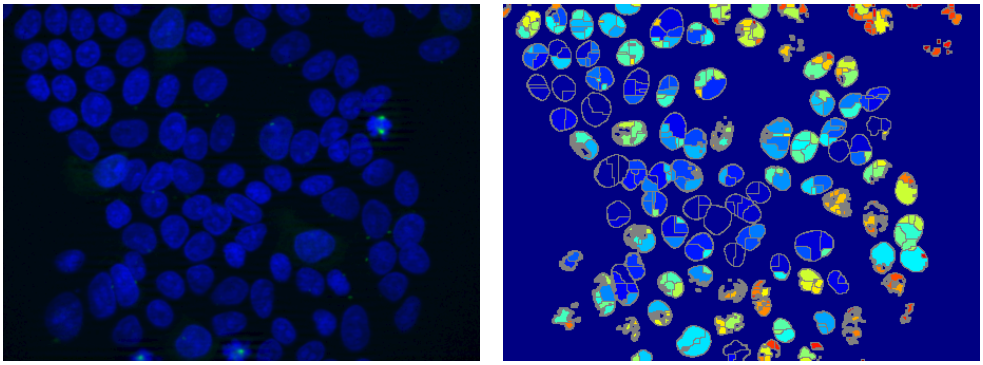

(a) Raw data XY-slice (b) Region labels XY-slice

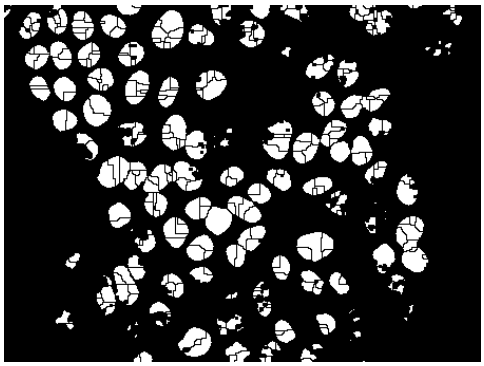

(c) Segmentation mask XY-slice

Figure 7.3: Result of the watershed segmentation algorithm.

7.3 Detection of Mitosis Cells

In this section we will present the results of steerable filter, harmonic filter and multi-channel harmonic filter algorithms which we described in chapter 4 and 5.
For the steerable filter, we could only use channel-0, because it is very difficult to design a template that would match the various shapes of the cells at hand (see appendix D for the whole cell database). We used a normalised version ”SF(Norm)” and a version without normalisation ”SF(c0)”. The normalisation was done by mapping the values of the input data on the interval $[0, 1]$. Furthermore, and in analogy to the collection of local voters as for the harmonic filter, we applied an output smoothing to the filter response to make regions of high local evidence smooth. We refer to them as ”SFS(c0)” and ”SFS(Norm)” respectively. Note that also for the steerable filter we have a kind of local non-linearity, namely by taking highest eigenvalue of the eigenvalue decomposition.
For the harmonic filter and for the multi-channel harmonic filters, we used a normalised version and a version without normalisation. We refer to them as ”HF(c0)” and ”HF(c0,Norm)” for the single channel version applied to channel-0 and as ”HFM” and ”HFM(Norm)” respectively. The harmonic filter using antisymmetric is denoted as ”HFMasym” and ”HFMasym(Norm)” for the normalised version. The normalisation was done as proposed in section 4.2 on page 19 by equation (4.7), by a normalisation of the first-order descriptor image on the standard deviation of local window.
The vectorial harmonic filter is denoted as ”HFM(GVF)” according to the gradient vector flow fields of channel-0 and channel-1 which were used as filter input. For the normalisation we set all vectors to unity length, which means that we only had directional information of the flow field.

Before we go into further details we will represent an overview of the filters described above. Table 7.1 on page 45 gives an overview results of the mitosis detection results achieved by the various filters. Figure 7.3 on the following page gives an overview of the complete precision-recall graphs of the various filters. All results were calculated by counting a detection as positive if it was in a precision radius of $3\mu m$ around the given label position in order to assure that we are inside the cell (average cell diameter was $9\mu m$). The best results were achieved with ”HFMasym”, the multi-channel harmonic filter with symmetric and antisymmetric products. A detailed description of all the results can be found in appendix B.

We already discussed the normalisation we chose for our filters. In case of the harmonic filter and the smoothed steerable filter we have to choose the size η of the Gaussian window. For η we chose half of the average cell diameter, which was found to be $4.5\mu m$. For the harmonic filters we also had to choose the size of the local features σ. We achieved our best results with $\sigma = 1.5\mu m$. For the expansion degree we used $n = 4$. The influence of the different expansion degrees is depicted in 7.5(b) on page 45. If the expansion degree is to low the precision and recall values are getting worse. This is also the case if we choose the expansion degree to high. The filter looses its generalisation ability. A good choice for the parameter γ was found to be 0.1. We mapped all input data values for the scalar filter to the range $[0, 1]$ as we did for the normalised steerable filter.

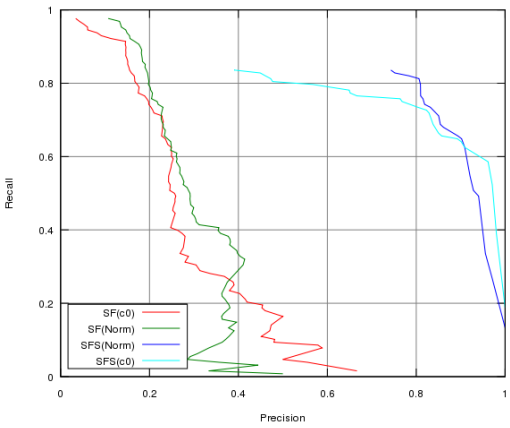

(a) Steerable filter overview

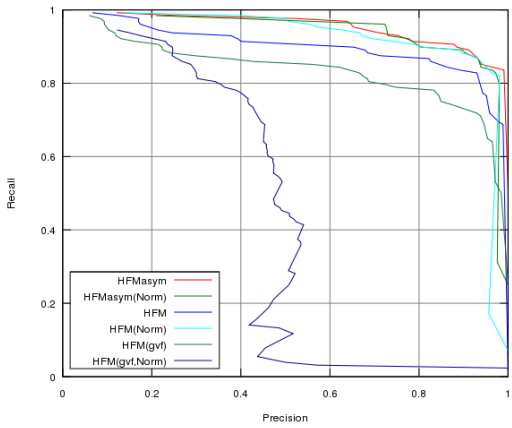

(b) Multi-channel harmonic filter overview

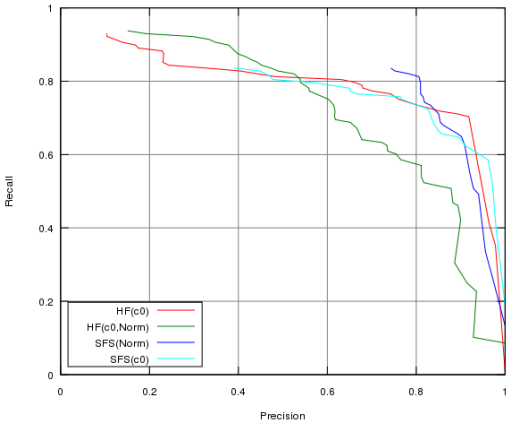

(c) Harmonic filter vs steerable filter on channel0

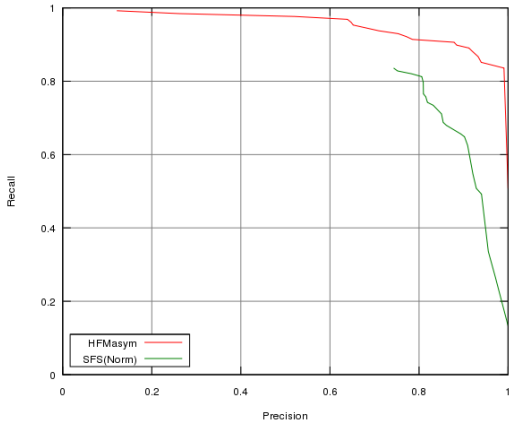

(d) Multi-channel harmonic filter vs steerable filter

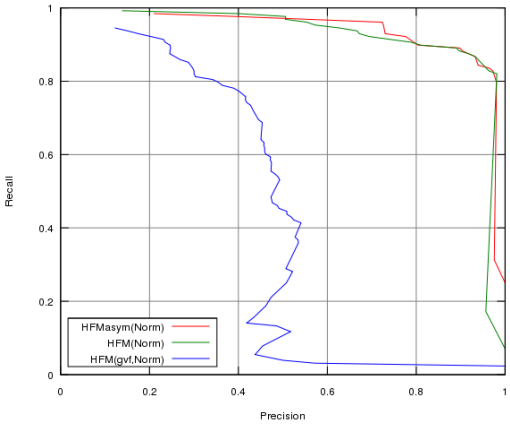

(e) Multi-channel harmonic filter overview (normalised)

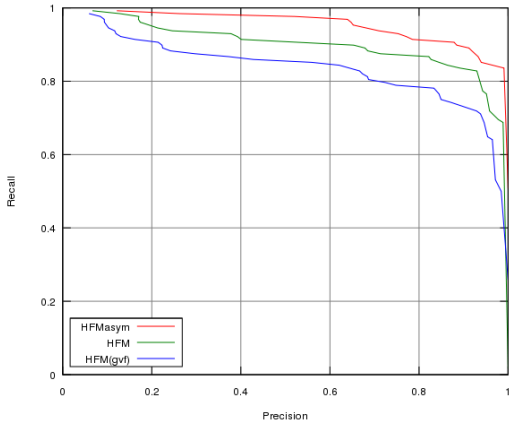

(f) Multi-channel harmonic filter overview (no normalisation)

Figure 7.4: Precision-Recall overview of the different filter algorithms.

Table 7.1: Detection results (recall) in % for fixed precision values.

Filter	50% Precision	70% Precision	90% Precision
SF(c0)	9%	5%<	5%<
SF(Norm)	5%<	5%<	5%<
SFS(c0)	80%	76%	64%
SFS(Norm)	83%	83%	65%
HF(c0)	82%	77%	42%
HF(c0,Norm)	83%	64%	71%
HFM	91%	88%	83%
HFM(Norm)	**98%**	92%	87%
HFM(GVF)	86%	80%	73%
HFM(GVF,Norm)	45%	5%<	5%<
HFMasym	**98%**	94%	**89%**
HFMasym(Norm)	97%	**96%**	88%

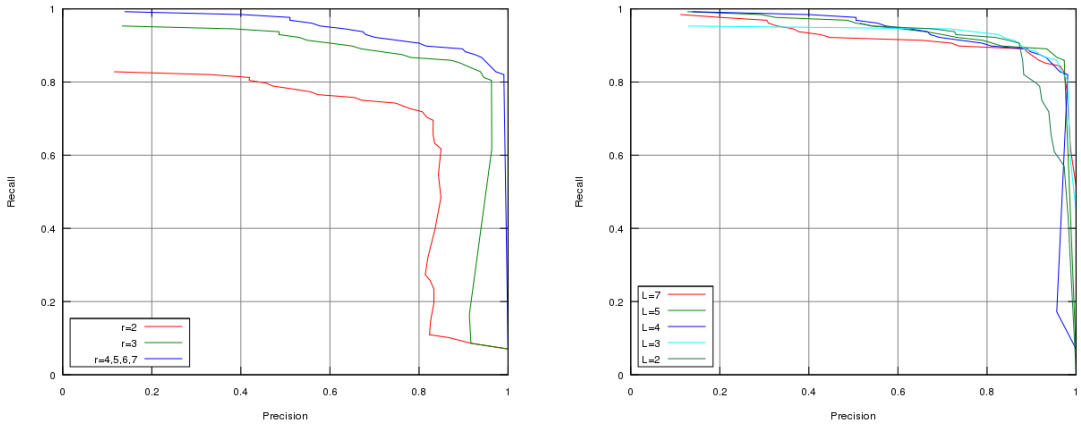

(a) Different precision radii. (b) Different expansion values L.

Figure 7.5: Precision-Recall for different filter parameters of ”HFM(Norm)”

The data set with the most false detections is depicted in figure 7.6 on the following page. The data set shows one huge aberrant cell for which we gave no labels. It was the only appearance of such a cell.
All filters had problems when the cells in the input data were larger than the diameter of our voting function, which was especially the case for cells in the control group. Figure 7.7 on page 47 shows an example of a cell that was too large. The cell was detected as two separate cells, but with low filter response in case of the harmonic filters.

Figure 7.8 on page 48 shows an example where all filters had good results. But one can also see the that the harmonic filters have much better localisation precisions of the ”true” cell centre than the steerable filter.

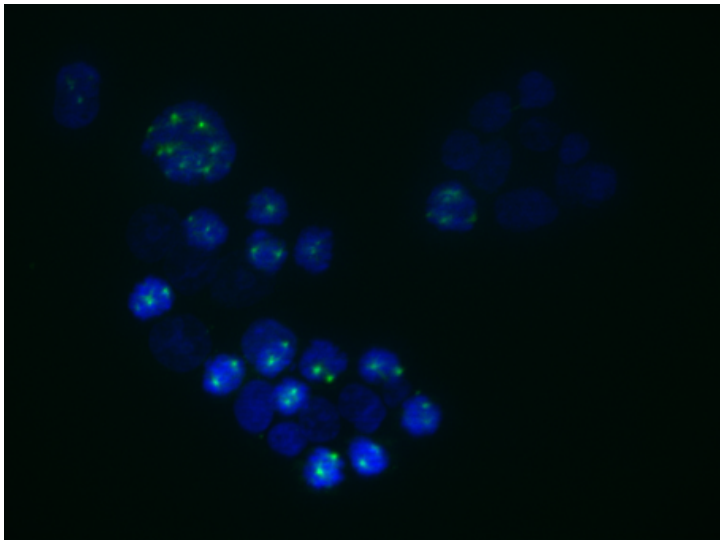

Figure 7.6: HT29 (STK15,4) data set with a huge aberrant cell.

Figure 7.9 on page 49 shows a false positive detection of the harmonic filters. It is conspicuous that the normalised filter HFM(Norm) has the highest response and it is likely due to the fact that we have very small standard deviation in channel-0. One should set a higher γ value in the normalisation to avoid such false detections.

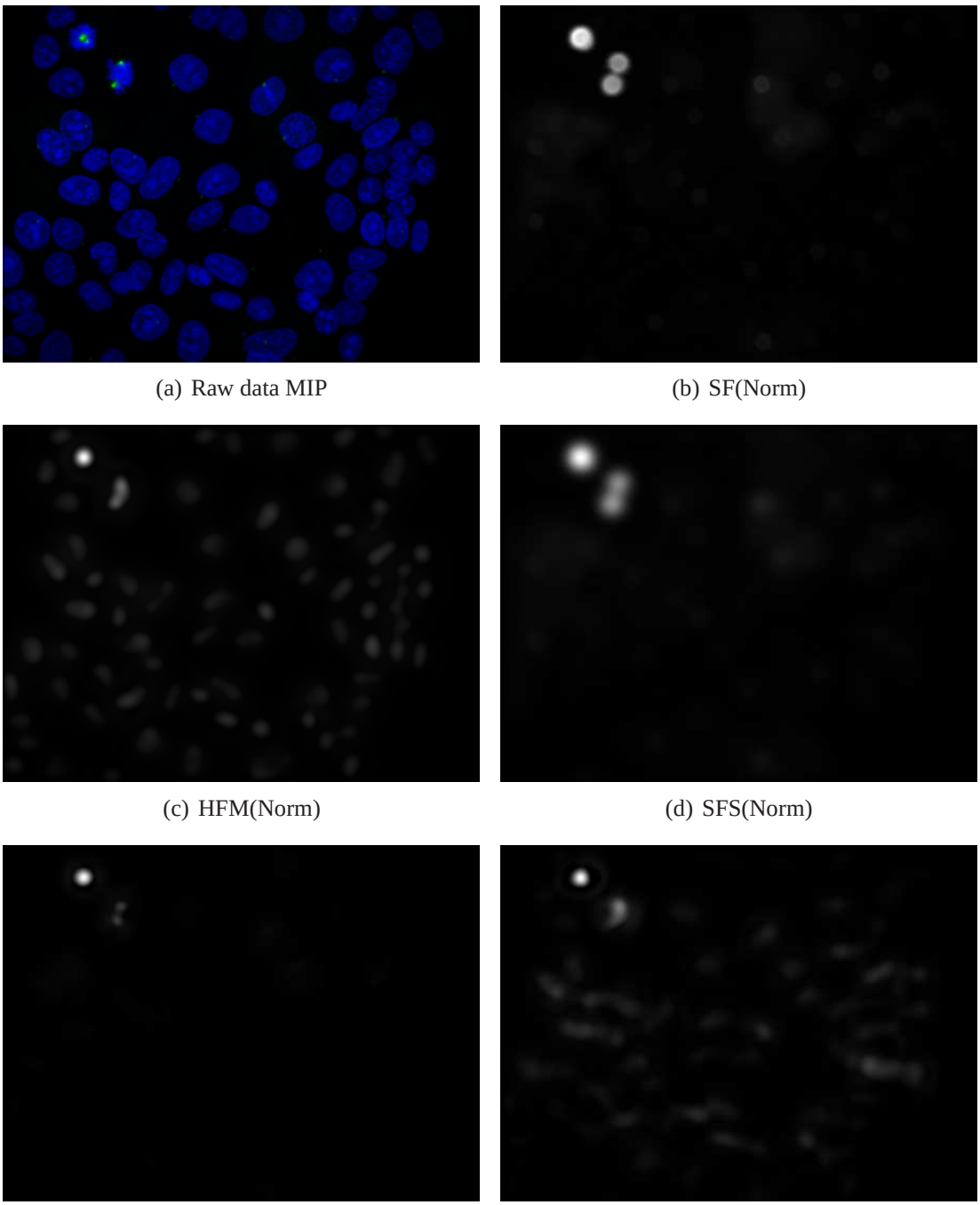

(a) Raw data MIP (b) SF(Norm)

(c) HFM(Norm) (d) SFS(Norm)

(e) HFMasym (f) HFM(GVF)

Figure 7.7: Filter responses for a DLD1 (STK15,1,DMSO) data set.

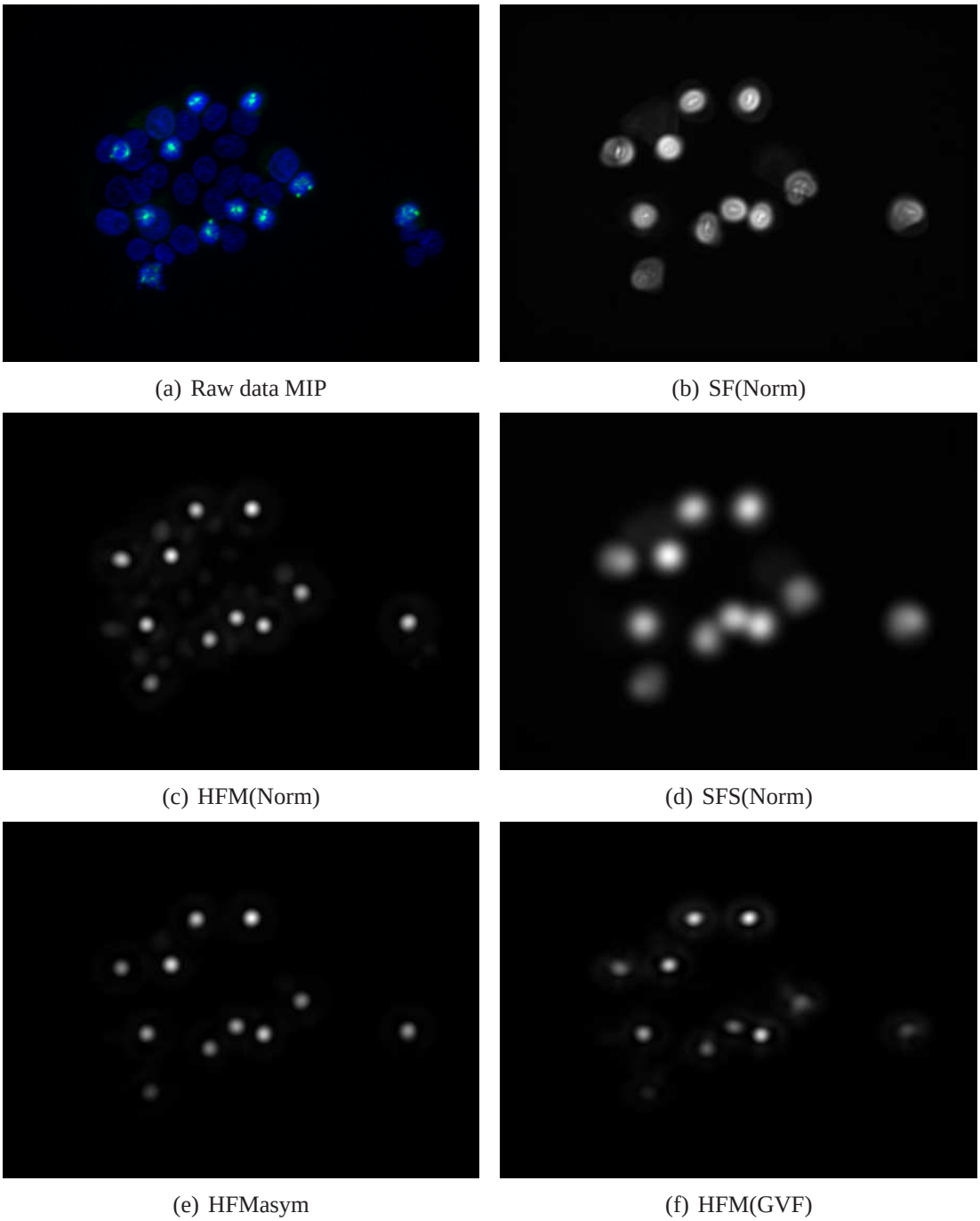

(a) Raw data MIP (b) SF(Norm)

(c) HFM(Norm) (d) SFS(Norm)

(e) HFMasym (f) HFM(GVF)

Figure 7.8: Filter responses for a HT29 (STK15,1) data set.

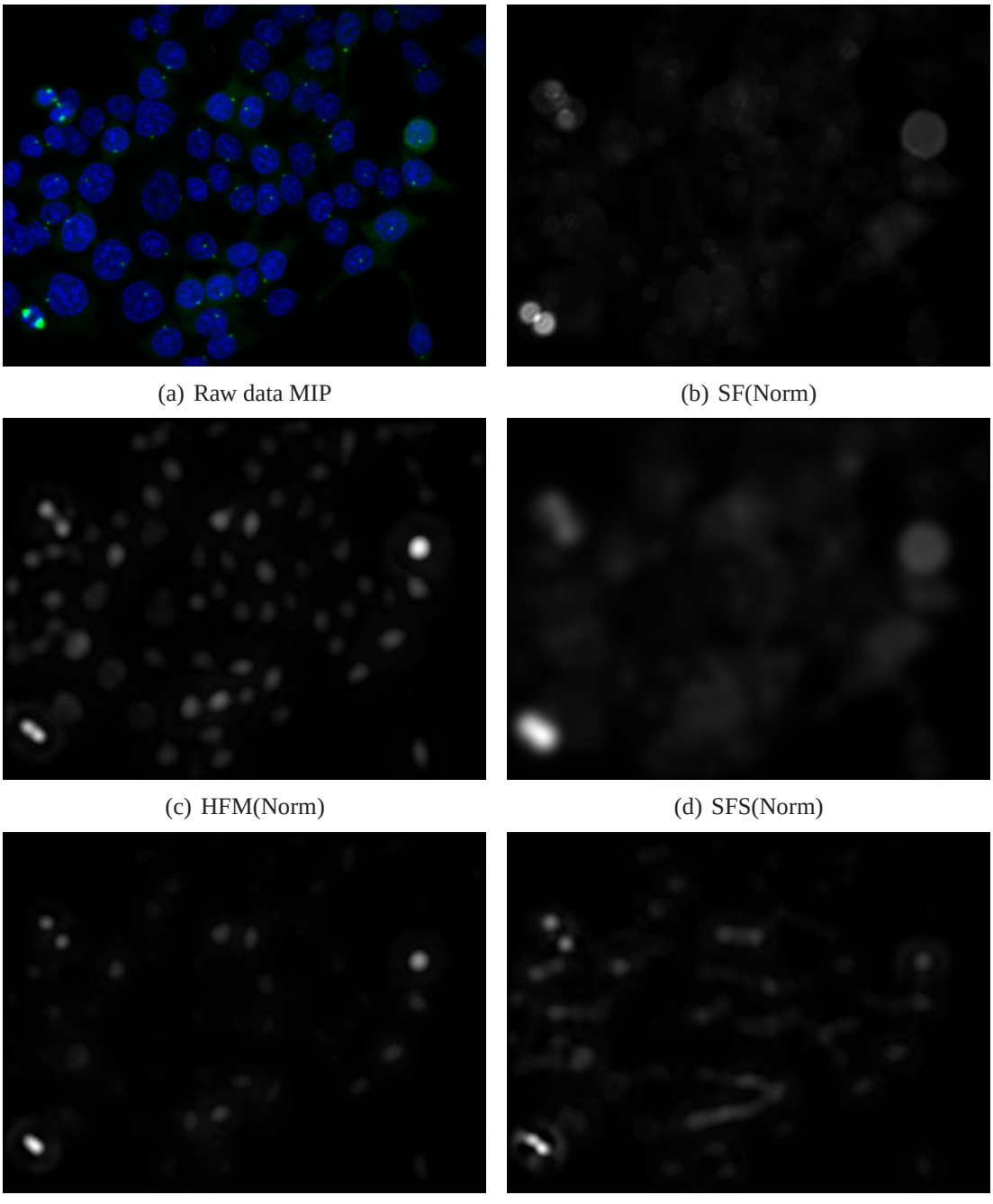

(a) Raw data MIP (b) SF(Norm)

(c) HFM(Norm) (d) SFS(Norm)

(e) HFMasym (f) HFM(GVF)

Figure 7.9: Filter responses for a HCT116 (STK15,1,DMSO) data set.

7.4 Cross Validation Results

In order to form our cell database, we extracted all mitosis cells of the original stacks (see appendix D). Since we had only few examples of DLD1 and HCT116, we decided to do a cross validation in order to compare our features. As classifier we chose a SVM with histogram intersection kernel, and a NN classifier. For the scaled SVM kernel we normalisation of our features with standard deviation.

Class	DLD1	HCT116	HT29	All Classes
# Samples	20	27	81	128

Table 7.2: Cell database details.

We computed seven different features. All features that involved sampling the input data on different shell radii, were evaluated at radii ranging from $1\mu m$ to $11\mu m$ with a step size of $1\mu m$.

SHD are SH-Descriptor computed on channel-1.

SHD-Multi are SH-Descriptors computed on channel-0 and channel-1. The resulting feature vectors were append to on large feature vector.

SHD-MultiC are the same as SHD-Multi, but additionally we computed for each radius the inner product of channel-0 and channel-1 expansion coefficients.

SHD-MIP is the SH-Descriptor computed on the maximum intensity projection of all shells.

SHD-AIP same SHD-MIP but using average intensity projection of all shells.

MISP-Multi are the MISP invariant computed of channel-0 and channel-1 with seven quantised gradient directions ranging $-\frac{6}{7}$ to $\frac{6}{7}$ with a step size of $\frac{1}{7}$.

MISP-MultiC are the same as MISP-Multi, but additionally we computed for each radius the inner product of quantised gradient directions of channel-0 and channel-1.

In table 7.3 on the facing page we present an overview of all cross validation results. SHD-Multi were the best with SVM as classifier. The most stable results were achieved with MISP-Multi, were we have nearly the same results for all classifiers.
Details on all cross validation results including confusion matrices can be found in appendix C.

Table 7.3: Overview of cross-validation statistics of the mitosis cell database. Each row shows the true positive rate for a specific feature. The best result for each classifier (single row) is printed in bold face.

Feature/Classifier	SVM	SVM (scaled)	1-NN (L1-Norm)	1-NN (L2-Norm)
SHD	69.53%	74.22%	67.2%	69.5%
SHD-Multi	**83.59%**	**82.03%**	70.3%	64.8%
SHD-AIP	68.75%	64.84%	68.0%	57.8%
SHD-MIP	70.31%	68.75%	69.5%	68.8%
SHD-MultiC	74.22%	81.25%	70.3%	64.8%
MISP-Multi	78.12%	78.12%	**78.1%**	**72.7%**
MISP-MultiC	75.78%	78.91%	71.9%	67.2%

7.5 Validation with Support Vector Machines

For validation we classified all detected maxima with a SVM. The best results were achieved with SHD- MIP descriptor. But the database was to small to come to a meaningful conclusion.

Feature	#Labels	#TP	#FP	#FN	#TN	#Detections
SHD-Multi	128	124	1857	0	3953	5934
SHD-MultiC	128	124	1877	0	3933	5934
MISP-MultiC	128	124	2462	0	3348	5934
MISP-Multi	128	124	2533	0	3277	5934
SHD- MIP	128	109	**104**	15	**5706**	5934
SHD- AIP	128	109	1277	15	4533	5934

Table 7.4: Overview of the validation results.

8 Conclusion and Outlook

This work presented a new approach towards image filtering of multi-channel 3D images and feature extraction methods.
We introduced a novel framework based harmonic filters that allows us to use multi-channel images and therefore information of more than one input channel. We achieved much better results as the standard algorithms used for single channel gray-scale images.
We successfully extended existing 3D invariant features such as SH-Descriptors an gray-scale MISP invariants to their multi-channel counterparts.

8.1 Outlook

The introduced algorithms form a good basis for further research and applications on multi-channel image filtering and feature extraction. But there are still issues that have to be addressed to.

Segmentation of the cells could increase the quality of the features and increase the classification results.
One should also consider a way to automatically select best parameters for radii and combinations of radii of our proposed features during the training phase.

Since we had only few tissue samples we were not able to do meaningful experiments and finally answer the question whether it is possible to train on cell line data and classify on tissue samples. Figure 8.1 and the following figures show tissue samples and filter responses of harmonic filters trained on cell line data. The results look very promising.

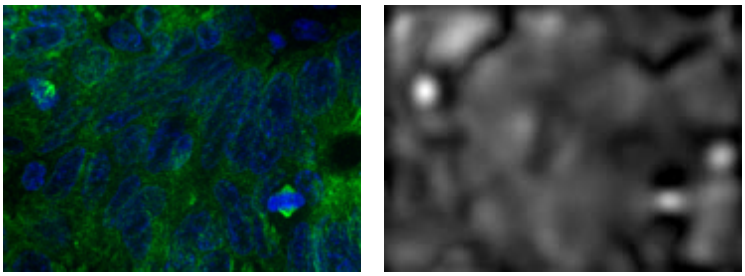

(a) Tissue raw data MIP (b) Filter response of HFM(Norm)

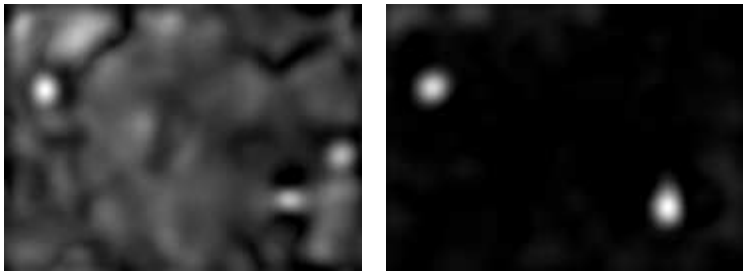

(c) Filter response of HF-Masym(Norm) (d) Filter response of HFM(GVF)

Figure 8.1: Filter response of harmonic filters on tissue sample (example 1). Filters were trained with cell line data.

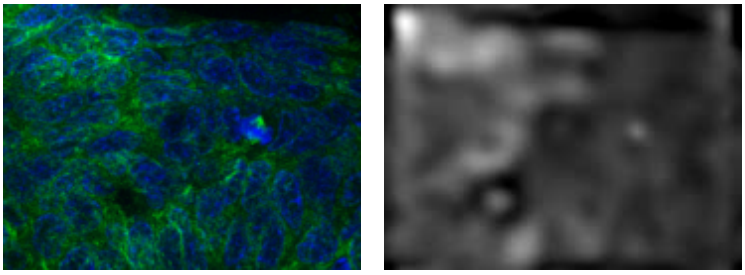

(a) Tissue raw data MIP (b) Filter response of HFM(Norm)

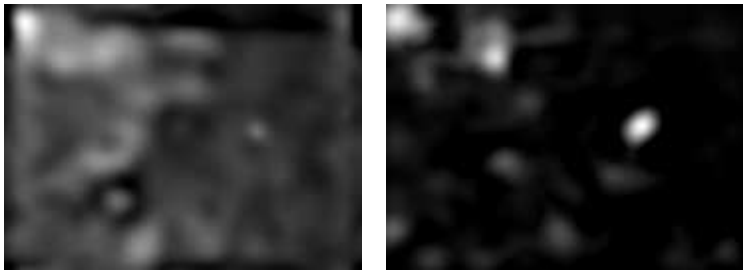

(c) Filter response of HF-Masym(Norm) (d) Filter response of HFM(GVF)

Figure 8.2: Filter response of harmonic filters on tissue sample (example 2). Filters were trained with cell line data.

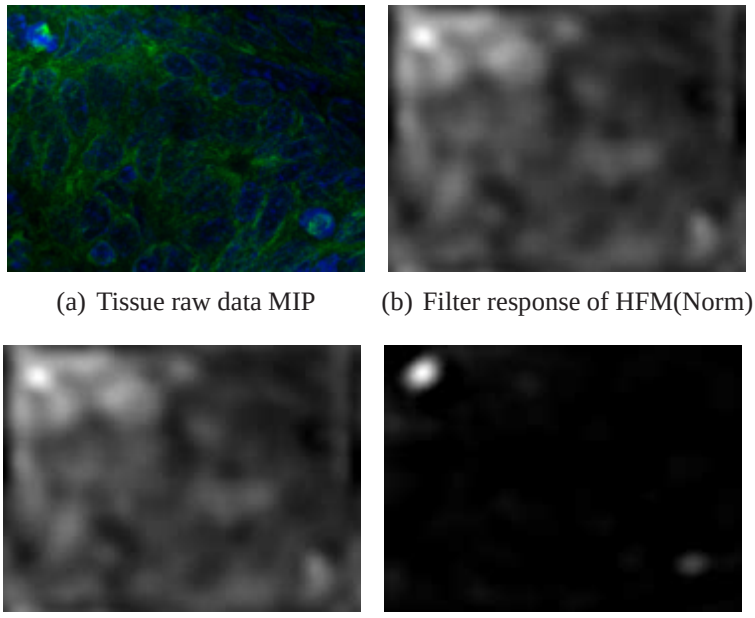

(a) Tissue raw data MIP (b) Filter response of HFM(Norm)

(c) Filter response of HF-Masym(Norm) (d) Filter response of HFM(GVF)

Figure 8.3: Filter response of harmonic filters on tissue sample (example 3). Filters were trained with cell line data.

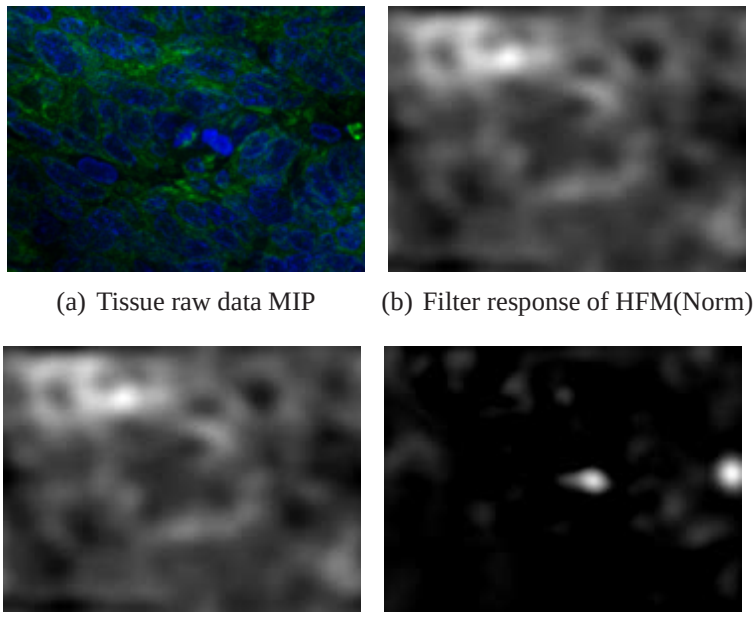

(a) Tissue raw data MIP (b) Filter response of HFM(Norm)

(c) Filter response of HF-Masym(Norm) (d) Filter response of HFM(GVF)

Figure 8.4: Filter response of harmonic filters on tissue sample (example 4). Filters were trained with cell line data.

A Appendix

A.1 Spherical Harmonics

We always use Racah-normalised spherical harmonics. In terms of Legendre polynomials they are written as

$$Y_m^\ell(\phi,\theta) = \sqrt{\frac{(l-m)!}{(l+m)!}} P_m^\ell(\cos(\theta)) e^{\mathbf{i}\phi}$$

Mostly we write $\mathbf{r}/r \in S^2$ instead of (ϕ,θ). The Racah-normalised solid harmonics can be written as

$$R_m^\ell(\mathbf{r}) = \sqrt{(\ell+m)!(\ell-m)!} \sum_{i,j,k} \frac{\delta_{i+j+k,\ell}\delta_{i-j,m}}{i!\,j!k!2^i 2^j} (x-\mathbf{i}y)^j(-x-\mathbf{i}y)^i z^k,$$

where $\mathbf{r} = (x,y,z)$. They are related to spherical harmonics by $R_m^\ell(\mathbf{r})/r^\ell = Y_m^\ell(\mathbf{r}/r)$

A.2 Clebsch Gordan Coefficients

Orthogonality

$$\sum_{j,m} \langle jm|j_1m_1, j_2m_2\rangle\langle jm|j_1m_1', j_2m_2'\rangle = \delta_{m_1,m_1'}\delta_{m_2,m_2'} \tag{A.1}$$

$$\sum_{m=m_1+m_2} \langle jm|j_1m_1, j_2m_2\rangle\langle j'm'|j_1m_1, j_2m_2\rangle = \delta_{j,j'}\delta_{m,m'} \tag{A.2}$$

$$\sum_{m_1,m} \langle jm|j_1m_1, j_2m_2\rangle\langle jm|j_1m_1, j_2'm_2'\rangle = \frac{2j+1}{2j_2'+1}\delta_{j_2,j_2'}\delta_{m_2,m_2'} \tag{A.3}$$

Special Values

$$\langle \ell m|(\ell-\lambda)(m-\mu),\lambda\mu\rangle = \begin{pmatrix} \ell+m \\ \lambda+\mu \end{pmatrix}^{1/2} \begin{pmatrix} \ell-m \\ \lambda-\mu \end{pmatrix}^{1/2} \begin{pmatrix} 2\ell \\ 2\lambda \end{pmatrix}^{-1/2} \tag{A.4}$$

$$\begin{aligned} \langle \ell m|(\ell+\lambda)(m-\mu),\lambda\mu\rangle = (-1)^{\lambda+\mu} &\begin{pmatrix} \ell+\lambda-m+\mu \\ \lambda+\mu \end{pmatrix}^{1/2} \\ &\begin{pmatrix} \ell+\lambda+m-\mu \\ \lambda-\mu \end{pmatrix}^{1/2} \begin{pmatrix} 2\ell+2\lambda+1 \\ 2\lambda \end{pmatrix}^{-1/2} \end{aligned} \tag{A.5}$$

Symmetry

$$\langle jm|j_1m_1, j_2m_2\rangle = \langle j_1m_1, j_2m_2|jm\rangle \tag{A.6}$$
$$\langle jm|j_1m_1, j_2m_2\rangle = (-1)^{j+j_1+j_2}\langle jm|j_2m_2, j_1m_1\rangle \tag{A.7}$$
$$\langle jm|j_1m_1, j_2m_2\rangle = (-1)^{j+j_1+j_2}\langle j(-m)|j_1(-m_1), j_2(-m_2)\rangle \tag{A.8}$$

A.3 Wigner D-Matrix

The components of $\mathbf{D}_g^\ell$ are written D_{mn}^ℓ. They are called the Wigner D-matrix. In Euler angles ϕ, θ, ψ in ZYZ-convention we have

$$D_{mn}^\ell(\phi, \theta, \psi) = e^{\mathbf{i}m\phi} d_{mn}^\ell(\theta) e^{\mathbf{i}n\psi},$$

where $d_{mn}^\ell(\theta)$ are the Wigner d-matrix which is real-valued. Relation to the Clebsch Gordan coefficients:

$$D_{mn}^\ell = \sum_{\substack{m_1+m_2=m \\ n_1+n_2=n}} D_{m_1n_1}^{\ell_1} D_{m_2n_2}^{\ell_2} \langle lm|l_1m_1, l_2m_2\rangle\langle ln|l_1n_1, l_2n_2\rangle \tag{A.9}$$

$$D_{m_1n_1}^{\ell_1} D_{m_2n_2}^{\ell_2} = \sum_{l,m,n} D_{mn}^\ell \langle lm|l_1m_1, l_2m_2\rangle\langle ln|l_1n_1, l_2n_2\rangle \tag{A.10}$$

B Details of all Filter Algorithms

B.1 Steerable Filter

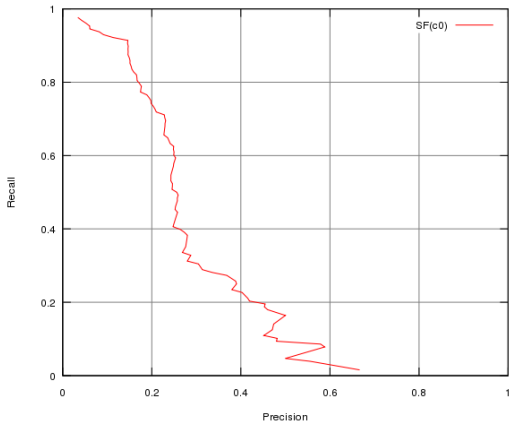

(a) Precision-Recall graph.

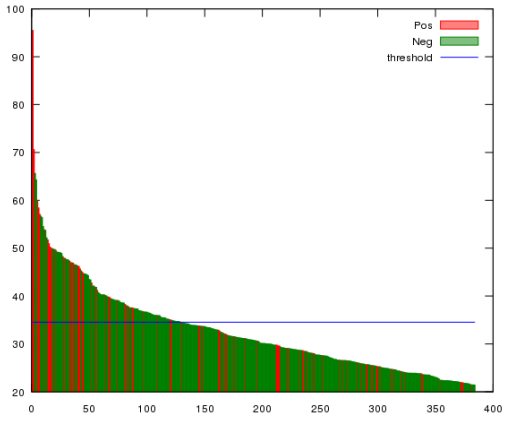

(b) Detection details and equal error rate threshold.

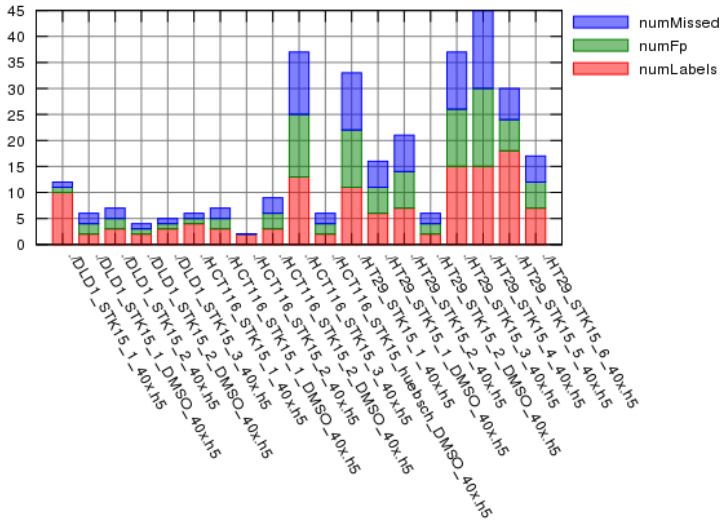

(c) Details per file.

Figure B.1: Details for SF(c0).

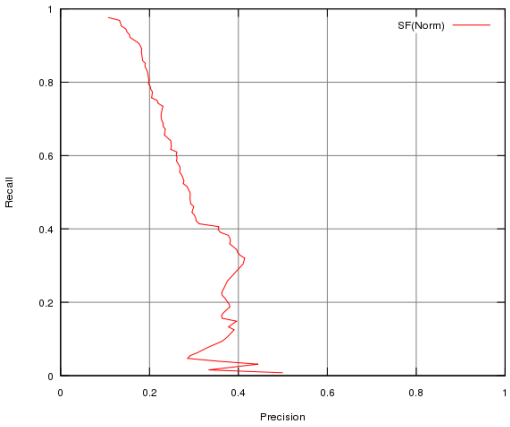

(a) Precision-Recall graph.

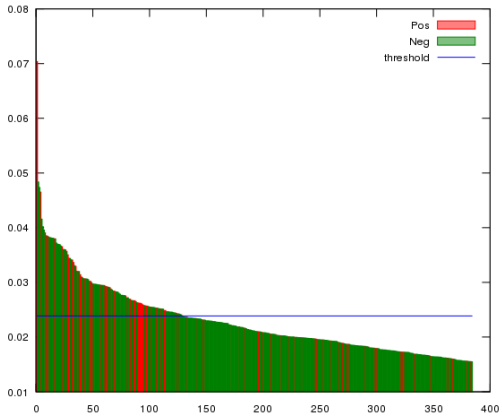

(b) Detection details and equal error rate threshold.

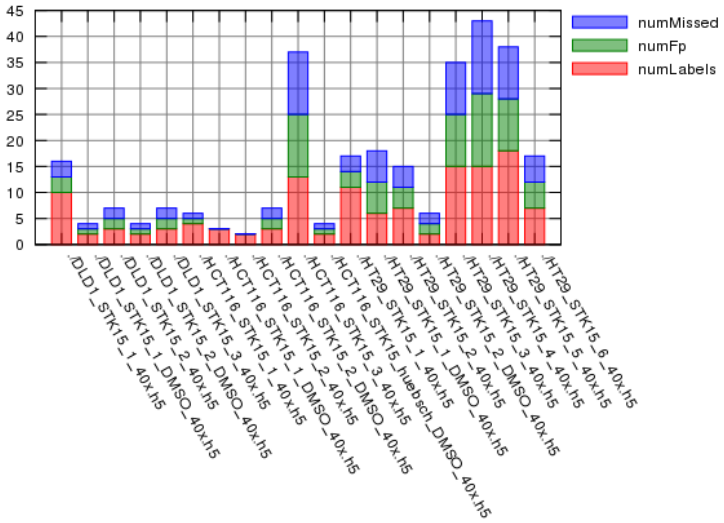

(c) Details per file.

Figure B.2: Details for SF(Norm).

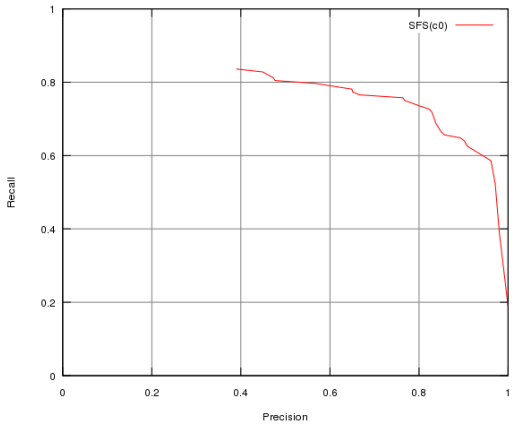

(a) Precision-Recall graph.

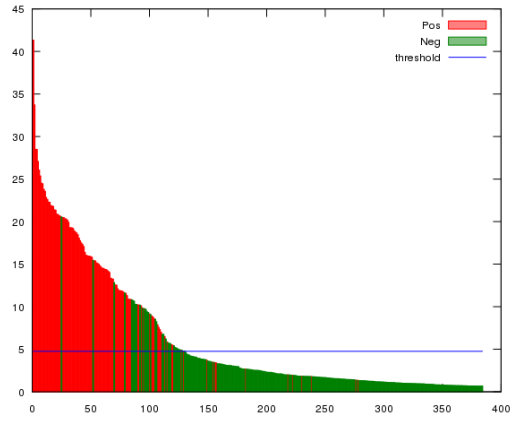

(b) Detection details and equal error rate threshold.

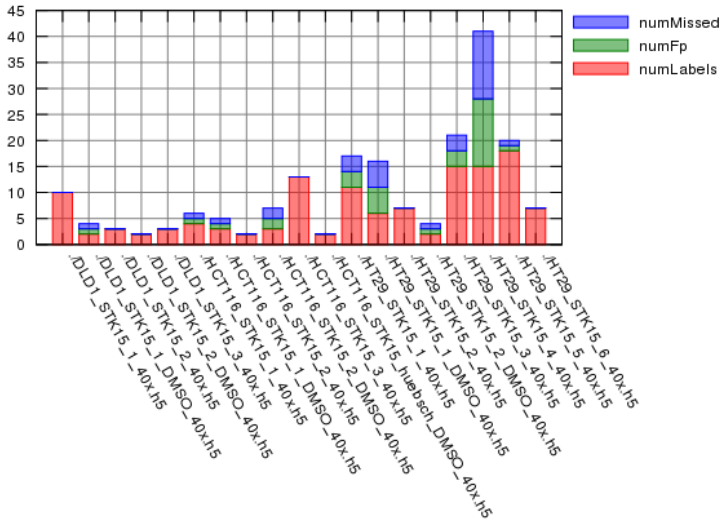

(c) Details per file.

Figure B.3: Details for SFS(c0).

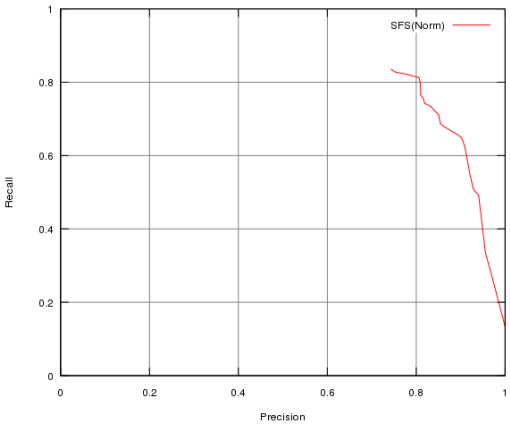

(a) Precision-Recall graph.

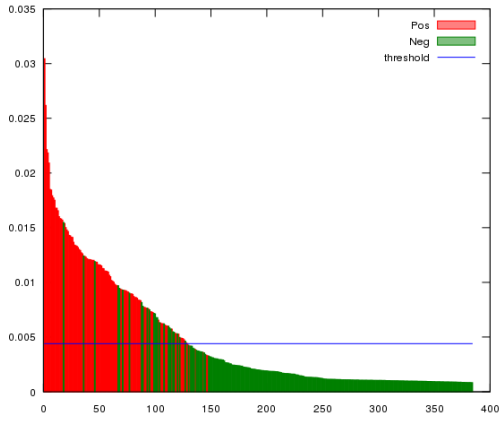

(b) Detection details and equal error rate threshold.

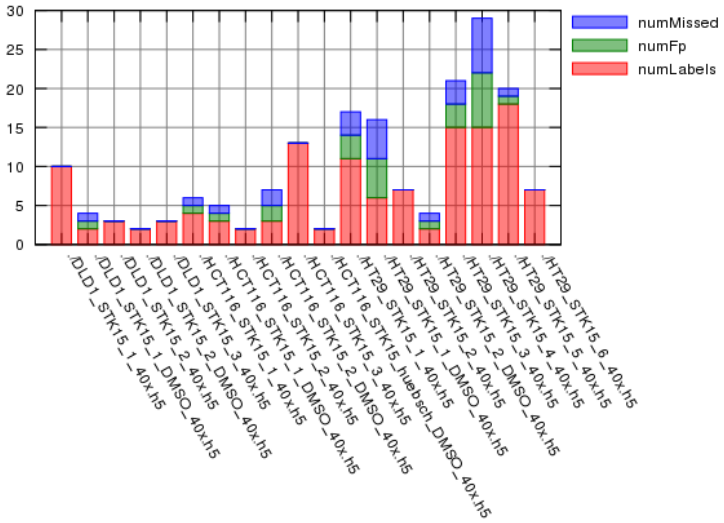

(c) Details per file.

Figure B.4: Details for SFS(Norm).

B.2 Harmonic Filter (Single Channel)

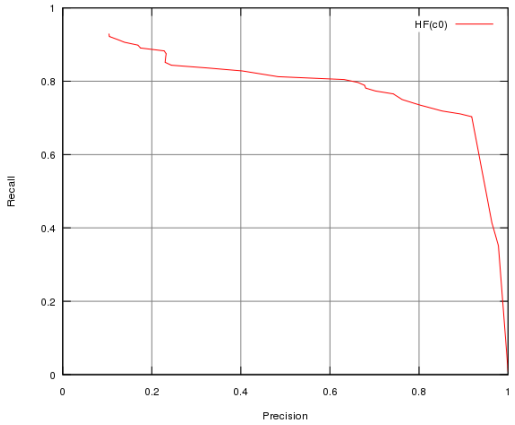

(a) Precision-Recall graph.

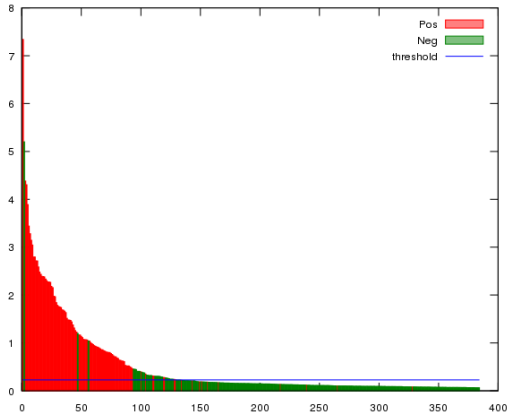

(b) Detection details and equal error rate threshold.

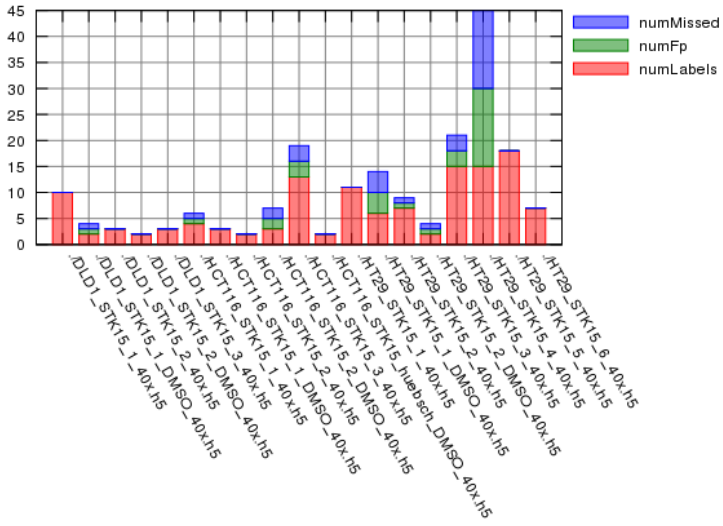

(c) Details per file.

Figure B.5: Details for HF(c0).

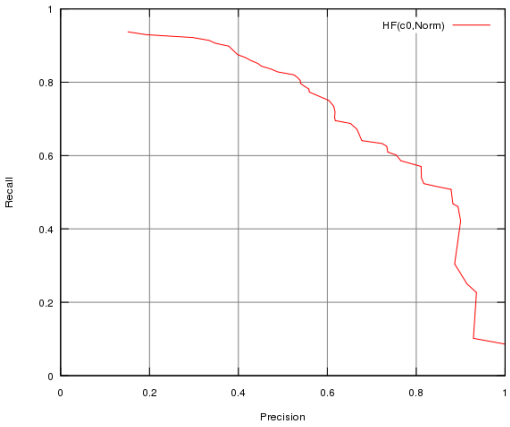

(a) Precision-Recall graph.

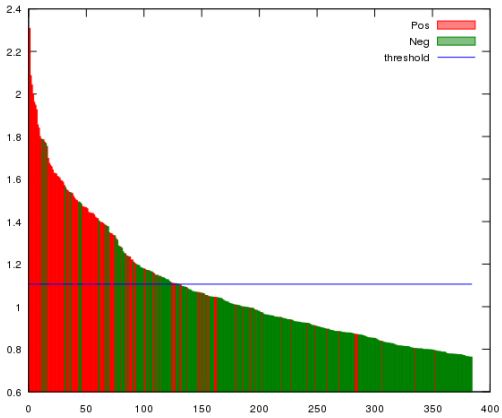

(b) Detection details and equal error rate threshold.

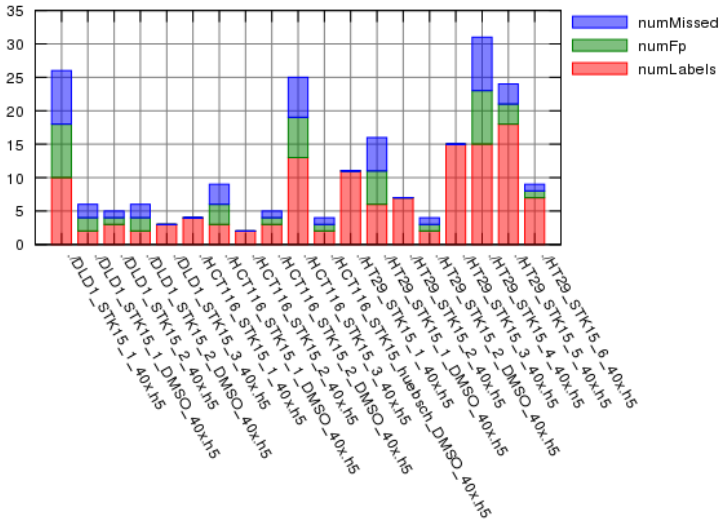

(c) Details per file.

Figure B.6: Details for HF(c0,Norm).

B.3 Harmonic Filter Multi-Channel

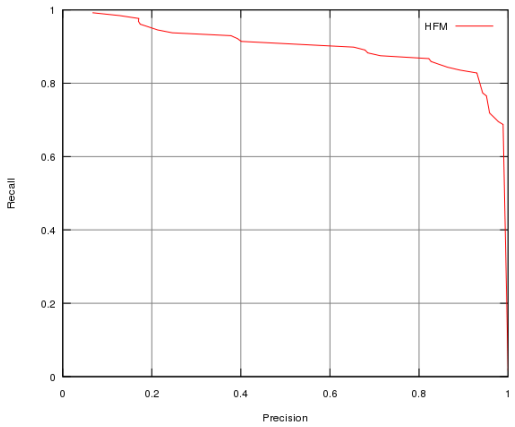

(a) Precision-Recall graph.

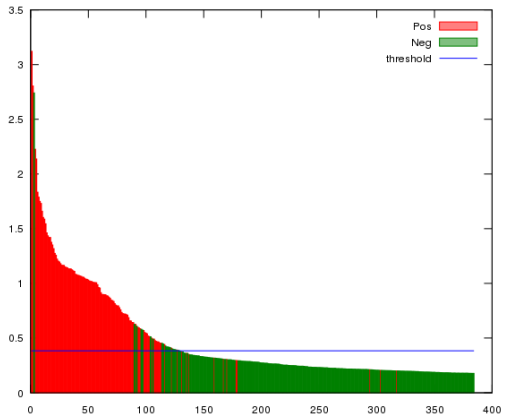

(b) Detection details and equal error rate threshold.

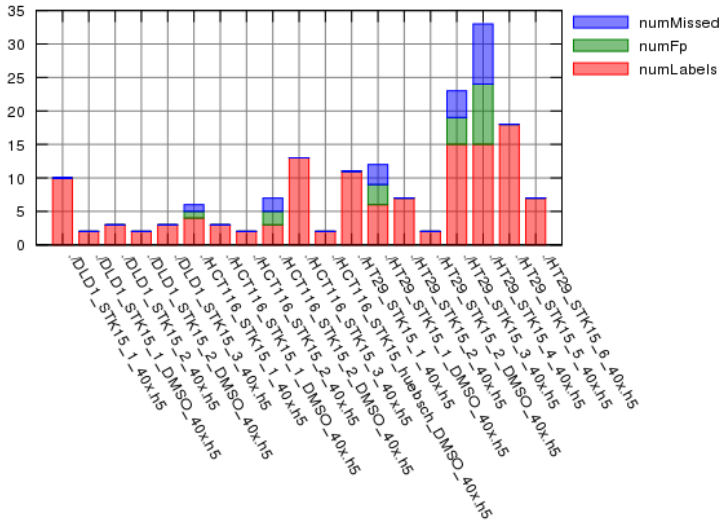

(c) Details per file.

Figure B.7: Details for HFM.

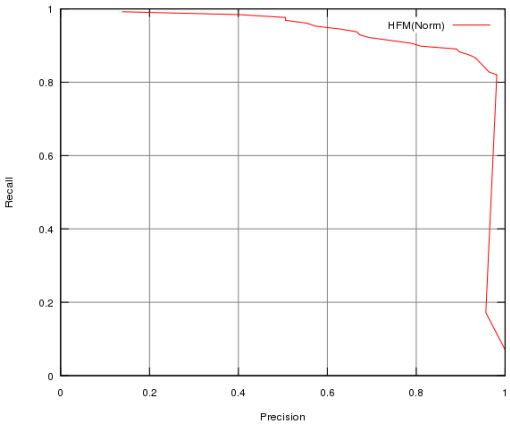

(a) Precision-Recall graph.

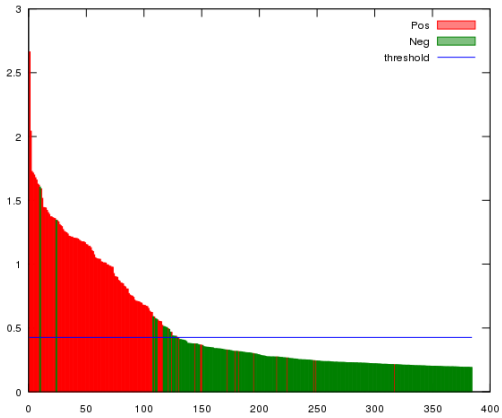

(b) Detection details and equal error rate threshold.

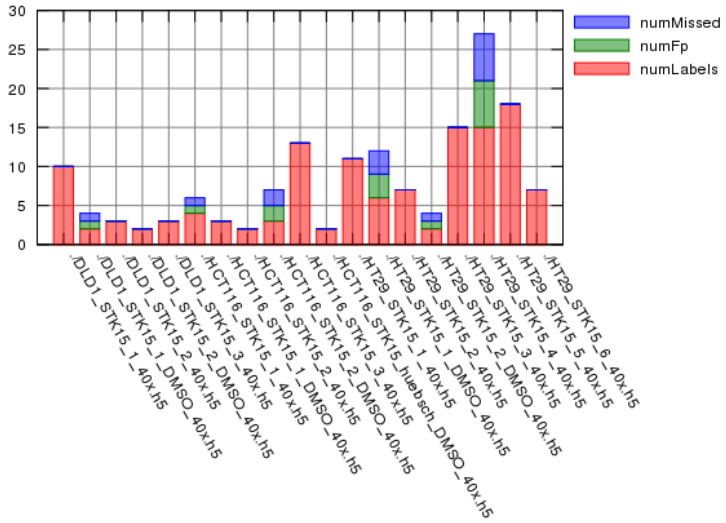

(c) Details per file.

Figure B.8: Details for HFM(Norm).

B.4 Harmonic Filter Multi Channel (GVF)

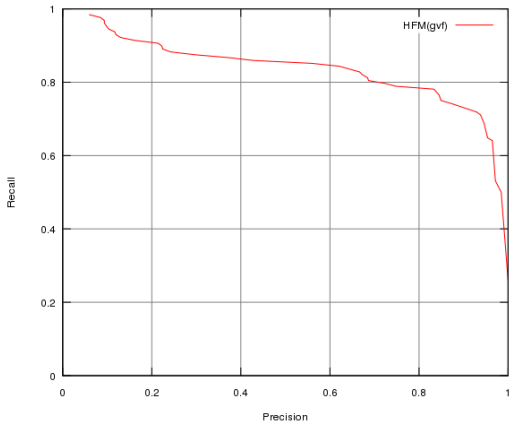

(a) Precision-Recall graph.

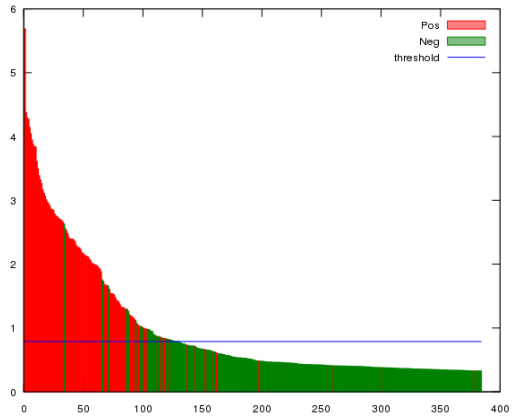

(b) Detection details and equal error rate threshold.

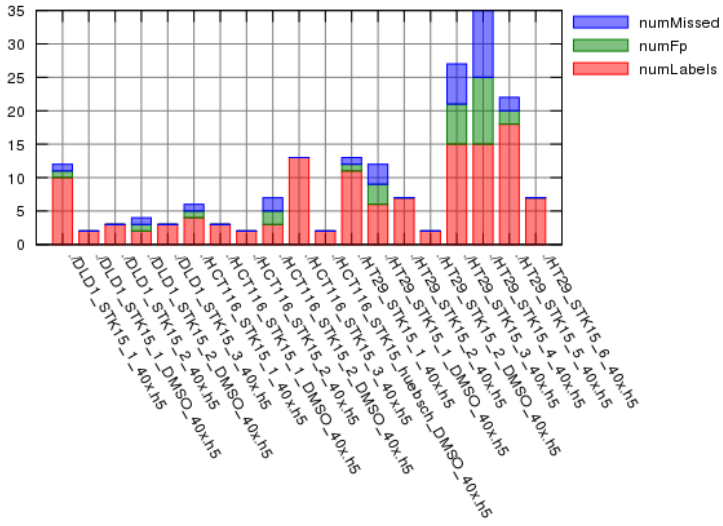

(c) Details per file.

Figure B.9: Details for HFM(GVF).

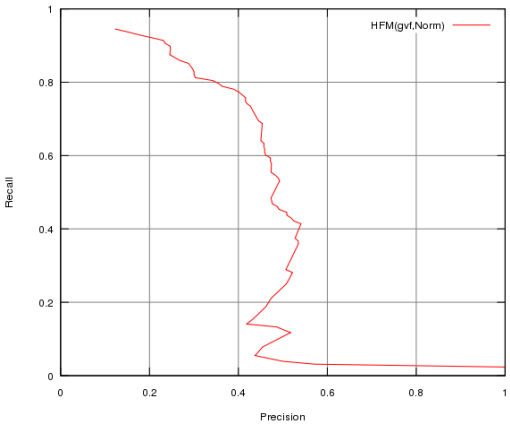

(a) Precision-Recall graph.

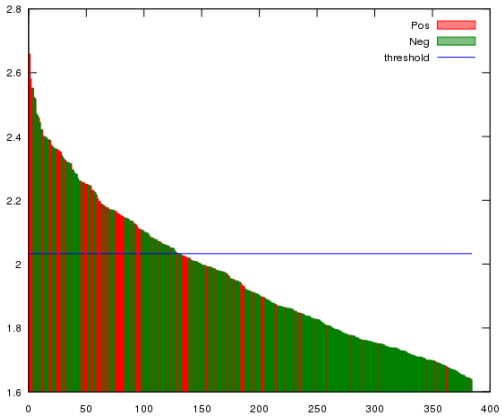

(b) Detection details and equal error rate threshold.

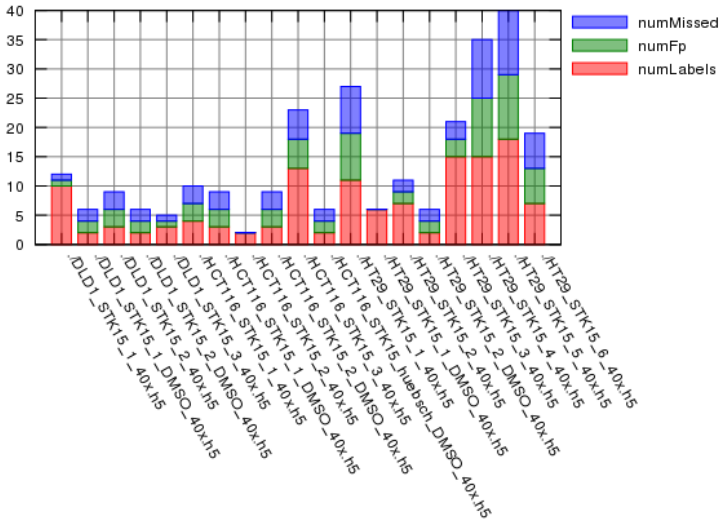

(c) Details per file.

Figure B.10: Details for HFM(GVF,Norm).

B.5 Harmonic Filter Multi Channel (Antisymmetric Products)

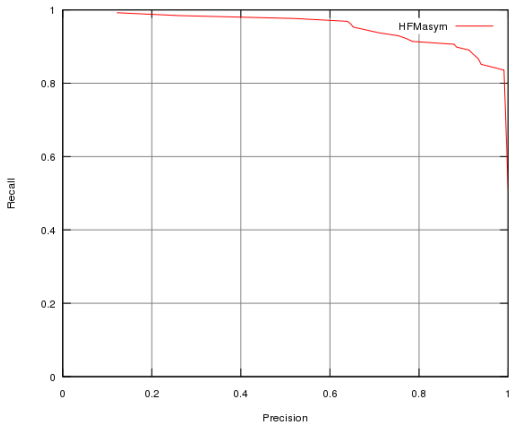

(a) Precision-Recall graph.

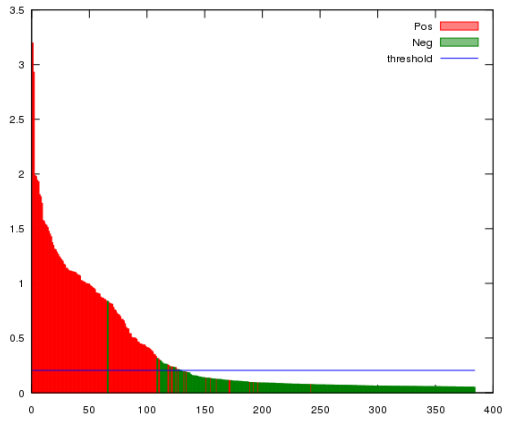

(b) Detection details and equal error rate threshold.

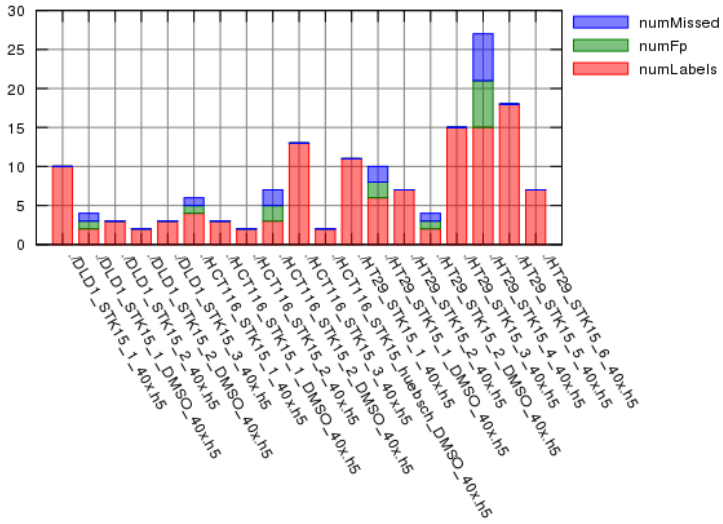

(c) Details per file.

Figure B.11: Details for HFMasym.

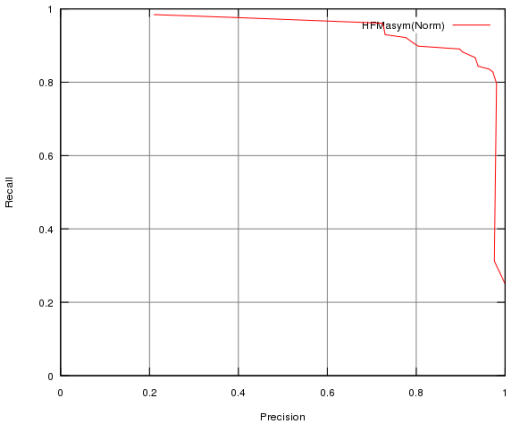

(a) Precision-Recall graph.

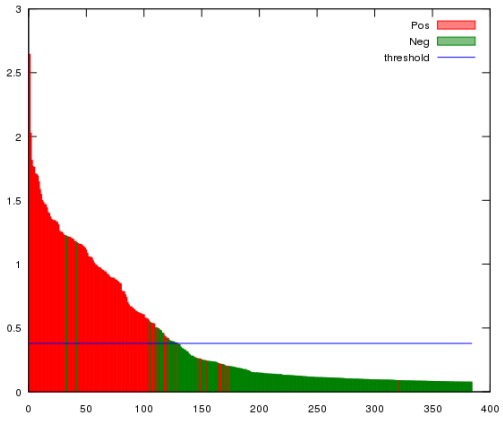

(b) Detection details and equal error rate threshold.

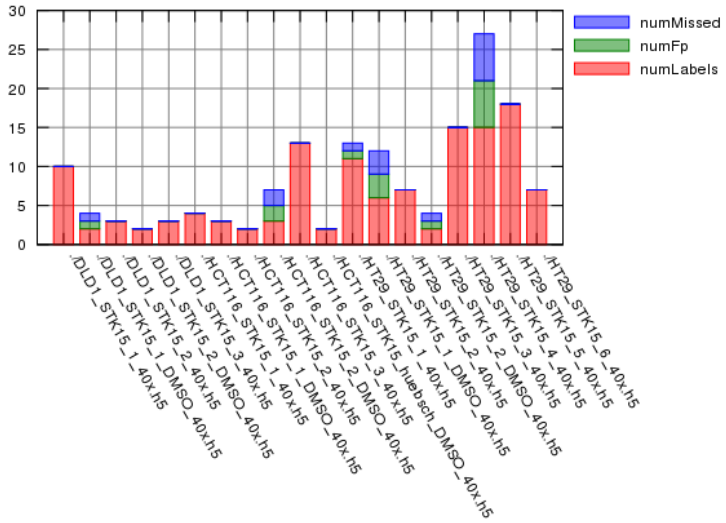

(c) Details per file.

Figure B.12: Details for HFMasym(Norm).

C Cross Validation Results

C.1 SVM Histogram Intersection Kernel

Table C.1: SHD

(a) Classification statistics

Class	True Positives (%)	False Positives (%)
DLD-1	5/20 (25%)	11/108 (10.19%)
HCT116	12/27 (44.44%)	15/101 (14.85%)
HT29	72/81 (88.89%)	13/47 (27.66%)
Total	89/128 (69.53%)	39/128 (30.47%)

(b) Confusion table

Class	DLD-1	HCT116	HT29
DLD-1	5	10	5
HCT116	7	12	8
HT29	4	5	72

Table C.2: SHD-Multi

(a) Classification statistics

Class	True Positives (%)	False Positives (%)
DLD-1	12/20 (60%)	2/108 (1.852%)
HCT116	18/27 (66.67%)	7/101 (6.931%)
HT29	77/81 (95.06%)	12/47 (25.53%)
Total	107/128 (83.59%)	21/128 (16.41%)

(b) Confusion table

Class	DLD-1	HCT116	HT29
DLD-1	12	4	4
HCT116	1	18	8
HT29	1	3	77

Table C.3: SHD-AIP

(a) Classification statistics

Class	True Positives (%)	False Positives (%)
DLD-1	7/20 (35%)	5/108 (4.63%)
HCT116	3/27 (11.11%)	2/101 (1.98%)
HT29	78/81 (96.3%)	33/47 (70.21%)
Total	88/128 (68.75%)	40/128 (31.25%)

(b) Confusion table

Class	DLD-1	HCT116	HT29
DLD-1	7	1	12
HCT116	3	3	21
HT29	2	1	78

Table C.4: SHD-MultiC

(a) Classification statistics

Class	True Positives (%)	False Positives (%)
DLD-1	11/20 (55%)	7/108 (6.481%)
HCT116	12/27 (44.44%)	14/101 (13.86%)
HT29	72/81 (88.89%)	12/47 (25.53%)
Total	95/128 (74.22%)	33/128 (25.78%)

(b) Confusion table

Class	DLD-1	HCT116	HT29
DLD-1	11	7	2
HCT116	5	12	10
HT29	2	7	72

Table C.5: MISP-MultiC

(a) Classification statistics

Class	True Positives (%)	False Positives (%)
DLD-1	10/20 (50%)	3/108 (2.778%)
HCT116	8/27 (29.63%)	7/101 (6.931%)
HT29	79/81 (97.53%)	21/47 (44.68%)
Total	97/128 (75.78%)	31/128 (24.22%)

(b) Confusion table

Class	DLD-1	HCT116	HT29
DLD-1	10	5	5
HCT116	3	8	16
HT29	0	2	79

Table C.6: SHD-MIP

(a) Classification statistics

Class	True Positives (%)	False Positives (%)
DLD-1	9/20 (45%)	4/108 (3.704%)
HCT116	3/27 (11.11%)	4/101 (3.96%)
HT29	78/81 (96.3%)	30/47 (63.83%)
Total	90/128 (70.31%)	38/128 (29.69%)

(b) Confusion table

Class	DLD-1	HCT116	HT29
DLD-1	9	2	9
HCT116	3	3	21
HT29	1	2	78

Table C.7: MISP-Multi

(a) Classification statistics

Class	True Positives (%)	False Positives (%)
DLD-1	12/20 (60%)	4/108 (3.704%)
HCT116	13/27 (48.15%)	12/101 (11.88%)
HT29	75/81 (92.59%)	12/47 (25.53%)
Total	100/128 (78.12%)	28/128 (21.88%)

(b) Confusion table

Class	DLD-1	HCT116	HT29
DLD-1	12	7	1
HCT116	3	13	11
HT29	1	5	75

C.2 SVM Histogram Intersection Kernel (scaled)

Table C.8: SHD

(a) Classification statistics

Class	True Positives (%)	False Positives (%)
DLD-1	6/20 (30%)	8/108 (7.407%)
HCT116	14/27 (51.85%)	15/101 (14.85%)
HT29	75/81 (92.59%)	10/47 (21.28%)
Total	95/128 (74.22%)	33/128 (25.78%)

(b) Confusion table

Class	DLD-1	HCT116	HT29
DLD-1	6	11	3
HCT116	6	14	7
HT29	2	4	75

Table C.9: SHD-AIP

(a) Classification statistics

Class	True Positives (%)	False Positives (%)
DLD-1	5/20 (25%)	10/108 (9.259%)
HCT116	5/27 (18.52%)	12/101 (11.88%)
HT29	73/81 (90.12%)	23/47 (48.94%)
Total	83/128 (64.84%)	45/128 (35.16%)

(b) Confusion table

Class	DLD-1	HCT116	HT29
DLD-1	5	7	8
HCT116	7	5	15
HT29	3	5	73

Table C.10: SHD-MIP

(a) Classification statistics

Class	True Positives (%)	False Positives (%)
DLD-1	9/20 (45%)	7/108 (6.481%)
HCT116	7/27 (25.93%)	10/101 (9.901%)
HT29	72/81 (88.89%)	23/47 (48.94%)
Total	88/128 (68.75%)	40/128 (31.25%)

(b) Confusion table

Class	DLD-1	HCT116	HT29
DLD-1	9	4	7
HCT116	4	7	16
HT29	3	6	72

Table C.11: MISP-Multi

(a) Classification statistics

Class	True Positives (%)	False Positives (%)
DLD-1	12/20 (60%)	5/108 (4.63%)
HCT116	12/27 (44.44%)	12/101 (11.88%)
HT29	76/81 (93.83%)	11/47 (23.4%)
Total	100/128 (78.12%)	28/128 (21.88%)

(b) Confusion table

Class	DLD-1	HCT116	HT29
DLD-1	12	7	1
HCT116	5	12	10
HT29	0	5	76

Table C.12: MISP-MultiC

(a) Classification statistics

Class	True Positives (%)	False Positives (%)
DLD-1	11/20 (55%)	5/108 (4.63%)
HCT116	14/27 (51.85%)	10/101 (9.901%)
HT29	76/81 (93.83%)	12/47 (25.53%)
Total	101/128 (78.91%)	27/128 (21.09%)

(b) Confusion table

Class	DLD-1	HCT116	HT29
DLD-1	11	7	2
HCT116	3	14	10
HT29	2	3	76

Table C.13: SHD-MultiC

(a) Classification statistics

Class	True Positives (%)	False Positives (%)
DLD-1	9/20 (45%)	5/108 (4.63%)
HCT116	18/27 (66.67%)	10/101 (9.901%)
HT29	77/81 (95.06%)	9/47 (19.15%)
Total	104/128 (81.25%)	24/128 (18.75%)

(b) Confusion table

Class	DLD-1	HCT116	HT29
DLD-1	9	9	3
HCT116	3	18	6
HT29	2	2	77

Table C.14: SHD-Multi

(a) Classification statistics

Class	True Positives (%)	False Positives (%)
DLD-1	11/20 (55%)	6/108 (5.556%)
HCT116	17/27 (62.96%)	9/101 (8.911%)
HT29	77/81 (95.06%)	8/47 (17.02%)
Total	105/128 (82.03%)	23/128 (17.97%)

(b) Confusion table

Class	DLD-1	HCT116	HT29
DLD-1	11	7	2
HCT116	4	17	6
HT29	2	2	77

C.3 NN Cross Validation Results

Table C.15: SHD

(a) Classification statistics (1-NN)

Class	True Positives (%)	False Positives (%)
DLD-1	8/20 (40.0%)	12/108 (11.1%)
HCT116	12/27 (44.4%)	15/101 (14.9%)
HT29	66/81 (81.5%)	15/47 (31.9%)
Total	86/128 (67.2%)	42/128 (32.8%)

(b) Confusion table (1-NN)

Class	DLD-1	HCT116	HT29
DLD-1	8	5	7
HCT116	6	12	9
HT29	3	12	66

(c) Classification statistics (2-NN)

Class	True Positives (%)	False Positives (%)
DLD-1	3/20 (15.0%)	17/108 (15.7%)
HCT116	3/27 (11.1%)	24/101 (23.8%)
HT29	60/81 (74.1%)	21/47 (44.7%)
Total	66/128 (51.6%)	62/128 (48.4%)

(d) Confusion table (2-NN)

Class	DLD-1	HCT116	HT29
DLD-1	3	8	9
HCT116	10	3	14
HT29	3	18	60

(e) Classification statistics (1-NN)

Class	True Positives (%)	False Positives (%)
DLD-1	9/20 (45.0%)	11/108 (10.2%)
HCT116	11/27 (40.7%)	16/101 (15.8%)
HT29	69/81 (85.2%)	12/47 (25.5%)
Total	89/128 (69.5%)	39/128 (30.5%)

(f) Confusion table (1-NN)

Class	DLD-1	HCT116	HT29
DLD-1	9	5	6
HCT116	7	11	9
HT29	2	10	69

(g) Classification statistics (2-NN)

Class	True Positives (%)	False Positives (%)
DLD-1	4/20 (20.0%)	16/108 (14.8%)
HCT116	1/27 (3.7%)	26/101 (25.7%)
HT29	58/81 (71.6%)	23/47 (48.9%)
Total	63/128 (49.2%)	65/128 (50.8%)

(h) Confusion table (2-NN)

Class	DLD-1	HCT116	HT29
DLD-1	4	6	10
HCT116	9	1	17
HT29	5	18	58

Table C.16: SHD-Multi

(a) Classification statistics (1-NN)

Class	True Positives (%)	False Positives (%)
DLD-1	12/20 (60.0%)	8/108 (7.4%)
HCT116	11/27 (40.7%)	16/101 (15.8%)
HT29	76/81 (93.8%)	5/47 (10.6%)
Total	99/128 (77.3%)	29/128 (22.7%)

(b) Confusion table (1-NN)

Class	DLD-1	HCT116	HT29
DLD-1	12	4	4
HCT116	4	11	12
HT29	1	4	76

(c) Classification statistics (2-NN)

Class	True Positives (%)	False Positives (%)
DLD-1	5/20 (25.0%)	15/108 (13.9%)
HCT116	5/27 (18.5%)	22/101 (21.8%)
HT29	67/81 (82.7%)	14/47 (29.8%)
Total	77/128 (60.2%)	51/128 (39.8%)

(d) Confusion table (2-NN)

Class	DLD-1	HCT116	HT29
DLD-1	5	6	9
HCT116	5	5	17
HT29	5	9	67

(e) Classification statistics (1-NN)

Class	True Positives (%)	False Positives (%)
DLD-1	6/20 (30.0%)	14/108 (13.0%)
HCT116	11/27 (40.7%)	16/101 (15.8%)
HT29	74/81 (91.4%)	7/47 (14.9%)
Total	91/128 (71.1%)	37/128 (28.9%)

(f) Confusion table (1-NN)

Class	DLD-1	HCT116	HT29
DLD-1	6	9	5
HCT116	4	11	12
HT29	0	7	74

(g) Classification statistics (2-NN)

Class	True Positives (%)	False Positives (%)
DLD-1	3/20 (15.0%)	17/108 (15.7%)
HCT116	7/27 (25.9%)	20/101 (19.8%)
HT29	69/81 (85.2%)	12/47 (25.5%)
Total	79/128 (61.7%)	49/128 (38.3%)

(h) Confusion table (2-NN)

Class	DLD-1	HCT116	HT29
DLD-1	3	9	8
HCT116	4	7	16
HT29	2	10	69

Table C.17: SHD-AIP

(a) Classification statistics (1-NN)

Class	True Positives (%)	False Positives (%)
DLD-1	10/20 (50.0%)	10/108 (9.3%)
HCT116	12/27 (44.4%)	15/101 (14.9%)
HT29	65/81 (80.2%)	16/47 (34.0%)
Total	87/128 (68.0%)	41/128 (32.0%)

(b) Confusion table (1-NN)

Class	DLD-1	HCT116	HT29
DLD-1	10	4	6
HCT116	3	12	12
HT29	5	11	65

(c) Classification statistics (2-NN)

Class	True Positives (%)	False Positives (%)
DLD-1	2/20 (10.0%)	18/108 (16.7%)
HCT116	4/27 (14.8%)	23/101 (22.8%)
HT29	52/81 (64.2%)	29/47 (61.7%)
Total	58/128 (45.3%)	70/128 (54.7%)

(d) Confusion table (2-NN)

Class	DLD-1	HCT116	HT29
DLD-1	2	8	10
HCT116	4	4	19
HT29	7	22	52

(e) Classification statistics (1-NN)

Class	True Positives (%)	False Positives (%)
DLD-1	9/20 (45.0%)	11/108 (10.2%)
HCT116	9/27 (33.3%)	18/101 (17.8%)
HT29	56/81 (69.1%)	25/47 (53.2%)
Total	74/128 (57.8%)	54/128 (42.2%)

(f) Confusion table (1-NN)

Class	DLD-1	HCT116	HT29
DLD-1	9	5	6
HCT116	4	9	14
HT29	7	18	56

(g) Classification statistics (2-NN)

Class	True Positives (%)	False Positives (%)
DLD-1	2/20 (10.0%)	18/108 (16.7%)
HCT116	3/27 (11.1%)	24/101 (23.8%)
HT29	51/81 (63.0%)	30/47 (63.8%)
Total	56/128 (43.8%)	72/128 (56.2%)

(h) Confusion table (2-NN)

Class	DLD-1	HCT116	HT29
DLD-1	2	10	8
HCT116	5	3	19
HT29	8	22	51

Table C.18: SHD-MIP

(a) Classification statistics (1-NN)

Class	True Positives (%)	False Positives (%)
DLD-1	9/20 (45.0%)	11/108 (10.2%)
HCT116	11/27 (40.7%)	16/101 (15.8%)
HT29	69/81 (85.2%)	12/47 (25.5%)
Total	89/128 (69.5%)	39/128 (30.5%)

(b) Confusion table (1-NN)

Class	DLD-1	HCT116	HT29
DLD-1	9	4	7
HCT116	3	11	13
HT29	2	10	69

(c) Classification statistics (2-NN)

Class	True Positives (%)	False Positives (%)
DLD-1	5/20 (25.0%)	15/108 (13.9%)
HCT116	5/27 (18.5%)	22/101 (21.8%)
HT29	51/81 (63.0%)	30/47 (63.8%)
Total	61/128 (47.7%)	67/128 (52.3%)

(d) Confusion table (2-NN)

Class	DLD-1	HCT116	HT29
DLD-1	5	6	9
HCT116	4	5	18
HT29	9	21	51

(e) Classification statistics (1-NN)

Class	True Positives (%)	False Positives (%)
DLD-1	8/20 (40.0%)	12/108 (11.1%)
HCT116	13/27 (48.1%)	14/101 (13.9%)
HT29	67/81 (82.7%)	14/47 (29.8%)
Total	88/128 (68.8%)	40/128 (31.2%)

(f) Confusion table (1-NN)

Class	DLD-1	HCT116	HT29
DLD-1	8	4	8
HCT116	5	13	9
HT29	4	10	67

(g) Classification statistics (2-NN)

Class	True Positives (%)	False Positives (%)
DLD-1	2/20 (10.0%)	18/108 (16.7%)
HCT116	6/27 (22.2%)	21/101 (20.8%)
HT29	52/81 (64.2%)	29/47 (61.7%)
Total	60/128 (46.9%)	68/128 (53.1%)

(h) Confusion table (2-NN)

Class	DLD-1	HCT116	HT29
DLD-1	2	8	10
HCT116	6	6	15
HT29	7	22	52

Table C.19: MISP-Multi

(a) Classification statistics (1-NN)

Class	True Positives (%)	False Positives (%)
DLD-1	12/20 (60.0%)	8/108 (7.4%)
HCT116	14/27 (51.9%)	13/101 (12.9%)
HT29	74/81 (91.4%)	7/47 (14.9%)
Total	100/128 (78.1%)	28/128 (21.9%)

(b) Confusion table (1-NN)

Class	DLD-1	HCT116	HT29
DLD-1	12	5	3
HCT116	5	14	8
HT29	1	6	74

(c) Classification statistics (2-NN)

Class	True Positives (%)	False Positives (%)
DLD-1	8/20 (40.0%)	12/108 (11.1%)
HCT116	8/27 (29.6%)	19/101 (18.8%)
HT29	69/81 (85.2%)	12/47 (25.5%)
Total	85/128 (66.4%)	43/128 (33.6%)

(d) Confusion table (2-NN)

Class	DLD-1	HCT116	HT29
DLD-1	8	7	5
HCT116	8	8	11
HT29	3	9	69

(e) Classification statistics (1-NN)

Class	True Positives (%)	False Positives (%)
DLD-1	8/20 (40.0%)	12/108 (11.1%)
HCT116	16/27 (59.3%)	11/101 (10.9%)
HT29	69/81 (85.2%)	12/47 (25.5%)
Total	93/128 (72.7%)	35/128 (27.3%)

(f) Confusion table (1-NN)

Class	DLD-1	HCT116	HT29
DLD-1	8	5	7
HCT116	1	16	10
HT29	4	8	69

(g) Classification statistics (2-NN)

Class	True Positives (%)	False Positives (%)
DLD-1	2/20 (10.0%)	18/108 (16.7%)
HCT116	11/27 (40.7%)	16/101 (15.8%)
HT29	59/81 (72.8%)	22/47 (46.8%)
Total	72/128 (56.2%)	56/128 (43.8%)

(h) Confusion table (2-NN)

Class	DLD-1	HCT116	HT29
DLD-1	2	6	12
HCT116	3	11	13
HT29	8	14	59

Table C.20: MISP-MultiC

(a) Classification statistics (1-NN)

Class	True Positives (%)	False Positives (%)
DLD-1	8/20 (40.0%)	12/108 (11.1%)
HCT116	15/27 (55.6%)	12/101 (11.9%)
HT29	69/81 (85.2%)	12/47 (25.5%)
Total	92/128 (71.9%)	36/128 (28.2%)

(b) Confusion table (1-NN)

Class	DLD-1	HCT116	HT29
DLD-1	8	4	8
HCT116	1	15	11
HT29	4	8	69

(c) Classification statistics (2-NN)

Class	True Positives (%)	False Positives (%)
DLD-1	4/20 (20.0%)	16/108 (14.8%)
HCT116	9/27 (33.3%)	18/101 (17.8%)
HT29	62/81 (76.5%)	19/47 (40.4%)
Total	75/128 (58.6%)	53/128 (41.4%)

(d) Confusion table (2-NN)

Class	DLD-1	HCT116	HT29
DLD-1	4	5	11
HCT116	1	9	17
HT29	4	15	62

(e) Classification statistics (1-NN)

Class	True Positives (%)	False Positives (%)
DLD-1	7/20 (35.0%)	13/108 (12.0%)
HCT116	13/27 (48.1%)	14/101 (13.9%)
HT29	66/81 (81.5%)	15/47 (31.9%)
Total	86/128 (67.2%)	42/128 (32.8%)

(f) Confusion table (1-NN)

Class	DLD-1	HCT116	HT29
DLD-1	7	2	11
HCT116	3	13	11
HT29	4	11	66

(g) Classification statistics (2-NN)

Class	True Positives (%)	False Positives (%)
DLD-1	2/20 (10.0%)	18/108 (16.7%)
HCT116	3/27 (11.1%)	24/101 (23.8%)
HT29	47/81 (58.0%)	34/47 (72.3%)
Total	52/128 (40.6%)	76/128 (59.4%)

(h) Confusion table (2-NN)

Class	DLD-1	HCT116	HT29
DLD-1	2	4	14
HCT116	3	3	21
HT29	7	27	47

Table C.21: SHD-MultiC

(a) Classification statistics (1-NN)

Class	True Positives (%)	False Positives (%)
DLD-1	10/20 (50.0%)	10/108 (9.3%)
HCT116	12/27 (44.4%)	15/101 (14.9%)
HT29	68/81 (84.0%)	13/47 (27.7%)
Total	90/128 (70.3%)	38/128 (29.7%)

(b) Confusion table (1-NN)

Class	DLD-1	HCT116	HT29
DLD-1	10	7	3
HCT116	7	12	8
HT29	3	10	68

(c) Classification statistics (2-NN)

Class	True Positives (%)	False Positives (%)
DLD-1	5/20 (25.0%)	15/108 (13.9%)
HCT116	3/27 (11.1%)	24/101 (23.8%)
HT29	65/81 (80.2%)	16/47 (34.0%)
Total	73/128 (57.0%)	55/128 (43.0%)

(d) Confusion table (2-NN)

Class	DLD-1	HCT116	HT29
DLD-1	5	11	4
HCT116	12	3	12
HT29	3	13	65

(e) Classification statistics (1-NN)

Class	True Positives (%)	False Positives (%)
DLD-1	9/20 (45.0%)	11/108 (10.2%)
HCT116	8/27 (29.6%)	19/101 (18.8%)
HT29	66/81 (81.5%)	15/47 (31.9%)
Total	83/128 (64.8%)	45/128 (35.2%)

(f) Confusion table (1-NN)

Class	DLD-1	HCT116	HT29
DLD-1	9	7	4
HCT116	8	8	11
HT29	1	14	66

(g) Classification statistics (2-NN)

Class	True Positives (%)	False Positives (%)
DLD-1	6/20 (30.0%)	14/108 (13.0%)
HCT116	2/27 (7.4%)	25/101 (24.8%)
HT29	60/81 (74.1%)	21/47 (44.7%)
Total	68/128 (53.1%)	60/128 (26.9%)

(h) Confusion table (2-NN)

Class	DLD-1	HCT116	HT29
DLD-1	6	9	5
HCT116	9	2	16
HT29	2	19	60

D Overview of the Data

D.1 Treated Group (Nocodacole)

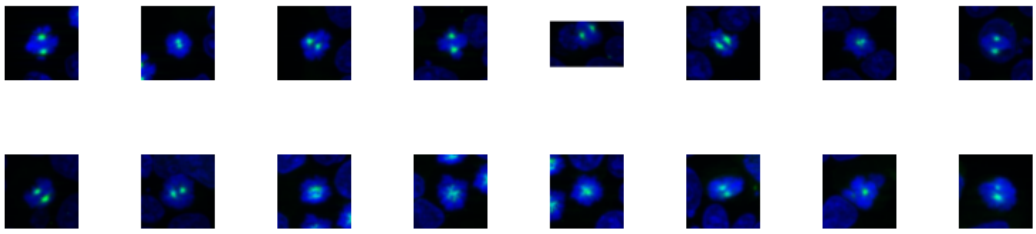

Figure D.1: Treated Group DLD (Nocodacole)

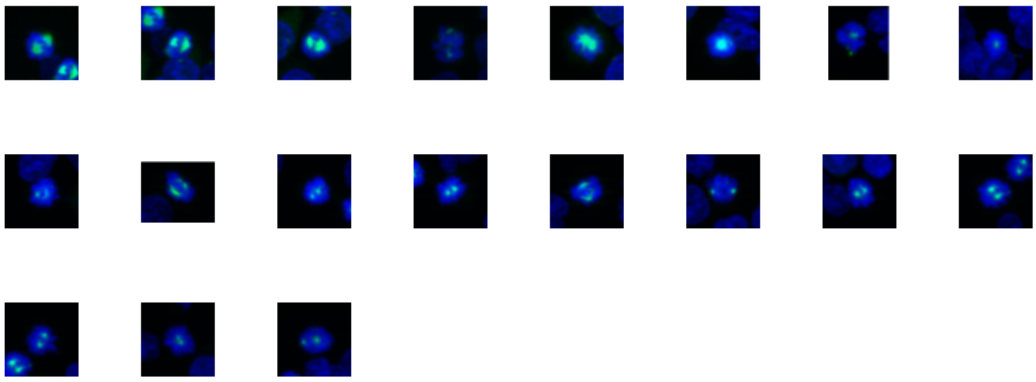

Figure D.2: Treated Group HCT116 (Nocodacole)

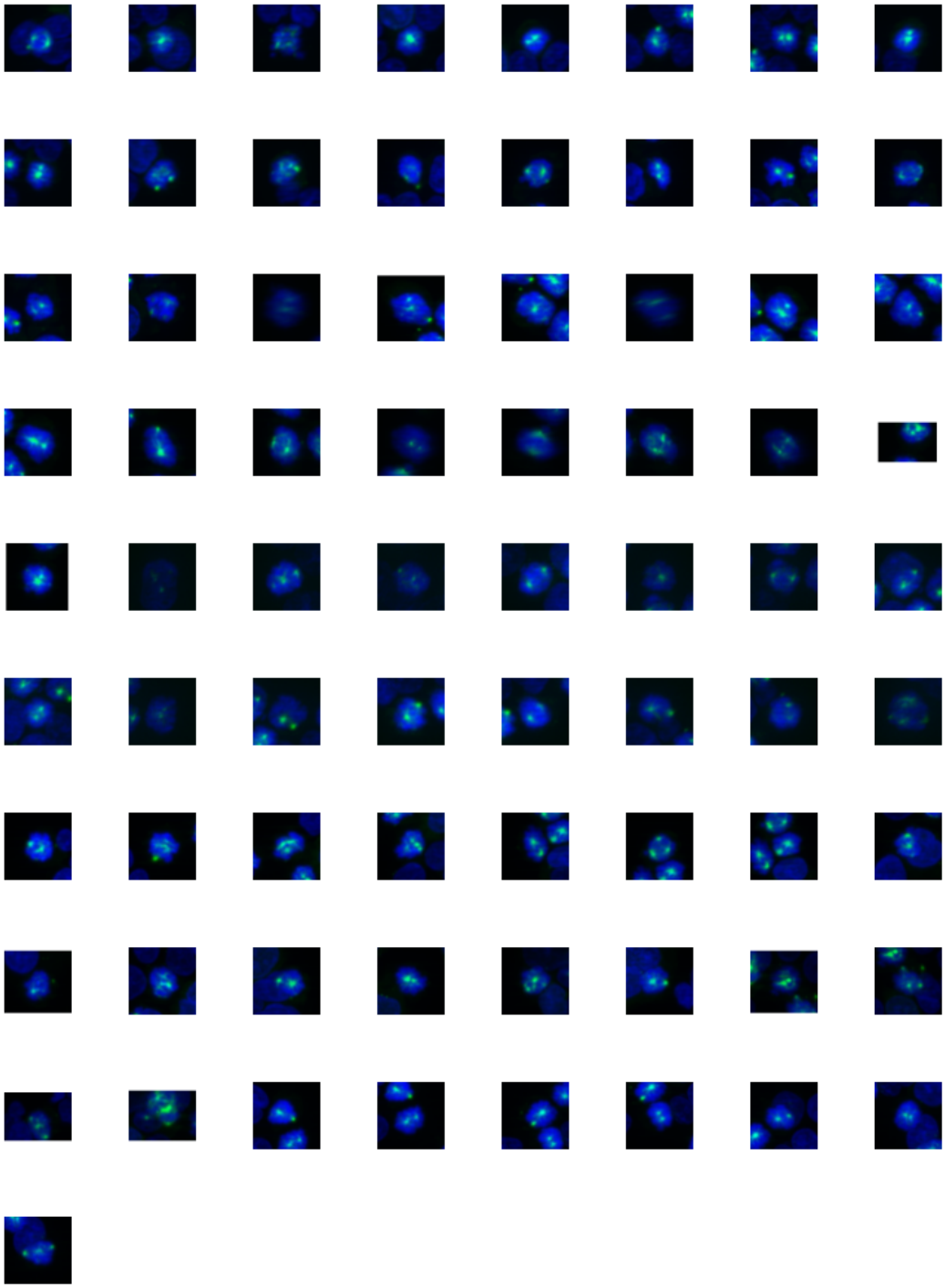

Figure D.3: Treated Group HT29 (Nocodacole)

D.2 Control Group (DMSO)

Figure D.4: Control Group DLD (DMSO)

Figure D.5: Control Group HCT116 (DMSO)

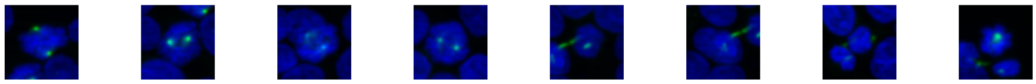

Figure D.6: Control Group HT29 (DMSO)

D.3 Data sets

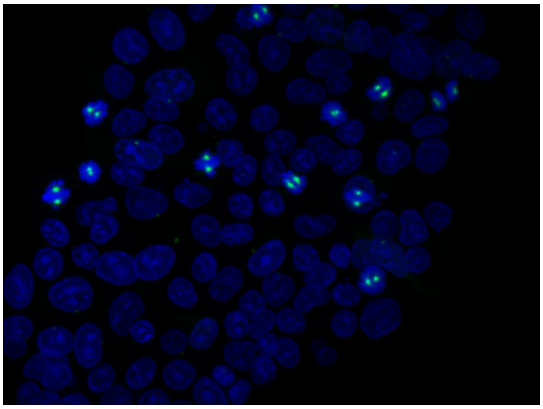

(a) DLD1 STK15 1 40x

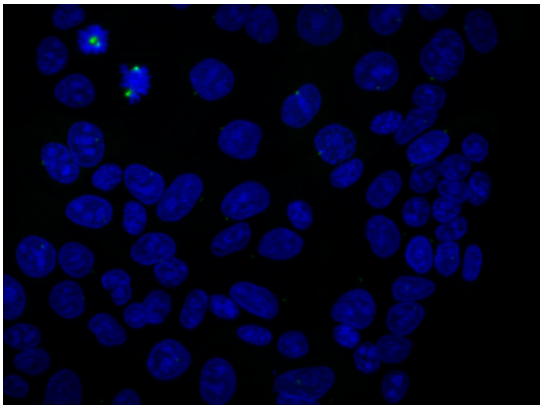

(b) DLD1 STK15 1 DMSO 40x

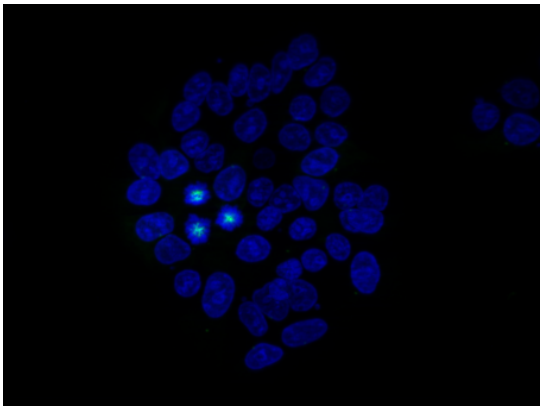

(c) DLD1 STK15 2 40x

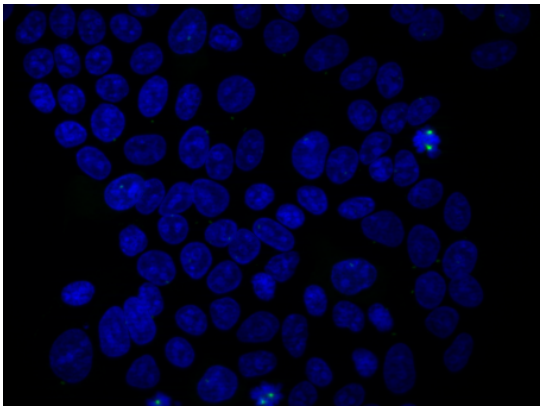

(d) DLD1 STK15 2 DMSO 40x

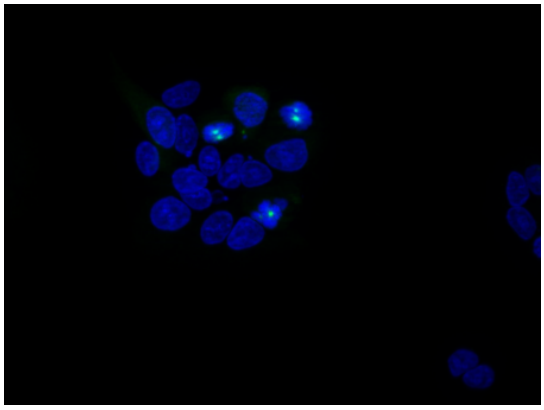

(e) DLD1 STK15 3 40x

Figure D.7: Raw images of DLD1 cells.

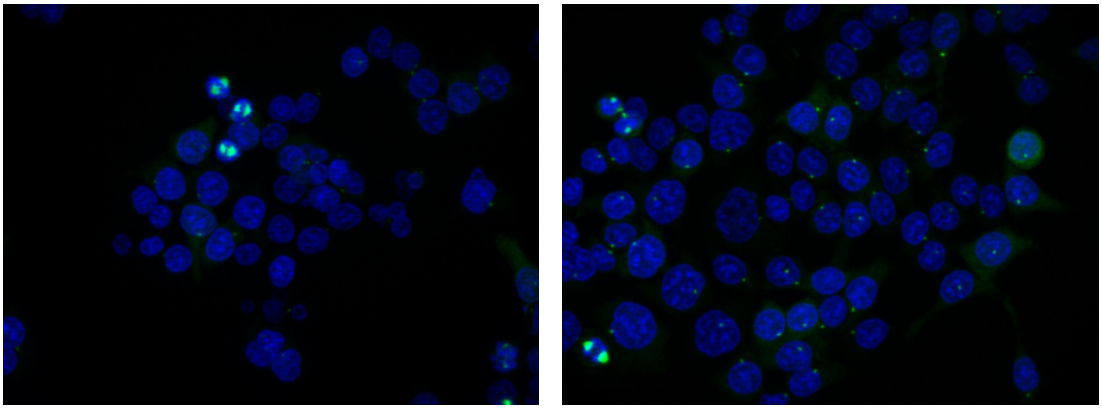

(a) HCT116 STK15 1 40x

(b) HCT116 STK15 1 DMSO 40x

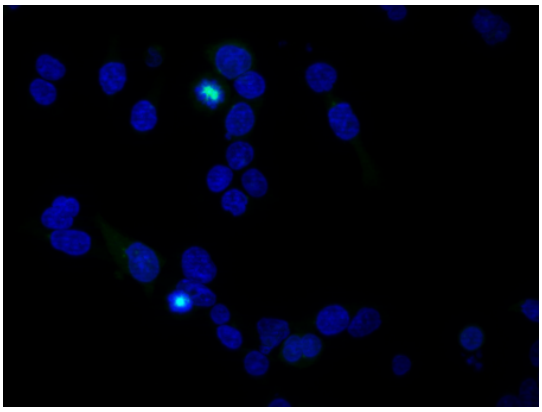

(c) HCT116 STK15 2 40x

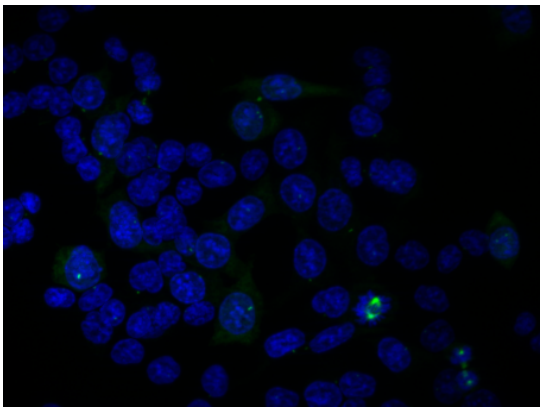

(d) HCT116 STK15 2 DMSO 40x

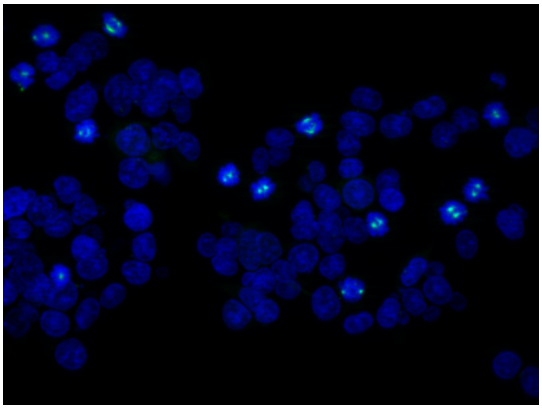

(e) HCT116 STK15 3 40x

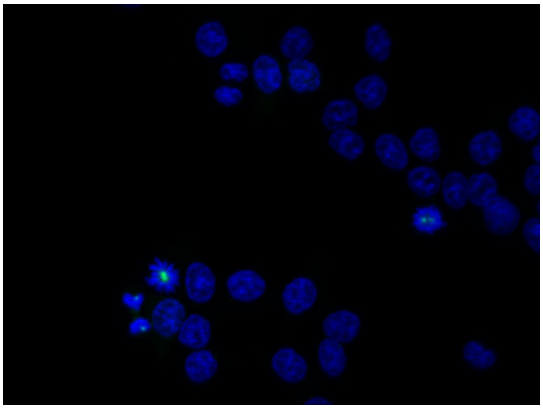

(f) HCT116 STK15 huebsch DMSO 40x

Figure D.8: Raw images of HCT116 cells.

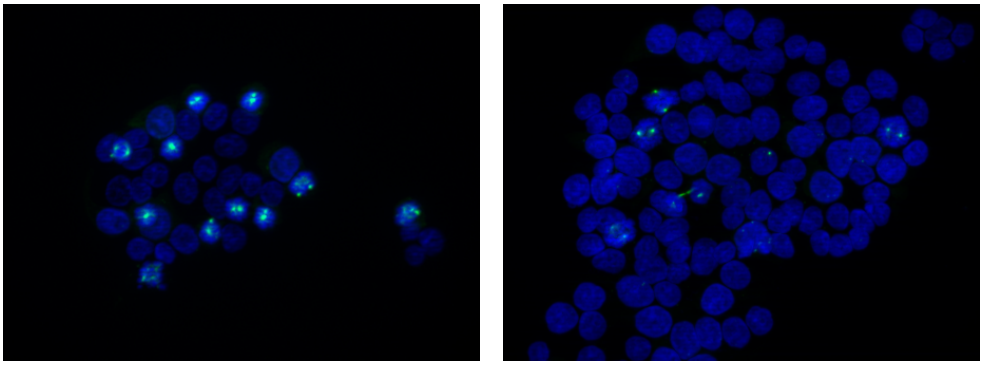

(a) HT29 STK15 1 40x

(b) HT29 STK15 1 DMSO 40x

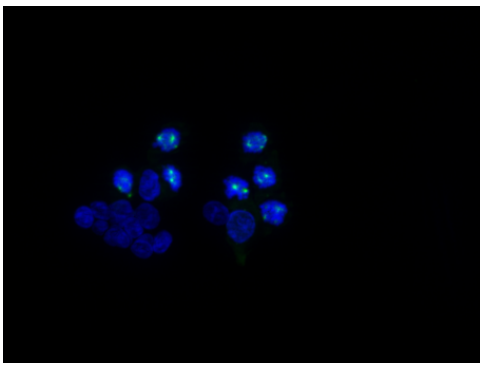

(c) HT29 STK15 2 40x

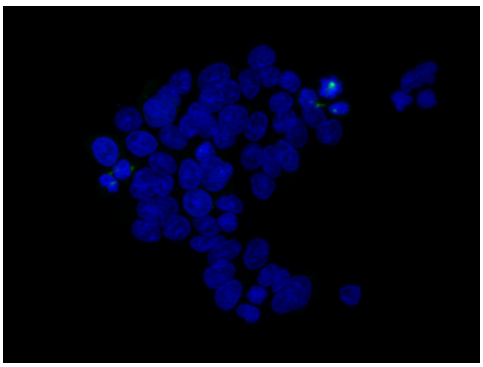

(d) HT29 STK15 2 DMSO 40x

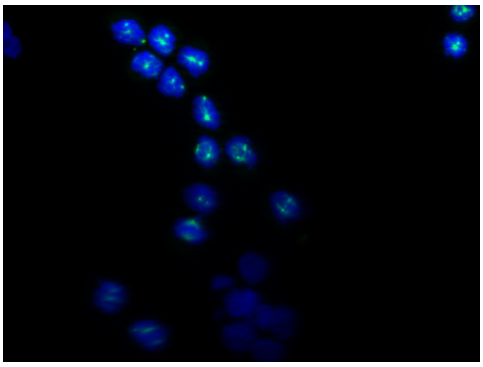

(e) HT29 STK15 3 40x

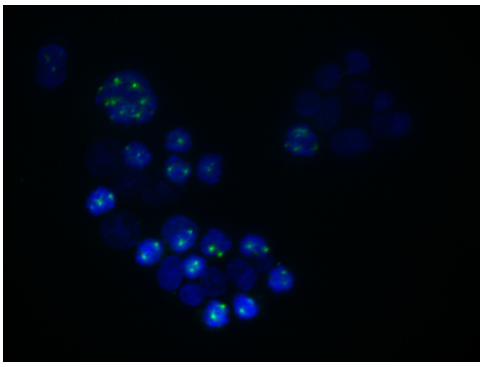

(f) HT29 STK15 4 40x

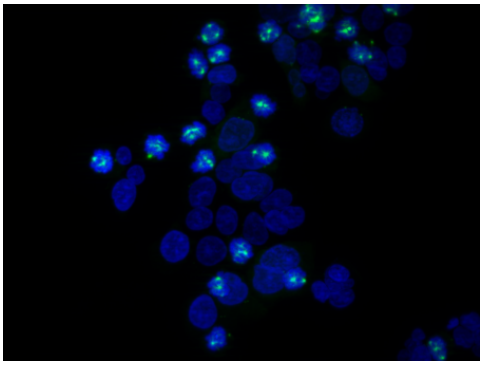

(g) HT29 STK15 5 40x

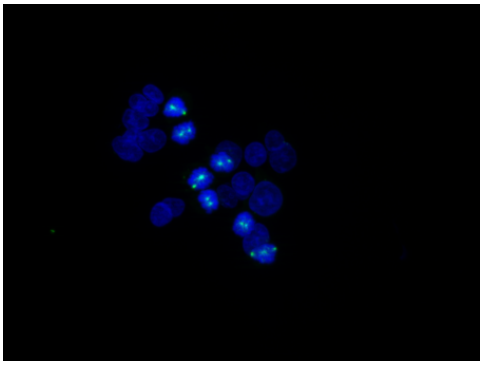

(h) HT29 STK15 6 40x

Figure D.9: Raw images of HT29 cells.

Bibliography

[AJU05] F. Aguet, M. Jacob, and M. Unser. Three-dimensional feature detection using optimal steerable filters. *Image Processing, 2005. ICIP 2005. IEEE International Conference on*, 2:II–1158–61, Sept. 2005.

[BS06] Hubert Bauch and Jörg Schaffer. Optical sections by means of "structured illumination": background and application in fluorescence microscopy. *Photonik international*, I, 2006.

[Cyg05] Bogusaw Cyganek. Object detection in multi-channel and multi-scale images based on the structural tensor. In *Computer Analysis of Images and Patterns*, volume 3691/2005 of *Lecture Notes in Computer Science*, pages 570–578. Springer Berlin / Heidelberg, 2005.

[FY91] William T. Freeman and Edward H. Adelson Y. The design and use of steerable filters. *IEEE Transactions on Pattern Analysis and Machine Intelligence*, 13:891–906, 1991.

[GKW+06] U Gerlach, G Kayser, A Walch, U Hopt, J Schulte-Mönting, M Werner, and S Lassmann. Centrosome-, chromosomal-passenger- and cell-cycle-associated mrnas are differentially regulated in the development of sporadic colorectal cancer. *J Pathol.*, 208(4):462–472, 2006.

[JU04] Mathews Jacob and Michael Unser. Design of steerable filters for feature detection using canny-like criteria. *IEEE Trans. Pattern Anal. Mach. Intell*, 26:1007–1019, 2004.

[KFR03] Michael Kazhdan, Thomas Funkhouser, and Szymon Rusinkiewicz. Rotation invariant spherical harmonic representation of 3d shape descriptors. In *SGP '03: Proceedings of the 2003 Eurographics/ACM SIGGRAPH symposium on Geometry processing*, pages 156–164, Aire-la-Ville, Switzerland, Switzerland, 2003. Eurographics Association.

[LKS+09] S Lassmann, C Kreutz, A Schoepflin, U Hopt, J Timmer, and M Werner. A novel approach for reliable microarray analysis of microdissected tumor cells from formalin-fixed and paraffin-embedded colorectal cancer resection specimens. *J Mol Med*, 87(2):211–224, Feb 2009.

[LWM+07] S Lassmann, R Weis, F Makowiec, J Roth, M Danciu, U Hopt, and Werner M. Array cgh identifies distinct dna copy number profiles of oncogenes and tumor

suppressor genes in chromosomal- and microsatellite-unstable sporadic colorectal carcinomas. *J Mol Med.*, 85(3):293–304, Mar 2007.

[RB08] M. Reisert and H. Burkhardt. Equivariant holomorphic filters for contour denoising and rapid object detection. *IEEE Transactions on Image Processing*, 17(2):190–203, 2008.

[RB09] M. Reisert and H. Burkhardt. Spherical tensor calculus for local adaptive filtering. In S. Aja-Fernández, R. de Luis García, D. Tao, and X. Li, editors, *Tensors in Image Processing and Computer Vision*, Advances in Pattern Recognition. Springer, 2009. to appear.

[Rei07] M. Reisert. Spherical derivatives for steerable filtering in 3d. Technical Report Internal Report 3/07, IIF-LMB, Computer Science Department, University of Freiburg, 2007.

[Rei09] Marco Reisert. Harmonic filerts in 3d - theory and applications. Technical Report 1, Albert-Ludwigs-Universität Freiburg, February 2009.

[RFB05] O. Ronneberger, J. Fehr, and H. Burkhardt. Voxel-wise gray scale invariants for simultaneous segmentation and classification. In *Pattern Recognition - Proc. of the 27th DAGM Symposium, Vienna, Austria*. Springer, Berlin, 2005. DAGM Award.

[Ron07] O. Ronneberger. *3D invariants for automated pollen recognition*. PhD thesis, Albert-Ludwigs-Universität Freiburg, 2007.

[Ros95] M.E. Rose. *Elementary Theory of Angular Momentum*. Dover Publications, 1995.

[RWB08] O. Ronneberger, Qing Wang, and H. Burkhardt. Fast and robust segmentation of spherical particles in volumetric data sets from brightfield microscopy. *Biomedical Imaging: From Nano to Macro, 2008. ISBI 2008. 5th IEEE International Symposium on*, pages 372–375, May 2008.

[SM95] H. Schulz-Mirbach. Invariant features for gray scale images. In G. Sagerer, S. Posch, and F. Kummert, editors, *17. DAGM - Symposium "Mustererkennung"*, pages 1–14, Bielefeld, 1995. Reihe Informatik aktuell, Springer. DAGM-Preis.

[SMH98] G. Sommer, M. Michaelis, and R. Herpers. The svd approach for steerable filter design. *Circuits and Systems, 1998. ISCAS '98. Proceedings of the 1998 IEEE International Symposium on*, 5:349–353 vol.5, May-3 Jun 1998.

[SSR+06] J. Schulz, T. Schmidt, O. Ronneberger, H. Burkhardt, T. Pasternak, A. Dovzhenko, and K. Palme. Fast scalar and vectorial grayscale based invariant features for 3d cell nuclei localization and classification. In *Proceedings of the 28th Pattern Recognition Symposium of the German Association for Pattern Recognition (DAGM 2006), Berlin, Germany*. LNCS, Springer, 2006. DAGM Award.

[SSS04] L. H. Schaefer, D. Schuster, and J. Schaefer. Structured illumination microscopy: artefact analysis and reduction utilizing a parameter optimization approach. *Journal of Microscopy*, 216(2):165 – 174, 2004.

[Tin04] M. Tinkham. *Group Theory in Quantum Mechanics*. Dover Publications, 2004.

[XP97] Chenyang Xu and Jerry L. Prince. Gradient vector flow: A new external force for snakes. In *IEEE Proc. Conf. On*, pages 66–71, 1997.

[XP98] Chenyang Xu and J.L. Prince. Snakes, shapes, and gradient vector flow. *Image Processing, IEEE Transactions on*, 7(3):359–369, Mar 1998.

[YLZW06] Xiaodong Yang, Houqiang Li, Xiaobo Zhou, and Stephen T.C. Wong. Identification of cell-cycle phases using neural network and steerable filter features. In *Advances in Neural Networks - ISNN 2006*, volume 3973 of *Lecture Notes in Computer Science*, pages 702–709. Springer Berlin / Heidelberg, 2006.